FINAL TECHNICAL REPORT

Improved Target Detection in Urban Structures using Distributed Sensing and Fast Data Acquisition Techniques

March 2010 – October 2013

Submitted to

Office of Naval Research

ONR Grant: N00014-10-1-0455

Principal Investigator

Moeness Amin

Contributors

Prof. Moeness Amin
Dr. Fauzia Ahmad
Dr. Yimin Zhang
Dr. Batu Chalise
Mr. Pawan Setlur
Mr. Christian Debes

April 2013

Contents

Executive Summary

This report presents research work performed under the Office of Naval Research grant no. N00014-10-1-0455 over the four- year funding period of 2010-2013. It includes contributions from Prof. Moeness Amin (PI), Dr. Fauzia Ahmad (Research Professor), Dr. Yimin Zhang (Research Professor), Dr. Batu Chalise (Postdoctoral fellow), Mr. Pawan Setlur (PhD Student) and Mr. Christian Debes (Visiting Scholar).

This report deals with the general problem of urban radar. It addresses major challenges in radar imaging of simple and complex scenes inside enclosed structures with efficient data collection systems. The report is divided into two major sections. Each Section has its own abstract and introduction, and also has its own figure numbers, and references. The first section includes a comprehensive discussion of key results obtained for Through-the-Wall Radar Imaging (TWRI) in terms of target detection, exterior and interior wall mitigation, and multipath exploitation. The second section deals with fast acquisition and imaging using significantly reduced data measurements.

It has become very evident that TWRI is emerging as a viable technology for providing high quality imagery of enclosed structures. TWRI makes use of electromagnetic waves below the S-band to penetrate through building wall materials. The indoor scene can be illuminated from each antenna, and be reconstructed using the data from the receive antennas. Due to the "see"-through ability, TWRI has attracted much attention in the last decade with a variety of important civilian and military applications. For instance, this technology is employed for surveillance and detection of humans and interior objects in urban environments, and for search and rescue operations in military situations. In the first section, we cover signal processing algorithms that proved valuable in allowing proper imaging and image recovery in the presence of high clutter, caused by front walls, and multipath, caused by reflections from internal walls. Specifically, we focus on ground-based imaging systems which are relatively mature, and discuss wall mitigation techniques, multipath exploitation methods, change detection of moving target, and compressive sensing for fast data acquisition.

Recently, research efforts have shifted towards effective and reliable imaging under constraints on aperture size, frequency, and acquisition time. In this respect, scene reconstructions are being pursued with reduced data volume and within the emerging compressive sensing (CS) framework. In the second section, we present CS based scene reconstruction techniques that address the unique challenges associated with fast and efficient imaging in urban operations. Specifically, we focus on ground-based imaging systems for indoor targets. We discuss CS based wall mitigation, multipath exploitation, and change detection for imaging of stationary and moving targets inside enclosed structures.

List of Publications

Journal Papers

1. C. H. Seng, M. G. Amin, F. Ahmad, and A. Bouzerdoum,"Image segmentations for through-the-wall radar target detection," IEEE Transactions on Aerospace and Electronic Systems, vol. 49, no. 3, pp. 1869-1896, July 2013.
2. C. Debes, A. M. Zoubir and M. G. Amin, "Enhanced detection using target polarization signatures in through-the-wall radar imaging," IEEE Transactions on Geoscience and Remote Sensing, vol. 50, no. 5, May 2012.
3. C. Debes, J. Hahn, A.M. Zoubir and **M. G. Amin**, "Target discrimination and classification in through-the-wall radar imaging," IEEE Transactions on Signal Processing, vol. 59, pp. 4664-4676, October 2011.
4. C. Debes, J. Riedler, A. M. Zoubir, **M. G. Amin**, "Adaptive target detection with application to through-the-wall radar imaging," IEEE Transaction on Signal Processing, vol. 58, pp. 5572–5583, November 2010.

Conference Papers

1. F. Ahmad and M. G. Amin, "Wall clutter mitigation for MIMO radar configurations in urban sensing," Proceeding of the 11th International Conference on Information Science, Signal Processing, and their Applications, Montreal, Canada, July 2012.
2. E. L. Targarona, M. Amin, F. Ahmad, and M. Nájar, "Compressive sensing for through wall radar imaging of stationary scenes using arbitrary data measurements," Proceeding of the 11th International Conference on Information Science, Signal Processing, and their Applications, Montreal, Canada, July 2012.
3. C.H. Seng, M. Amin, F. Ahmad, and A. Bouzerdoum, "Segmentations of through-the-wall radar images," Proceeding of the Seventh IEEE Radar Conference, Atlanta, GA, May 2012.
4. M. Amin, F. Ahmad, W. Zhang, "A Compressive Sensing Approach to Moving Target Indication for Urban Sensing," Proceeding of the IEEE Radar Conference, Kansas City, MO, May 2011.

Section 1 - New Techniques for Improved Through-the-Wall Radar Imaging: Theory and Applications

1.1 Introduction

The field of remote sensing has developed a range of interesting imaging approaches for a variety of applications. Through-the-wall sensing is a relatively new area that addresses the desire to see inside buildings for various purposes, including determining the room layouts, discerning the building intent and nature of activities, locating the occupants, and even identifying and classifying objects within the building. Through-the-wall sensing is highly desired by police, fire and rescue, emergency relief workers, and military operations. Accurate sensing and imaging can allow a police force to obtain an accurate description of a building in a hostage crisis, or allow firefighters to locate people trapped inside a burning structure. In essence, the goals of through-the-wall sensing technology are to provide vision into otherwise obscured areas.

Each remote sensing application area has driven different sensing modalities and imaging algorithm development based upon propagation characteristics, sensor positioning, and safety issues. Traditional optical, radar, and sonar image processing all begin with basic wave physics equations to provide focusing to individual points. In many radar applications, for example, data sampled from many sensors are mathematically integrated to provide equivalent focusing using free-space propagation assumptions. Free-space imaging is commonly seen in synthetic aperture radar (SAR) techniques since atmospheric distortions are often negligible and can be safely ignored in first-order calculations [23].

Conventional imaging approaches exploit the wave equation to compute the expected phase at each point in space and time over which the data are collected. The complex phase front is similar to the spatial representation of the wavefront captured by a hologram [38]. The complex returns can then be compared against the predicted returns from points in the imaging target space to focus on each point in that space. The focusing is analogous to image reconstruction in holography, where a spatial pattern is projected back into the originating target image space. In true free-space conditions, this focusing approach represents a mathematically accurate way to perform imaging. More sophisticated approaches extend beyond free-space assumptions to allow for more complicated propagation effects, such as adaptive optics [78], atmospheric correction for radar [23], and matched field processing for sonar [79]. Correction approaches range from simple wavefront calibration to more sophisticated volumetric propagation corrections.

Free-space propagation does not apply to several applications where transmission through scattering media is encountered, including many modern imaging approaches such as geophysical sensing, medical imaging, and more recently through-the-wall imaging and sensing. In these applications, propagating signals diffract through a volume. As examples, geophysical imaging techniques generally measure seismic propagation through the earth to look for discontinuities that are often indicators of oil, gas, water, or mineral deposits [59]. In medical imaging, ultrasound tomographic approaches account for propagation through different tissue classes [42].

Non-freespace scattering applications are more representative of the through-the-wall sensing problem, albeit each has its own distinct challenges and approaches. In geophysical and medical applications, the propagation medium is discontinuous but still respectively fills the sensing volume of the earth and tissue. To better propagate into the volume, sensors are placed in direct contact with the medium (e.g., seismometers for geophysical sensing, ultrasound transducers for medical imaging). In through-the-wall sensing, there are many air-material interfaces that dramatically change the wavefront. Through-the-wall sensors may be placed against the front walls or located

1

some distance away from the structure. In either case, attenuation is largely seen only in the building materials and contents rather than in the large volumes of air that occupy most of the space outside or within a building. The rich through- the-wall scattering environment makes volumetric tomographic imaging approaches most relevant for through-the-wall sensing. Rather than using free-space focusing assumptions, correcting for propagation effects may greatly improve the imaging solution [1-3].

Through-the-wall sensing is best motivated by examining the applications primarily driving its development. Through-the-wall sensing grew from the application of ground-penetrating radar systems to walls, with specific applications documented in the literature since the late 1990s showing abilities to sense beyond a single wall from near range [7, 8, 13, 15 ,17, 31-34, 36, 40, 54, 67, 68, 70]. Applications can be divided based upon whether information is sought on motions within a structure or on imaging the structure and its stationary contents.

The need to detect motion is highly desired in situations like firefighters finding a child in a burning building or law enforcement officers locating hostages and their captors. Such applications can resort to Doppler discrimination of movement from background clutter [35, 62, 64, 75]. Motion detection and localization can be decomposed into zero (0-D), one (1-D), two (2-D), or three-dimensional (3-D) systems. A 0-D system is simply a motion detector and will report any motion in the scene. Such systems may be useful to detect whether a room is occupied or not, often useful in monitoring applications such as security systems or intruder detection. Interior motion may be ample information for a firefighter to decide whether to enter a room or building. Since range or angle is not required, 0-D systems may use continuous wave (CW) tones as waveforms. While such systems have exquisite sensitivity, it is difficult to confine the sensitivity to desired areas, so care must be taken to prevent undesired detections beyond the intended range or even from the system operator himself due to multipath reflections. 0-D systems are not particularly useful in cases where other moving individuals may be within the sensor field of view.

One-dimensional systems provide a range to a target but not an angle. The extra dimension provides the ability to separate and possibly discriminate multiple targets. The range information can help bound whether a detection is in the adjacent room, or perhaps deeper within the building. The systems can obviously gate out detections from ranges beyond the ranges of interest, and may more easily discriminate desired target motion from the motion of the operator. The systems often consist of a single receiving antenna in addition to a transmitting antenna (although sometimes a single antenna can be used for both functions). Motion of the operator can be gated out in range, or a reference antenna pointed towards the radar operator can be used for cancellation. Ranging is historically one of the principle reasons for the development of radar technology, but the short stand-off ranges of most through-the-wall systems provide some particular challenges. Three methods are often employed to obtain target range, namely, ultrawideband pulses [47, 48, 51, 54, 80, 83], dual frequencies [9, 10, 62, 91] or stepped CW [7, 36].

Two-dimensional systems provide a slice through the scene in the range and angle dimensions [7, 54, 67]. The 2-D representation provides better localization of the mover, at the expense of a larger antenna array whose elements are collinear. 2-D systems will be subject to layover of objects, meaning that objects out of plane will appear to be rotated to the imaging plane, which can lead to distortion of the field of view. 3-D systems attempt to represent a volumetric representation of the field of view in the range, azimuth, and elevation dimensions [11]. The third dimension avoids the layover issue of targets being projected into a 2-D plane; at the expense of a 2-D array and higher processing requirements. Potentially, the third dimension can provide additional localization for identification of targets. Height information may allow discrimination between people and animals such as household pets, since radar cross-section alone can be unreliable in the presence of through-

the-wall multipath and other issues. The ultimate goal is higher resolution for even better moving target classification. Both 2-D and 3-D processing techniques have generally used either multilateration [1, 32] or SAR techniques [5, 27] using either ultrawideband pulses or stepped CW radars to localize features in the scene.

Imaging of structural features and contents of buildings requires at least 2-D (and preferably 3-D) systems. It cannot rely on Doppler processing for separation of desired features, so multilateration or SAR approaches have been the most commonly used approaches. The general idea behind multilateration is to correlate range measurements from multiple sensors to specific points in the image. With sufficient spatial diversity from a large set of transmit/receive combinations, specific reflection points will start to integrate above the background interference. However, ambiguities will arise as the number of reflection points increases which can provide an over-determined system relative to the transmit/receive signal pairs which can detract from image quality. SAR-based systems can be thought of as a coherent extension of the multilateration concept. Instead of incoherent combinations of range returns from multiple transmit/receive pairs, coherent algorithms are used to provide a complex matched filter to specific points in the target space. SAR algorithms are well established for stand-off imaging applications [23]. Stand-off applications generally assume free-space propagation to each point in the target scene, although platform motion compensation and atmospheric effects are removed with autofocusing algorithms.

Most of the SAR and multilateration techniques usually neglect propagation distortions such as those encountered by signals passing through walls and objects. Distortions degrade the performance and can lead to ambiguities in target and wall localizations. Free-space assumptions no longer apply after the electromagnetic waves propagate through the first wall. As a result, free-space approximations may carry imaging systems through to the first wall, but propagation effects will then affect further imaging results. Shadowing, attenuation, multipath, reflection, refraction, diffraction, and dispersion, all play a role in how the signals will propagate after the first interface. Without factoring in propagation effects, imaging of contents within buildings will be severely impacted. As such, image formation methods, array processing techniques, target detection, image sharpening, and clutter and multipath identification and rejection paradigms must work in concert and be reexamined in view of the nature and specificities of the underlying sensing problem.

A common occurrence of incorrect localization is objects outside the building being illuminated by the reflection off the first wall and subsequently creating an ambiguous image visible inside the building. Moreover, the strong front wall reflection causes nearby indoor weak targets to go undetected. Multipath propagation introduces ghosts or false targets in the image. Uncompensated refraction through walls can lead to localization or focusing errors, leading to offsets and blurring of imaged targets [5, 6, 24, 86]. Bragg scattering off repeating structural elements, such as rebar in concrete walls or repetitive voids in concrete block walls, can cause image ambiguities and modulation of subsequent wavefronts. Some of the wall propagation effects can be compensated for using image-focusing techniques incorporating proper wavefront corrections [5, 24]. SAR techniques and tomographic algorithms, specifically tailored for through-the-wall imaging, are capable of making some of the adjustments for wave propagation through solid materials. While such approaches are well suited for shadowing, attenuation, and refraction effects, they do not account for multipath, Bragg scattering, as well as strong reflections from the front wall.

In this section, we consider new algorithmic that addresses some of the aforementioned unique challenges in through-the-wall sensing operations. More specifically, Section 1.2 deals with techniques for the mitigation of the wall clutter. Front wall reflections are often stronger than target reflections, and they tend to persist over a long duration of time. Therefore, weak and close by targets behind walls become obscured and invisible in the image. Approaches based on both

3

electromagnetic modeling and signal processing are advocated to significantly mitigate the front wall clutter. Section 1.3 presents an approach to exploit the rich indoor multipath environment for improved target detection. It uses a ray tracing model to implement a multipath exploitation algorithm, which maps each multipath ghost to its corresponding true target location. In doing so, the algorithm improves the radar system performance by aiding in ameliorating the false positives in the original SAR image as well as increasing the SNR at the target locations, culminating in enhanced behind the wall target detection and localization. Section 1.4 discusses a change detection approach to moving target indication for through-the-wall applications. Change detection is used to mitigate the heavy clutter that is caused by strong reflections from exterior and interior walls. Both coherent and noncoherent change detection techniques are examined and their performance is compared using real data collected in a semi-controlled laboratory environment.

It is noted that the section provides a signal processing perspective to through-the-wall radar imaging. Outside the scope of this section, there has been significant work performed for TWRI applications in the areas of antenna and system design [16, 44, 65, 83], wall attenuation and dispersion [37, 53, 74], electromagnetic modeling [19, 21, 29, 76], inverse scattering approaches [26, 68, 71], and polarization exploitation [30, 84, 89].

The progress reported in this section is substantial and noteworthy. However, many challenging scenarios and situations remain unresolved using the current techniques and, as such, further research and development is required. However, with the advent of technology that brings about better hardware and improved system architectures, opportunities for handling more complex building scenarios will definitely increase.

1.2   Wall Clutter Mitigation

Scattering from the exterior front wall is typically stronger than that from targets of interest, such as a human or a rifle, which have relatively small radar cross sections (RCS). This makes imaging of stationary targets behind walls difficult and challenging. The problem is further compounded when targets are in close vicinity of walls of either a high dielectric constant or with layered structures. In particular, hollow cinder block walls contain an air-gap void within the cinder block with disparate dielectric constants. This establishes a periodic structure resonance cavity that traps electromagnetic (EM) modes. The consequence of this layered composite structure on radar target imaging is to introduce long time constant relaxations on target detections in radar range profiles. Therefore, weak and close by targets behind walls become obscured and sometimes totally invisible in the image. Thus, wall reflections should be suppressed, or significantly mitigated, prior to applying image formation methods. One of the simple but effective methods is based on background subtraction. If the received signals can be approximated as the superposition of the wall and the target reflections, then subtracting the raw complex data without target (empty scene) from that with the target would remove the wall contributions and eliminate its potential overwhelming signature in the image. Availability of the empty scene, however, is not possible in many applications, and one must resort to other means to deal with strong and persistent wall reflections.

In the past few years, a number of approaches have been proposed to mitigate the front wall returns and effectively increase the signal-to-clutter ratio. For example, the wall reflections can be gated out, the corresponding parameters can be estimated, and then used to model and subtract the wall contributions from the received data [24]. This wall-dependent technique is effective, but its performance is subject to wall estimation and modeling errors. Another method is proposed in [27], which employs three parallel antenna arrays at different heights. The difference between the received signals at two different arrays is used for imaging. Due to the receiver symmetry with respect to the transmitter, a simple subtraction of the radar returns leads to wall reflection

4

attenuation and image improvement. However, this technique requires two additional arrays and the effect of the subtraction operation on the target reflection is unknown and cannot be controlled. In [29], the walls reflections are eliminated by operating the imaging radar in cross-polarization as the cross-polarization returns from a planar interface such as the wall surface are theoretically zero, unlike the returns from humans. However, the cross-polarization returns from the targets behind walls are often very weak compared to their co-polarization counterparts, and as such, the radar performance may be limited by noise.

An eigen-structure technique is developed in [77] to decompose the received radar signal into three subspaces: clutter (including the front wall), target, and noise. Singular value decomposition (SVD is applied on the data matrix to extract the target signatures. SVD has also been used as a wall clutter reduction method for TWRI in [20, 81]. Another approach for wall clutter mitigation is based on spatial filtering. It utilizes the strong similarity between wall EM responses, as viewed by different antennas along the entire physical or synthesized array aperture, is proposed in [87]. The idea is that under monostatic radar operation, the wall returns approximately assume equal values and identical signal characteristics across the array elements, provided that the extent of the wall is much greater than the antenna beamwidth. On the other hand, returns from targets with limited spatial extent, such as humans, vary from sensor to sensor. The dc component corresponding to the constant-type return, which is typical of walls, can be significantly reduced while preserving the target returns by applying an appropriate spatial filter along the array axis. However, care must be exercised in the choice of the spatial filter so that its characteristics cause minimum distortion to the target returns. The spatial-domain preprocessing scheme is analogous, in its objective, to the moving target indication (MTI) clutter filter operation in the time domain.

In this section, we present in details two of the aforementioned methods, namely, the wall parameter estimation method and the spatial filtering technique. For the spatial filtering technique, we consider two different types of filters, namely, moving average subtraction filter and the infinite impulse response notch filter, and compare their effects on the target image.

1.2.1 Spatial Filtering

1.2.1.1 Characteristic of the Wall Reflection

Assume a synthetic aperture radar (SAR) is used in which a single antenna at one location transmits and receives the radar signal, then moves to the next location, and repeats the same operation along the axis parallel to the wall. Assume N antenna locations. With the wall reflection, the received signal at the nth antenna due to a single point target of complex reflectivity σ is given by,

$$z(n,t) = s_w(t - \tau_w) + \sigma s(t - \tau_n) \tag{1.1}$$

where $s_w(t)$ is the signal reflected from the wall, τ_w is the two-way traveling time of the signal from the nth sensor to the wall, $s(t)$ is the transmitted signal convolved with the two-way transmission transfer function of the wall, and τ_n is the two-way traveling time between the nth antenna and the target. Note that σ is assumed to be independent of frequency and τ_w does not vary with the sensor location since the wall is parallel to the array. Furthermore, if the wall is homogeneous and much larger than the beamwidth of the antenna, the wall reflection $s_w(t)$ will be the same for all antenna locations. This implies that the first term in (1.1) assumes the same value across the array aperture. When the wall is not parallel to the array axis, τ_w should be calculated for each sensor location. Compensations for signal attenuations due to differences in the two-way traveling distances for different antenna positions should be performed prior to filtering.

5

Unlike τ_w, the time delay τ_n in (1.1) changes with each antenna location, since the signal path from the antenna to the target is different. For $t = t_0$ and $\sigma = 1$, the received signal is

$$z(n, t_0) = s_w(t_0 - \tau_w) + s(t_0 - \tau_n) \qquad (1.2)$$

for $n = 0, 1, \ldots, N - 1$. Since the time t is fixed, the received signal is now a function of n via the variable τ_n. We can rewrite (1.2) as a discrete function of n such that

$$z_{t_0}(n) = v_{t_0} + u_{t_0}[n] \qquad (1.3)$$

where $v_{t_0} = s_w(t_0 - \tau_w)$ and $u_{t_0}[n] = s(t_0 - \tau_n)$. Since the delay τ_n is not linear in n, $u_{t_0}[n]$ for $n = 0, 1, \ldots, N - 1$ is a nonuniformly sampled version of $s(t)$. Fig. 1(a) shows the signals received by the N antennas at a given time instant. For example, suppose that the n_cth sensor is the closest to the target (see Fig. 1(b)). If the wall diffraction is negligible, then

$$R_{n_c - m} = \sqrt{x_t^2 + (\delta d + md)^2} = \sqrt{(x_t^2 + \delta d^2) + 2md\delta d + (md)^2} = \sqrt{R_{n_c}^2 + 2md\delta d + (md)^2} \quad (1.4)$$

where $m = |n - n_c|$. In most cases, the target's range R_{n_c} is much larger than the antenna spacing d. Then, $R_{n_c}^2 \gg 2md\delta d + (md)^2$. Using Taylor series expansion, we can approximate (1.4) as,

$$R_{n_c - m} \approx R_{n_c}\left(1 + \frac{1}{2}\frac{2md\delta d + (md)^2}{R_{n_c}^2}\right) \qquad (1.5)$$

Therefore,

$$R_{n_c - m} - R_{n_c} \approx \frac{1}{2}\frac{2md\delta d + (md)^2}{R_{n_c}} \qquad (1.6)$$

The received signal at $t = \tau_{n_c}$ is given by

$$z(n, \tau_{n_c}) = s_w(\tau_{n_c} - \tau_w) + s(\tau_{n_c} - \tau_n) \approx v_{\tau_{n_c}} + s\left(-\frac{2md\delta d + (md)^2}{R_{n_c}c}\right) \qquad (1.7)$$

The spatial frequency transform of (1.7) is given by

$$Z(\kappa, \tau_{n_c}) = \sum_{n=0}^{N-1} z(n, \tau_{n_c})e^{-j\kappa n} \approx v_{\tau_{n_c}} \cdot \delta(\kappa) + S_{\tau_{n_c}}(\kappa) \qquad (1.8)$$

where κ denotes the spatial frequency, and $S_{\tau_{n_c}}(\kappa)$ is the target spatial signature at $t = \tau_{n_c}$ such as

$$S_{\tau_{n_c}}(\kappa) = \sum_{n=0}^{N-1} s\left(-\frac{2md\delta d + (md)^2}{R_{n_c}c}\right)e^{-j\kappa n} \qquad (1.9)$$

The above analysis shows that separating wall reflections from target reflections amounts to basically separating constant (zero-frequency signal) from nonconstant valued signals across antennas, which can be performed by applying a proper spatial filter.

1.2.1.2 Target Spatial Signature

In the previous section, it is shown that the target signal across the antennas at a fixed time (fixed down-range) is a nonuniformly sampled version of the target reflection. In order to minimize the effect of the wall removal, which is done by spatial filtering, on the target signal, it is necessary to find the target spatial frequency bandwidth as viewed by the array aperture. This is a critical factor in designing the proposed spatial filters for the purpose of wall reflection removal. The target spatial frequency bandwidth depends on the target downrange, as shown in (1.9), and is also inversely proportional to the extent of the target signal return along the array. At any given time, the latter depends on the array length, target down range, and the target signal temporal duration.

Considering a point target, which reflects the radar signal without modification, the target spatial signature can be analytically computed. The minimum bandwidth occurs when the extent of the target return is maximum. Two different cases can be identified depending on the target location in cross-range relative to the edge of the array. Fig. 2(a) shows the target signal return in the time-space domain when the target is located within the array aperture, whereas Fig. 2(b) shows the case in which the target is outside the array aperture. In these figures, L represents the array length, τ is the signal temporal duration, and R is the target range. Consider the case of Fig. 2(a), where l_0 is the cross-range of the target location from the edge of the array. Without loss of generality, assume that l_0 is larger than or equal to $L/2$. The maximum width of the target return across the array for the case of Fig. 2(a) is (Yoon and Amin, 2009)

$$\mu \approx \sqrt{2R\delta_r} + \min\{\sqrt{2R\delta_r}, L - l_0\} \qquad (1.10)$$

and for the case of Fig. 2(b),

$$\mu = \sqrt{q_2^2 + 2W\delta_r} - q_2 \qquad (1.11)$$

In the above equations, δ_r is the radar down-range resolution and

$$W = \sqrt{R^2 + q_2^2} \qquad (1.12)$$

The maximum width is achieved when the target is located along the centerline of the array

$$\mu_{\max} = \min\{2\sqrt{2R\delta_r}, L\} \qquad (1.13)$$

Define $\mu/\sqrt{2}$ as the effective width. Then, the maximum effective width is

$$\mu_{\max,\mathrm{eff}} = \min\{2\sqrt{R\delta_r}, L\} \qquad (1.14)$$

7

and the corresponding minimum frequency bandwidth is given by

$$\kappa_{B,\min} = \frac{1}{\mu_{\max,\text{eff}}}$$ (1.15)

Note that $\kappa_{B,\min}$ decreases as R increases. This implies that the spatial filter should have a narrower stopband to process the more distant target.

1.2.1.3 Moving Average Wall Removal

Moving Average (MA) filter background subtraction is a noncausal Finite impulse response (FIR) filter, which notches out the zero spatial frequency component. The MA subtraction method has been effectively used for removal of the ground reflections in ground penetrating radar [18]. The effect of the MA on the target image can be viewed in the context of the corresponding change in the point spread function (PSF). With the transmitted signal chosen as a stepped-frequency waveform consisting of Q narrowband signals, let $z(n, f_q)$ be the signal received at the nth antenna at frequency f_q. Let $\tilde{z}(n, f_q)$ be the signal after MA subtraction. That is

$$\tilde{z}(n, f_q) = z(n, f_q) - \bar{z}(f_q)$$ (1.16)

where $\bar{z}(f_q)$ is the MA of $z(n, f_q)$ such as

$$\bar{z}(f_q) = \frac{1}{2D+1} \sum_{m=n-D}^{m=n+D} z(m, f_q)$$ (1.17)

where 2D+1 is the filter length. When the sum is taken over the entire length of the array, the moving average becomes just an average over the entire aperture and 2D+1=N. The klth pixel value of the image obtained by applying delay-and-sum (DS) beamforming to the received data $z(n, f_q)$ is given by

$$b(k,l) = \sum_{n=0}^{N-1} \sum_{q=0}^{Q-1} z(n, f_q) \exp\{ j2\pi f_q \tau_{n,(k,l)} \}$$ (1.18)

where $\tau_{n,(k,l)}$ is the two-way traveling time, through the air and the wall, between the nth antenna and the klth pixel location. The new DS beamforming image after filtering is given by

$$\tilde{b}(k,l) = \sum_{n=0}^{N-1} \sum_{q=0}^{Q-1} \tilde{z}(n, f_q) \exp\{ j2\pi f_q \tau_{n,(k,l)} \} = b(k,l) - \sum_{n=0}^{N-1} \sum_{q=0}^{Q-1} \bar{z}(f_q) \exp\{ j2\pi f_q \tau_{n,(k,l)} \}$$ (1.19)

The second term in the above equation is due to the average subtraction. This additional term depends on the signal waveform, target location, and the antenna positions, implying that the effect of average subtraction varies according to these parameters. The PSF is the DS image of a point source as a function of the down-range and the cross-range. Fig. 3(a) shows the image of the second term in (1.19) when a point target is located 6 m away from the center of a 3m long antenna array. In this case, the maximum value is about 0.13 (The maximum value in PSF is one). The signal is a step-frequency waveform covering the 2–3 GHz band with 5 MHz steps. It is noted that the magnitude of this image assumes a high value over a large cross-range area, whereas the down-range spread of the function is small. Fig. 3(b) is the PSF without spatial filtering. The modified PSF of the spatial filtered signal, which is the difference between Figs. 3(a) and 3(b), is shown in Fig. 3(c).

8

We observe that the size of the mainlobe of the modified PSF remains unchanged with about 0.8 dB loss in the maximum value. However, the sidelobes are higher compared to the original PSF. Although the average subtraction seems to work well in this simulation, the limits of using this subtraction method when handling the distant targets can be shown as follows.

The discrete Fourier transform of $\tilde{z}(f_q)$ is

$$\tilde{Z}(\kappa, f_q) = \sum_{n=0}^{N-1} \tilde{z}(n, f_q) \exp\{-j2\pi\kappa n / N\} = \sum_{n=0}^{N-1} (z(n, f_q) - \bar{z}(f_q)) \exp\{-j2\pi\kappa n / N\}$$
$$= Z(\kappa, f_q) - \bar{z}(f_q) \sum_{n=0}^{N-1} \exp\{-j2\pi\kappa n / N\} = Z(\kappa, f_q) - N\bar{z}(f_q)\delta[\kappa]$$

(1.20)

Note that

$$Z(\kappa, f_q)\big|_{\kappa=0} = \sum_{n=0}^{N-1} z(n, f_q) = N\bar{z}(f_q)$$

(1.21)

Therefore,

$$\tilde{Z}(\kappa, f_q) = \begin{cases} Z(\kappa, f_q) & \kappa \neq 0 \\ 0 & \kappa = 0 \end{cases}$$

(1.22)

As shown above, the subtraction removes the single spatial frequency component ($\kappa = 0$) without changing other components. The actual spatial frequency band that is filtered out is always $1/dN = 1/L$, where L is the array length. When $\mu_{\text{max,eff}}$ is equal to L, the target bandwidth is $1/L$. In this case, most of the target signal return will be removed by the process of the average subtraction. The range at which $\mu_{\text{max,eff}} = L$ is

$$R_L = \frac{L^2}{4\delta_r}$$

(1.23)

For example, for L = 2 m and δ_r = 0.075 m (2 GHz bandwidth), R_L is equal to 13.33 m, implying that when the target's down-range is larger than 13.33 m, the MA subtraction method will eliminate most of the target signature, which is undesirable. Thus, the MA subtraction is simple but produces spatial filter characteristics, which may not be applicable to all wall types and target locations.

1.2.1.4 Notch Filtering

Zero-phase spatial IIR filters, such as notch filters, are good candidates for wall clutter mitigation. The IIR filter provides a flexible design. It overcomes the problem of the fixed MA (average) filter characteristics that could be unsuitable for various wall and target types and locations. Although the IIR filter spatial extent is truncated because of the finite number of antennas, the filter is still capable of delivering good wall suppression performance without a significant change in the target signal when the number of antennas is moderate. A simple IIR notch filter that rejects zero frequency component is given by

$$H_{NF}(\omega) = \frac{1 - e^{-j\omega}}{1 - \alpha e^{-j\omega}}$$

(1.24)

9

The positive parameter α (< 1) determines the width of the filter notch. Fig. 4 shows the frequency response of the filter for various values of α and that of MA subtraction with 67 antenna locations. Note the difference between the notch filters and MA. The notch filter does not have ripples and can change its stopband depending on the parameter α. In the underlying problem, ω is the spatial frequency and the parameter α provides a compromise between wall suppression and target signal conservation. This flexibility is an advantage of the notch filtering over MA subtraction method. As shown in the figure, as α moves closer to one, the stopband becomes narrower such that most of the signal except dc will pass through the filtering.

The spatial spectrum of wall reflections may have a nonzero width due to unstable antenna path and local inhomogeneities. In this case, a wider filter stopband should be applied to remove most of the wall reflections around dc, but it would also reduce the target reflection. Therefore, the spatial filter should be adjusted to the environment. It is noted that the frequency spectrum of the target reflection depends on the range to the target, the transmitted waveform, and the distance between antenna locations. These parameters determine the sampling point of the received signal and, subsequently, the spatial frequency characteristics of the target. If the sampled target signal does not have a dc component, it will not be severely affected by the spatial filter and, as such, the target image after notch filtering will approximately remain unaltered. It is noted that the desire to have the target spatial spectrum least attenuated by the spatial filtering could play an important role in designing signal waveforms for TWRI.

The filter zero-phase property, which is required for a focused image formation, can be achieved by applying the notch filter twice in the forward and backward directions [39]. By two-way filtering, group delay can be removed. One way to avoid the loss of the target signal returns by filtering, particularly if these returns vary slowly across the array aperture antennas, is to increase the delay between antenna outputs. This is true whether the MA, the notch filter, or any other filter is employed. The increased delay can be achieved by down sampling of sensors without making the sensor space too large to cause aliasing. When the antenna positions are down sampled by M, there will be M different sets with N/M antennas. These M sets are filtered independently and the results are used by the delay and sum beamforming. Fig. 5 shows the diagram of notch filter processing. The downsampled signal $w_{m,t}$ for $n = 0,1,\ldots,(N/M) - 1$ and $m = 0,1,\ldots,M - 1$

$$w_{m,t}[n] = z(nM + m - 1, t) \qquad (1.25)$$

The effective filter length of the IIR filter should be considered when downsampling since the length of the downsampled signal is now N/M. A highly truncated IIR will lead to undesired filter characteristics.

1.2.1.5 Imaging Results

A through-the-wall SAR system was set up in the Radar Imaging Lab at Villanova University. A line array of length 1.2446m with 0.0187m inter-element spacing was synthesized, parallel to a 0.14m thick solid concrete wall, at a standoff distance of 1.01m. The back and the side walls of the room were covered with RF absorbing material to reduce clutter. A stepped-frequency signal covering 1 to 3 GHz band with 2.75 MHz frequency step was employed. A vertical dihedral was used as the target and was placed 3.04 m away on other side of the front wall. The size of each face of the dihedral is 0.39 m by 0.28 m. The empty scene without the dihedral target present was also measured for comparison.

First, we examine the validity of the wall EM return assumption that the spatial filtering approach is based on. Fig. 6(a) shows the signal reflected from the concrete wall. It clearly shows the first few

reflections from the wall and as expected, the wall return assumes almost constant values across the antenna positions. In order to quantify the performance of the images, we apply the target-to-clutter ratio (TCR) which is commonly adopted in SAR image evaluations [22, 25]. TCR is similar to the MTI improvement factor, except that the latter is for the time-domain, whereas TCR is for the image domain. TCR is calculated as

$$TCR = 20\log_{10}\left(\frac{\max\limits_{(k,l)\in A_t}|b(k,l)|}{\frac{1}{N_c}\sum\limits_{(k,l)\in A_c}|b(k,l)|}\right)\qquad(1.26)$$

where A_t is the target area, A_c is the clutter area, and N_c is the number of pixels in the clutter area. TCR, in essence, is the ratio between the maximum pixel value of the target to the average pixel value in the clutter region. The clutter region is the area where no target is present and the wall reflection is severe. The clutter area is manually selected in close vicinity to the wall where wall reflections are most pronounced. The rectangles depicted in the figures represent the clutter area and the target area in our example. Fig. 6(b) shows the image without any preprocessing and the target is masked by the wall response. Fig. 6(c) shows the result of applying background subtraction, and the target is clearly visible. Fig. 7(a) and (b) demonstrates that the spatial filtering approach is effective in reducing the wall reflections without significantly compromising the target image. Fig. 7(a) shows the DS image after MA subtraction, and Fig. 7(b) shows the DS image after the notch filtering. TCRs in these figures are 2.2 dB (with wall), 26.2 dB (background subtraction), 13.4 dB (notch filtering), and 15.3 dB (MA subtraction). The background subtracted image provides the highest TCR, while MA subtraction and notch filtering provide comparable performance.

1.2.2 Wall Parameter Estimation, Modelling, and Subtraction

1.2.2.1 Approach

In this approach, the effect of the wall on EM wave propagation is achieved through three steps. The wall parameters are accurately estimated. Then, the reflected signal from the wall is properly modelled. Finally, the modelled signal is subtracted from the measured signal.

Building walls, such as brick, adobe, and poured concrete walls, can be modelled by homogeneous dielectric slabs. Using the geometric optics approach, the reflection coefficient γ for vertically and horizontally polarized incident waves through the wall is given by [24, 45]

$$\gamma = \frac{R_{01} + R_{10}e^{j2k_{1x}d}}{1 + R_{01}R_{10}e^{j2k_{1x}d}}, \quad R_{10} = -R_{01} = \frac{1 - p_{10}}{1 + p_{10}}\qquad(1.27)$$

where $p_{10} = k_{0x}/k_{1x}$ for horizontal polarization and $p_{10} = \varepsilon_r k_{0x}/k_{1x}$ for vertical polarization of the incident fields. In (27), ε_r is the relative dielectric constant, d is the thickness of the wall, and k_{0x} and k_{1x} are the normal components of the propagation constants in air and in the dielectric, respectively. The expressions for the vertical/transverse magnetic and horizontal/transverse electric unit vectors are given in [45].

The wall parameters can be estimated from the time-domain backscatter at a given location [24, 73]. Basically, the response of the wall is gated from the total backscatter signal and transferred to the

frequency domain. The mean-squared error between the calculated reflection coefficient γ of (1.27) and the measured reflection coefficient γ_m given by

$$\delta = \frac{1}{N_f} \sum_{n=1}^{N_f} |\gamma_m(f_n) - \gamma(f_n)|^2 \qquad (1.28)$$

is computed, and its minimum is searched for the wall thickness and permittivity [24,88]. In (1.28), N_f is the number of frequency points and f_n is the nth frequency.

The estimated wall parameters are then used to compute the wall EM reflection. This could be accomplished either numerically using EM modelling software, or in case of far-field conditions, analytically using the following expression [24]

$$E_r^w(k_n) = \frac{G\lambda}{8\pi} \frac{e^{j2k_n x_0}}{x_0} \Gamma(\theta_i = 0, k_n) \qquad (1.29)$$

where x_0 is the standoff distance of the radar from the wall, λ is the wavelength, G is the antenna gain, $k_n = 2\pi f_n / c$ is the nth wave constant, c is the speed of light in free space, and $\Gamma(\theta_i = 0, k_n)$ is the reflectivity matrix from the wall at normal incidence angle and is given by,

$$\Gamma = \begin{bmatrix} \gamma_v & 0 \\ 0 & \gamma_h \end{bmatrix} \qquad (1.30)$$

In (30), the subscripts 'v' and 'h', respectively, denote the vertical and horizontal polarization and $\gamma_{v/h}$ is given by (1.27). This estimated wall reflection should be coherently subtracted from the total received signal in order to isolate the signature of the target on the other side of the wall.

The isolated target return can then be processed to generate an image of the scene. The effects of the wall transmissivity on the target image are the following: 1) dislocation of the target from its actual position in range and 2) significant degradation in cross-range resolution [5, 24]. To compensate for the effects of transmission through the wall, a compensation factor proportional to the inverse of the squared of the wall transmittivity can be used in the conventional free-space image formation methods. In cases where transmissivity is low and the signal is noisy, division by a small noise-affected number may cause significant distortion. In such cases, one may use only the phase of transmission coefficients as a compensation factor [24].

1.2.2.2 Imaging Results

An experimental study was conducted at the Radiation Laboratory in University of Michigan. The measurement setup consists of an HP8753D vector network analyzer, two double ridge horn antennas with operational frequency range of 1 to 18 GHz, an XY table along with a control unit, and a personal computer. The vertically aligned antennas, one for transmission and the other for reception, are mounted on a vertical wooden rod (along the z-axis), which is attached to the carriage of the XY table. A 2.37m x 1.77m wall composed of poured concrete blocks is made on top of a layer of cinder blocks inside the laboratory. The underlying cinder block layer is used to line up the antennas in height at approximately the middle of the concrete block wall. Figure 8(a) shows the side view of the measurement setup. A small trihedral corner reflector with pentagonal panel

geometry is used as a point target behind the wall, as shown in Fig. 8(b). The back corner of the trihedral (scattering phase center) is at x = −0.71 m and at the same height as that of the receiver antenna, i.e., 1.28 m above the ground plane. The transmitting antenna is attached about 0.25 m below the receiving antenna on the wooden rod. The antennas are moved along a scan line of length 95.88 cm, parallel to the wall, with a spacing of 2.04 cm. The apertures of both antennas are about 0.45 m away from the wall. The frequency of operation is from 1 to 2.5 GHz and the frequency step is 12.5 MHz. It is noted that the antennas are in the far-field region of the target.

An image is first constructed under assumption of free-space propagation by using the total received signal, and is shown in Fig. 9(a). Here, in addition to the target, the wall is also imaged, primarily as two parallel lines showing the front and back boundaries. Since backscatter from the wall is very strong, the sidelobes generated by image formation spill over into desired image domain, which is manifested as multiple lines parallel to the wall surfaces. Also, the target appears blurred and its location is biased. Figure 9(b) shows the image after the estimate, model, and subtract approach was applied. The wall thickness and the permittivity were estimated using (1.28) as 20 cm and 5.7 + j0.6, respectively. The wall reflection was computed using (1.29) and subtracted from the total received signal, and the resulting signal was used for image formation. For comparison, the signal prior to wall return subtraction was used for imaging wherein compensation for the effect of transmission through the wall was applied and is shown in Fig. 9(c). Although the imaged target is at the correct location and is refocused in Fig. 9(c), existence of the wall sidelobes in the image is still evident. By comparing Figs. 9(b) and (c), a substantial improvement in clutter rejection is observed after subtraction of the modeled wall return.

1.3   Multipath Exploitation

The existence of targets inside a room or in an enclosed structure introduces multipath in the radar return, which results in false targets or ghosts in the radar images. These ghosts lie on or near the vicinity of the back and side walls, leading to a cluttered image with several false positives. Without a reasonable through-the-wall multipath model, it becomes difficult to associate a ghost to a particular target. Identifying the nature of the targets in the image and tagging the ghosts with their respective target according to a developed multipath model, although important to reduce false alarms, is not the final goal of a high-performance through-the-wall imaging system. Since each multipath provides some information about the target, it becomes prudent to utilize the multipath rather than ignoring it, once identified. The utilization or exploitation of the multipath to one's advantage represents a paradigm shift when compared to the classical approach of either ignoring or mitigating it.

For through-the-wall radar imaging applications, the existence of multipath has been recently demonstrated for stationary targets in [4, 19, 28]. In [4], the authors use distributed fusion to remove the false targets caused either from multipath or target interactions for stationary scenes after suitable image registration. In [9], time reversal techniques are used to alleviate ghosts and clutter from the target scene and in [28], a synthetic aperture radar (SAR) based image of a human inside a room is shown along with possible multipath ghosts. However, no more rigorous multipath modeling and analysis are presented in the aforementioned references [4, 19, 28] and the references therein.

In this section, we derive a model for the multipath in an enclosed room of four walls. The model considers propagation through a front wall and specular reflections at interior walls. A SAR system is considered and stationary or slow moving targets are assumed. Although the multipath model presented deals with walls, reflections from the ceiling and floor can be readily handled, similar to the work in [61]. We demonstrate analytically that the multipath as seen by each sensor is displaced,

13

and, therefore, we derive the actual focusing positions of the multipath ghosts in downrange and crossrange. The multipath model permits an implementation of a multipath exploitation algorithm, which associates as well as maps each target ghost back to its corresponding true target location. In so doing, the exploitation algorithm improves the radar system performance by ameliorating the false positives in the original SAR image as well as increasing the signal-to-clutter ratio (SCR) at the target locations, culminating in enhanced behind the wall target detection and localization. It is noted that the exploitation algorithm only maps back target-wall interactions; target-target interactions are left untreated. The multipath exploitation algorithm is inspired by the work in [43], wherein the shadowed regions of a target are revealed via its multipath returns. The difference, however, is that we are not striving to reveal the shadowed regions of the target. In our case, we deal with targets with arbitrary dielectric constants, and wish to associate and map each multipath to its true target location.

1.3.1 Image Formation Algorithm

In this section, we describe the through-the-wall delay-and-sum beamforming approach [5, 11, 12]. We consider a SAR system in which a single antenna at one location transmits a wideband signal and receives the radar return, and then moves to the next location and repeats the same operation along the axis parallel to the front wall. Assume N monostatic antenna locations. The setup is as depicted in Fig. 10. Consider a single point target, located at $\mathbf{x}_t = [x_t, y_t]^T$. At each antenna location, the radar transmits a pulsed waveform $s(t)$, where 't' indexes the time within the pulse, and measures the reflected signal. The target return at the nth antenna location is given by,

$$r_n(t) = T_n^2(\mathbf{x}_t) a(\mathbf{x}_t) s(t - 2\tau_n(\mathbf{x}_t)) \tag{1.31}$$

where $a(\mathbf{x}_t)$ represents the target reflectivity, $T_n(\mathbf{x}_t)$ is the complex amplitude associated with the one-way propagation through a dielectric wall for the nth antenna location [63], and $\tau_n(\mathbf{x}_t)$ represents the one-way through-the-wall propagation delay from the nth antenna location to the target.

The scene of interest comprises several pixels indexed by the downrange and the crossrange. The complex composite return from the kth pixel location $\mathbf{x}_k$ is obtained by applying time delays to the N received signals, followed by weighting and summing the results. That is,

$$r(t, \mathbf{x}_k) = \sum_{n=0}^{N-1} w_n r_n(t + 2\tau_n(\mathbf{x}_k)) \tag{1.32}$$

The signal $r(t, \mathbf{x}_k)$ is passed through a matched filter, with impulse response $h(t) = s^*(-t)$. The complex amplitude assumed by the pixel $\mathbf{x}_k$ in the image $I(\cdot)$ is obtained by sampling the matched filter output at time $t = 0$,

$$I(\mathbf{x}_k) = \{r(t, \mathbf{x}_k) * h(t)\}|_{t=0} \tag{1.33}$$

where '$*$' denotes the convolution operation. Equations (1.32-1.33) describe the standard beamforming approach in through-the-wall radar imaging. It is noted that if the imaged pixel is in the vicinity of or at the true target location, then the complex amplitude in (1.33) assumes a high value as given by the system's point spread function. The process described in (1.32) and (1.33) is carried out for all pixels in the scene of interest to generate the image of the scene.

14

The beamforming approach as described above is pertinent to a point target in a two-dimensional (2D) scene. Extensions to three-dimensional (3D) scenes and spatially extended targets are discussed in [11, 85]. It is noted that, in the above beamforming description, we have not considered the multipath returns; neither have we addressed the specificities of calculating the delays, $\tau_n(\cdot)$, which will be treated in detail in the following sections. Without loss of generality, we now assume that the weights $w_n = 1, \forall n$ and the target has unit reflectivity.

1.3.2 Multipath Model

Consider a room under surveillance using a SAR system. A priori knowledge of the room layout, i.e., wall locations and material properties, is assumed. The scene being observed relative to the nth sensor location is as shown in Fig. 11. The origin is marked as point 'O' in the figure, and the standard convention for the positive x- and y- axes is assumed. The nth sensor location is given by $\mathbf{R}_n = [-D_{xn}, 0]^T$. The front wall has a thickness d_1 and dielectric constant ε_1. For notational simplicity, the back and the side walls are also assumed to have ε_1 as the dielectric constant. The side walls, labeled as wall-1 and wall-3, have a length D_1, whereas the front wall and the back wall (wall-2) have a length D_2. The target is stationary and at location $\mathbf{A} = [-x_t, y_t]^T$. The standoff distance from the front wall is constant for each sensor location constituting the synthetic aperture, and is denoted as D_y. In the figure, we consider the direct path, referred to as path-A, and three additional paths, namely, paths-B, C, and D, which correspond to single-bounce multipath. In general, there exist other paths which can contribute to the multipath returns; these include multiple bounces from the back and side walls as well as paths that include multiple reflections within each of the four walls themselves. Examples of the former and the latter are provided in Fig. 12. Such paths are defined as higher-order multipath. Hence, in Fig. 11, we have considered only first-order multipath. It is noted that higher-order multipath are in general weaker compared to the first-order multipath due to the secondary reflections and refractions at the various air-wall interfaces and high attenuation in the wall material. Therefore, we choose to exclude these paths from the model.

The walls are assumed smooth with specular reflections. The smoothness assumption is valid, since for through-the-wall radars, the wavelength of operation is much larger than the roughness of the walls. Specular reflections are a direct consequence of the wall smoothness, and necessitate that the angle of incidence be equal to the angle of reflection. Note that, in general, the back and side walls may each be of a different material (interior or exterior grade), and thus may assume different values for the wall thickness and dielectric constant. If interior reflections inside these walls are considered, then the thickness of these walls is required [19, 28, 43]. However, since we have ignored such higher-order paths, we only require the dielectric constant of the back and side walls to be known. As the EM wave propagates through the front wall, it bends at the medium discontinuity as dictated by Snell's law, i.e., each of the paths, as seen in Fig. 11, has an associated angle of incidence and an angle of refraction. For example, the angles of incidence and refraction for path-B are denoted as $\psi_{iB}^{(n)}$ and $\psi_{rB}^{(n)}$, respectively. Similar nomenclature follows for the remaining paths.

Let the reflection points on wall-1, 2, and 3 be denoted by B_n, C_n, and D_n, with respective position vectors $\mathbf{B}_n = [0, y_{Bn}]^T$, $\mathbf{C}_n = [-x_{Cn}, D_1 + D_y]^T$, and $\mathbf{D}_n = [-D_2, y_{Dn}]^T$. It is clear that these position vectors are dependent on the sensor location. The one-way path delays for the four paths, with the antenna at the nth location, are denoted by $\tau_p^{(n)}, p \in \{A, B, C, D\}$, and can be derived from the geometry as

$$\tau_A^{(n)} = (d_1\sqrt{\varepsilon_1}\sec(\psi_{rA}^{(n)}) + (y_t - d_1)\sec(\psi_{iA}^{(n)}))/c$$

$$\tau_B^{(n)} = (d_1\sqrt{\varepsilon_1}\sec(\psi_{rB}^{(n)}) + (y_{Bn} - d_1)\sec(\psi_{iB}^{(n)}) + x_t\csc(\psi_{iB}^{(n)}))/c$$

$$\tau_C^{(n)} = (d_1(\sqrt{\varepsilon_1}\sec(\psi_{rC}^{(n)}) - \sec(\psi_{iC}^{(n)})) + (2D_1 + 2D_y - y_t)\sec(\psi_{iC}^{(n)}))/c$$

$$\tau_D^{(n)} = (d_1\sqrt{\varepsilon_1}\sec(\psi_{rD}^{(n)}) + (y_{Dn} - d_1)\sec(\psi_{iD}^{(n)}) + (D_2 - x_t)\csc(\psi_{iD}^{(n)}))/c$$

(1.34)

with c being the speed of light and the coordinates of B_n, C_n, and D_n given by

$$y_{Bn} = y_t - x_t\cot(\psi_{iB}^{(n)})$$

$$x_{Cn} = x_t + (D_1 + D_y - y_t)\tan(\psi_{iC}^{(n)})$$

$$y_{Dn} = y_t - (D_2 - x_t)\cot(\psi_{iB}^{(n)})$$

(1.35)

Equations (1.34) and (1.35) depend on the angles of incidence and refraction. Since the standoff distance is a known constant, by projecting the various paths to the x-axis, we obtain the following equations, which are useful in calculating the various angles.

$$d_1\tan(\psi_{rA}^{(n)}) + (y_t - d_1)\tan(\psi_{iA}^{(n)}) - D_{xn} + x_t = 0$$

$$d_1\tan(\psi_{rB}^{(n)}) + (y_{Bn} - d_1)\tan(\psi_{iB}^{(n)}) - D_{xn} = 0$$

$$(2D_1 + 2D_y - y_t)\tan(\psi_{iC}^{(n)}) + d_1(\tan(\psi_{rC}^{(n)}) - \tan(\psi_{iC}^{(n)})) - D_{xn} + x_t = 0$$

$$d_1\tan(\psi_{rD}^{(n)}) + (y_{Dn} - d_1)\tan(\psi_{iD}^{(n)}) - D_2 + D_{xn} = 0$$

(1.36)

The angles of refraction can be determined from Snell's law as,

$$\psi_{rp}^{(n)} = \sin^{-1}\left(\frac{\sin(\psi_{ip}^{(n)})}{\sqrt{\varepsilon_1}}\right), \quad p \in \{A, B, C, D\}$$

(1.37)

Substituting the angles of refraction from (1.37) in (1.36), and using (1.35), we obtain a set of equations that can be solved numerically for the angles of incidence by using the Newton method. The angles of refraction can then be obtained using (1.37).

We are now in a position to write the radar signal return from the single target scene as a superposition of the direct path and the multipath returns. For the nth sensor location, we obtain

$$r_n(t) = \sum_{p\in\{A,B,C,D\}} T_{pn}^2 s(t - 2\tau_p^{(n)}) + \sum_{\substack{(p,q)\in\{A,B,C,D\} \\ p\neq q}} T_{pn}T_{qn}s(t - \tau_p^{(n)} - \tau_q^{(n)})$$

(1.38)

where T_{pn} is the complex amplitude associated with reflection and transmission coefficients for the one-way propagation along path-p, and depends on the angles of incidence, the angles of refraction, and dielectric properties of the walls [63]. In (1.38), the first summation captures the two-way returns along the direct path and each multipath. More specifically, the signal propagates along a particular path-p, $p \in \{A, B, C, D\}$, reaches the target and retraces the same path back to the radar, i.e., path-p. The multipath returns due to the combination paths are captured by the second

16

summation, i.e., the wave initially travels to the target via path-p and returns to the radar through a different path-q, $q \in \{A, B, C, D\}$.

From Fig. 11 and (1.35), we observe that the coordinates of the points of reflection at the back and side walls are sensor dependent, implying that the multipath presents itself at different locations to the different sensors. Location of the multipath as seen by each sensor and the actual focusing position of the resulting ghost in the image are discussed next.

1.3.2.1 Multipath Locations

For simplicity of analysis, consider the scenario in Fig. 11, but without the front wall. We first focus on the multipath originating from wall-1, i.e., the signal travelling to the target via path-A, and following path-B back to the radar or vice versa. The goal is to find the location of the multipath corresponding to the above combination path as seen by each of the N sensors. Let the point $P_n^{w_1}$, represented by the vector $[-x_{tn}^{w_1}, y_{tn}^{w_1}]^T$, denote the multipath location as seen by the nth sensor. The superscript 'w_1' stresses that the multipath is associated with the reflection at wall-1 and the subscript 't' indicates that the multipath is due to the target located at $[-x_t, y_t]^T$. Reflecting path B about wall-1 yields an alternate radar-target geometry, as shown in Fig. 13. We obtain the virtual target denoted by point A^1 with coordinates $[x_t, y_t]^T$ such that the distance $AB_n = A^1 B_n$, which implies that

$$AR_n + AB_n + B_n R_n = AR_n + A^1 R_n \tag{1.39}$$

In other words, the combination path comprising of path-A and path-B has the same length as path-A and the path connecting the nth sensor to the virtual target at A^1. Due to the monostatic nature of the radar system, this combination path appears to the nth sensor as the traditional two way path of length $2R_n P_n^{w_1}$. Therefore, we have

$$R_n P_n^{w_1} = \frac{AR_n + A^1 R_n}{2} \tag{1.40}$$

Additionally, we obtain the virtual radar at $\mathbf{R}_n^1 = [D_{xn}, 0]^T$ on the other side of the wall, as shown in Fig. 13. Considering Fig. 13, it is readily observed that the first order multipath has the same time delay as a bistatic configuration, comprising the radar and the virtual radar. That is, in terms of range, we have

$$R_n A + R_n A^1 = R_n A^1 + R_n^1 A^1 \tag{1.41}$$

where $R_n A^1 + R_n^1 A^1$ represents the bistatic configuration. In the bistatic case, the constant range contour corresponding to the multipath is an ellipse, which has foci at the radar and virtual radar and passes through the target and the virtual target locations. On the other hand, the monostatic measurement scenario described by (1.40) has a circular constant range contour, centered at the radar. Since the two measurements are equivalent, the location of the multipath corresponds to the point of intersection of the bistatic elliptical and the monostatic circular constant range contours. The equations for the ellipse and circle are given by,

$$\frac{(x_{tn}^{w_1})^2}{(R_n P_n^{w_1})^2} + \frac{(y_{tn}^{w_1})^2}{(R_n P_n^{w_1})^2 - D_{xn}^2} = 1 \tag{1.42}$$

$$(x_{tn}^{w_1} + D_{xn})^2 + (y_{tn}^{w_1})^2 = (R_n P_n^{w_1})^2$$

Solving (42) for an intersection point, we can readily see that $x_{tn}^{w_1} = 0$ is the only solution. In other words, regardless of the location of the target, its first-order multipath always falls on the wall. The y-coordinate of $P_n^{w_1}$ can then be derived as

$$y_{tn}^{w_1} = \pm \sqrt{\frac{(AR_n + A^1 R_n)^2}{4} - D_{xn}^2} \tag{1.43}$$

In (1.43), the positive y-coordinate is the desired value as the other solution lies behind the radar. It is clear from (1.43) that the multipath location is sensor dependent. Therefore, the locations of the target multipath corresponding to the various sensor positions will be displaced from one another. In the presence of the front wall, the multipath remains on the wall, but the equations for the ellipse and circle are different than that presented in (1.42). Hence, for the scenario comprising of the front-wall and wall-1, the multipath appears on wall-1, with its y-coordinate given by,

$$y_{tn}^{w_1} = \left(\frac{c\tau_A^{(n)} + c\tau_B^{(n)}}{2} + d_1 (\sec(\psi_{it}^{(n)w_1}) - \sqrt{\varepsilon_1}\, \sec(\psi_{rt}^{(n)w_1})) \right) \cos(\psi_{rt}^{(n)w_1}) \tag{1.44}$$

where $\psi_{it}^{(n)w_1}$ and $\psi_{rt}^{(n)w_1}$ are, respectively, the angles of incidence and refraction for the ghost. The solution in (1.44) depends on the angle $\psi_{it}^{(n)w_1}$, which can be obtained by solving

$$d_1 \tan(\psi_{rt}^{(n)w_1}) + \left(\frac{c\tau_A^{(n)} + c\tau_B^{(n)}}{2} + d_1 \sqrt{\varepsilon_1}\, \sec(\psi_{rt}^{(n)w_1}) \right) \sin(\psi_{it}^{(n)w_1}) - D_x = 0$$

$$\psi_{rt}^{(n)w_1} = \sin^{-1} \left(\frac{\sin(\psi_{it}^{(n)w_1})}{\sqrt{\varepsilon_1}} \right), \tag{1.45}$$

So far, we have considered the multipath corresponding to wall-1; there exist two other multipath returns tagged to the remaining walls, namely, wall-2, and wall-3. We can readily show, using similar analysis, that the multipath associated with wall-2 appears on wall-2, i.e., $y_{tn}^{w_2} = D_y + D_1$, at an x-coordinate given by

$$x_{tn}^{w_2} = -\sin(\psi_{it}^{(n)w_2}) \times \left(\begin{array}{l} d_1 (\sqrt{\varepsilon_1}\, \sec(\psi_{rt}^{(n)w_2}) - \tan(\psi_{rt}^{(n)w_2})\cosec(\psi_{it}^{(n)w_2})) \\ + D_x \cosec(\psi_{it}^{(n)w_2}) - \dfrac{c\tau_A^{(n)} + c\tau_C^{(n)}}{2} \end{array} \right) \tag{1.46}$$

The angles in the above equation are determined by solving the equations,

$$d_1 \sec(\psi_{it}^{(n)w_2}) + (D_1 - d_1)\sec(\psi_{it}^{(n)w_2}) + d_1\sqrt{\varepsilon_1}\,\sec(\psi_{rt}^{(n)w_2}) - \frac{c\tau_A^{(n)} + c\tau_C^{(n)}}{2} = 0$$

$$\psi_{rt}^{(n)w_2} = \sin^{-1}\left(\frac{\sin(\psi_{it}^{(n)w_2})}{\sqrt{\varepsilon_1}}\right), \tag{1.47}$$

Likewise, the multipath associated with wall-3 appears at wall-3, i.e., $x_{tn}^{w_3} = -D_2$, and at a y-coordinate given by,

$$y_{tn}^{w_3} = \left(\frac{c\tau_A^{(n)} + c\tau_D^{(n)}}{2} + d_1(\sec(\psi_{it}^{(n)w_3}) - \sqrt{\varepsilon_1}\,\sec(\psi_{rt}^{(n)w_3}))\right)\cos(\psi_{rt}^{(n)w_3}) \tag{1.48}$$

The respective angles can be obtained by solving,

$$d_1 \tan(\psi_{rt}^{(n)w_3}) + \left(\frac{c\tau_A^{(n)} + c\tau_D^{(n)}}{2} + d_1\sqrt{\varepsilon_1}\,\sec(\psi_{rt}^{(n)w_3})\right)\sin(\psi_{it}^{(n)w_3}) - D_2 + D_x = 0$$

$$\psi_{rt}^{(n)w_3} = \sin^{-1}\left(\frac{\sin(\psi_{it}^{(n)w_3})}{\sqrt{\varepsilon_1}}\right), \tag{1.49}$$

From the above equations, it is again observed that the *N* sensors view the multipath, resulting from the combination paths associated with a particular wall, at different locations on that wall. That is, the multipath maybe regarded as a moving target. As a result, when applying beamforming, the multipath ghost appears at a different pixel in the vicinity of the true multipath locations. We note that the multipath ghost will lie inside the room except when the target is near the corners of the room. In this case, as the multipath corresponding to the N sensors may appear along an extrapolation of the wall, the multipath ghost may appear outside the room. We further note that the virtual target corresponds to two-way propagation along the single-bounce multipath, and is readily seen to lie outside the room perimeter. The multipath focusing pixel analysis for the combination paths is discussed next.

1.3.2.2 Multipath Focusing Analysis

Consider Fig. 14, which shows the multipath locations w.r.t to walls-1-3, and the focusing pixels w.r.t to these walls. Consider the multipath locations associated with wall-1; further assume that the focused multipath ghost appears at a pixel location given by

$$\mathbf{x}_t^{w_1} = [-\Delta x_1 + x_{t1}^{w_1}, \Delta y_1 + y_{t1}^{w_1}]^T \tag{1.50}$$

where $\mathbf{x}_{t1}^{w_1} = [-x_{t1}^{w_1}, y_{t1}^{w_1}]^T$ is the true multipath location corresponding to the first sensor position. Using a first order Taylor series expansion, which is valid under conditions of a small aperture [82] and when the ghost is in the vicinity of the true multipath locations, we obtain the difference in propagation path length between the multipath ghost location and the true multipath location w.r.t the first sensor position as

$$\Delta\varsigma_1^{w_1} = \Delta x_1 \frac{D_{x1} - D_y \tan(\psi_{it}^{(1)w_1}) - d_1 \tan(\psi_{rt}^{(1)w_1}) - x_{t1}^{w_1}}{\sqrt{(D_{x1} - D_y \tan(\psi_{it}^{(1)w_1}) - d_1 \tan(\psi_{rt}^{(1)w_1}) - x_{t1}^{w_1})^2 + (y_{t1}^{w_1} - D_y - d_1)^2}}$$

$$+ \Delta y_1 \frac{y_{t1}^{w_1} - D_y - d_1}{\sqrt{(D_{x1} - D_y \tan(\psi_{it}^{(1)w_1}) - d_1 \tan(\psi_{rt}^{(1)w_1}) - x_{t1}^{w_1})^2 + (y_{t1}^{w_1} - D_y - d_1)^2}}$$

$$(1.51)$$

Following the analysis in [82], (1.51) can be expressed as

$$\Delta\varsigma_1^{w_1} = \Delta x_1 \sin(\psi_{it}^{(1)w_1}) + \Delta y_1 \cos(\psi_{it}^{(1)w_1}) \tag{1.52}$$

In general, for the nth sensor, we have

$$\Delta\varsigma_n^{w_1} = \Delta x_1 \sin(\psi_{it}^{(n)w_1}) + (\Delta y_1 - (y_{tn}^{w_1} - y_{t1}^{w_1}))\cos(\psi_{it}^{(n)w_1}), \ n = 1,\dots,N \tag{1.53}$$

For the multipath to focus at the location $x_t^{w_1}$, we must have,

$$\Delta\varsigma_n^{w_1} = 0, \text{ for } n = 1,\dots,N \tag{1.54}$$

This yields a least squares (LS) formulation, given by

$$\mathbf{A}_1 \mathbf{e}_1 = \mathbf{b}_1, \quad \mathbf{e}_1 = [\Delta x_1, \Delta y_1]^T, \quad \mathbf{A}_1 := [\mathbf{a}_1^{w_1} \ \mathbf{a}_2^{w_1}]^T$$
$$\mathbf{a}_1^{w_1} = [\sin(\psi_{it}^{(1)w_1}),\dots,\sin(\psi_{it}^{(N)w_1})]^T, \quad \mathbf{a}_2^{w_1} = [\cos(\psi_{it}^{(1)w_1}),\dots,\cos(\psi_{it}^{(N)w_1})]^T \tag{1.55}$$
$$\mathbf{b}_1 := [0, y_{t2}^{w_1} - y_{t1}^{w_1},\dots,y_{tN}^{w_1} - y_{t1}^{w_1}]^T \circ \mathbf{a}_2^{w_1}$$

where '$\circ$' denotes the Hadamard or element-wise product. The solution of (1.55) is readily obtained by $(\mathbf{A}_1^T \mathbf{A}_1)^{-1}\mathbf{b}_1$.

Now, considering the multipath w.r.t wall-2, we have the following LS formulation for the focused ghost pixel.

$$\mathbf{A}_2 \mathbf{e}_2 = \mathbf{b}_2, \quad \mathbf{e}_2 = [\Delta x_2, \Delta y_2]^T, \quad \mathbf{A}_2 := [\mathbf{a}_1^{w_2} \ \mathbf{a}_2^{w_2}]^T$$
$$\mathbf{a}_1^{w_2} = [\sin(\psi_{it}^{(1)w_2}),\dots,\sin(\psi_{it}^{(N)w_2})]^T, \quad \mathbf{a}_2^{w_2} = [\cos(\psi_{it}^{(1)w_2}),\dots,\cos(\psi_{it}^{(N)w_2})]^T \tag{1.56}$$
$$\mathbf{b}_2 := [0, y_{t2}^{w_2} - y_{t1}^{w_2},\dots,y_{tN}^{w_2} - y_{t1}^{w_2}]^T \circ \mathbf{a}_2^{w_2}$$

Similarly, for the multipath from wall-3, we have

$$\mathbf{A}_3 \mathbf{e}_3 = \mathbf{b}_3, \quad \mathbf{e}_3 = [\Delta x_3, \Delta y_3]^T, \quad \mathbf{A}_3 := [\mathbf{a}_1^{w_3} \ \mathbf{a}_2^{w_3}]^T$$
$$\mathbf{a}_1^{w_3} = [\sin(\psi_{it}^{(1)w_3}),\dots,\sin(\psi_{it}^{(N)w_3})]^T, \quad \mathbf{a}_2^{w_3} = [\cos(\psi_{it}^{(1)w_3}),\dots,\cos(\psi_{it}^{(N)w_3})]^T \tag{1.57}$$
$$\mathbf{b}_3 := [0, y_{t2}^{w_3} - y_{t1}^{w_3},\dots,y_{tN}^{w_3} - y_{t1}^{w_3}]^T \circ \mathbf{a}_2^{w_3}$$

The formulations in (1.55-1.57) assume that the sensor position increases from left to right. In other words, sensor-1 is at the far left of the array whereas sensor-N is at the far right.

1.3.3   Multipath Exploitation Algorithm

Noting that the multipath ghosts exist due to the presence of the target, we state our objective as follows. Given the beamformed image $\{I(\mathbf{x}_k)\}_{k=1}^K$, our aim is to associate each multipath ghost with the respective target via the model developed in Section 1.3.2. The principle is captured in Fig. 15, which consists of two targets and six false positives or multipath ghosts. We desire to associate and map these ghosts to their respective true target locations. The main advantages of such an association or mapping are reduction in false positives in the original beamformed image, and an increase in the SCR at the true target coordinates. Note that the first advantage is directly implied in Fig. 15, whereas the second advantage is explained as follows.

For ease of exposition, the technique is explained considering the focused multipath ghost from wall-1 only. The technique for exploiting all the ghosts w.r.t to all three walls is enumerated subsequently. Consider an arbitrary pixel location $\mathbf{x} = [x, y]^T$, whose focused multipath ghost w.r.t wall-1 presents itself at location $\mathbf{x}^{w_1} = [x^{w_1}, y^{w_1}]^T$. Consider an intermediate image, $I_1(\mathbf{x})$, wherein the association and mapping of the focused multipath ghosts is performed using simple 2D weighting functions. That is,

$$I_1(\mathbf{x}) \in \mathbb{C}^K = \sum_{k=1}^{K} I(\mathbf{x}_k)\Phi_1(\mathbf{x}^{w_1}, \mathbf{x}_k, \sigma^2)\Phi_2(\mathbf{x}, \mathbf{x}_k, \sigma^2)$$

$$\Phi_1(\mathbf{x}^{w_1}, \mathbf{x}_k, \sigma^2) := \exp\left(-|\mathbf{x}^{w_1} - \mathbf{x}_k|^2 / \sigma^2\right) \Phi_2(\mathbf{x}, \mathbf{x}_k, \sigma^2) := 1 - \exp\left(-|\mathbf{x} - \mathbf{x}_k|^2 / \sigma^2\right)$$

(1.58)

where $\Phi_1(\cdot)$ and $\Phi_2(\cdot)$ are the weighting functions and σ^2 is an arbitrary variance. The weighting functions are related to the two dimensional real Gaussian distributions. A natural improvement, albeit not pursued here, is to let the variance in the y-direction to be equal to the system's range resolution, the variance in the x-direction to be equal to the system's crossrange resolution, and introducing a correlation which is a function of the actual ghost location. This would ensure that the ensuing weighting functions are rotated and sheared to match the system's point spread function, nevertheless at a higher computational cost. The role of $\Phi_1(\cdot)$ and $\Phi_2(\cdot)$ is explained as follows. Consider the weighting function $\Phi_1(\cdot)$; if the pixel $\mathbf{x}_k$ is in the vicinity of the focused multipath ghost pixel $\mathbf{x}^{w_1}$ associated with the target location $\mathbf{x}$, then $\Phi_1(\cdot)$ assumes a large value. On the other hand, if $\mathbf{x}_k$ is not in the vicinity of $\mathbf{x}^{w_1}$, then $\Phi_1(\cdot)$ assumes a low value. Since an exponential function is used, the weights are always between 0 and 1, the lower bound being theoretically unachievable. The vicinity is obviously controlled by the variance parameter, σ^2. From our extensive simulations, we found that a lower variance must be chosen for smaller dimension rooms. For small rooms, it is logical to assume that the ghosts and higher order multipath are located quite close to one another. Therefore, it becomes prudent to be conservative in selecting the variances. Large variances for smaller rooms lead to false mappings. Thus, variance selection for the problem at hand must be guided by the actual dimensions of the room being imaged. The weighting function $\Phi_2(\cdot)$ rejects pixel locations at and in the vicinity of the imaged pixel, i.e., the location corresponding to the assumed true target location $\mathbf{x}_k = \mathbf{x}$. This is required because, although the focus point is singular, but due to the system's point spread function, some of the energy is spread to the neighboring pixels.

From our extensive simulations, we found that as the original image $I(\cdot)$ is complex-valued, summing or integrating across the multipath pixels may result in destructive interference yielding a

poor SCR. This loss of SCR is against our principle of multipath exploitation. To alleviate this problem, we use the intensity of the original beamformed image in (1.58) as

$$I_1(\mathbf{x}) \in \mathfrak{R}^K = \sum_{k=1}^{K} |I(\mathbf{x}_k)|^2 \ \Phi_1(\mathbf{x}^{w_1}, \mathbf{x}_k, \sigma^2) \Phi_2(\mathbf{x}, \mathbf{x}_k, \sigma^2) \qquad (1.59)$$

which implies an incoherent summation. Now considering the ghosts w.r.t the three walls, we can readily see that (1.59) is modified as

$$I_1(\mathbf{x}) = \sum_{w_i=w_1}^{w_3} \sum_{k=1}^{K} |I(\mathbf{x}_k)|^2 \ \Phi_1(\mathbf{x}^{w_i}, \mathbf{x}_k, \sigma^2) \Phi_2(\mathbf{x}, \mathbf{x}_k, \sigma^2) \qquad (1.60)$$

Image $I_1(\cdot)$ will have no intensity at and near the vicinity of the focused multipath pixels. Hence, consider the following composite image obtained by simple pixel-wise multiplication.

$$I_f(\mathbf{x}) = I_1(\mathbf{x}) \times |I(\mathbf{x})|^2 \qquad (1.61)$$

The effect of pixel-wise multiplication in (1.61) is as follows. The image $I_1(\cdot)$ will have deep nulls at the hypothesized ghosts locations, whereas a large peak at the true target location. Thus, (1.61) is essentially a masking operation, nulling the ghosts in the original image $I(\cdot)$, and simultaneously enhancing the energy at the true target location. Hence, the composite image $I_f(\cdot)$ will alleviate the false positives, i.e., the multipath ghosts and increase the intensity of the true target pixel. In the approach described, the multipath ghost locations are readily obtained using the multipath focusing analysis in Section 1.3.2.2.

It is noted that, in practice, different targets may exhibit significantly weaker bistatic radar cross sections (RCS) relative to their monostatic RCS. Accordingly, some or maybe all of the target ghosts may go unnoticed. In this case, the proposed multipath exploitation approach will not prove beneficial as there may not be any increase in the target SCR. Also, consider a scenario where one target presents itself at one of the other target's focused multipath ghost. Since multipath is unexploited in the original beamformed image, we would declare the presence of the target at the pixel in question. On the other hand, the proposed approach will map this target and of course the collocated multipath ghost back to the other target's location causing the second target to go undetected. The question then arises whether one should ignore the multipath ghosts and consider them as true targets or instead exploit the multipath ghosts. The former has an unreasonably high false alarm rate, whereas the latter yields poor target detection for the considered scenario, which, although rare, can occur in practice. However, noting that indoor targets of interest are typically in motion, it is reasonable to assume that a genuine target would not persist on a multipath ghost throughout the surveillance period. Hence, multipath exploitation should be preferred. Another scenario of interest is when the direct path to the target is blocked. In that case, although the ghosts will be mapped to the true target coordinates in the image $I_1(\cdot)$, the masking operation in (1.61) will cause the target to still go undetected as the original image $I(\cdot)$ will have a null at the target location.

1.3.4 Experimental Results

A through-the-wall SAR system was set up in the Radar Imaging Lab at Villanova University. A stepped-frequency signal with 696 steps covering the 1-3GHz frequency band was used. This provides a range resolution of 0.15m and a maximum unambiguous range of 40m. The room

22

dimensions are $D_1 = 5.09$m and $D_2 = 3.78$m. The side walls and part of the floor were covered with RF absorbers and only multipath due to the back wall was considered. The front wall is made of 0.15m thick solid concrete blocks with a dielectric constant of 7.66. The synthetic aperture consisted of an 81-element monostatic linear array with an inter-element spacing of 2.22cm. The standoff distance of the array from the front wall is 1.53m. The experimental set up is depicted in Fig. 16.

Two different experiments were conducted. In the first experiment, a 0.35m diameter metal sphere, labeled as 'Target 1' in Fig. 16, was used as a target. The second experiment consisted of two targets, the first being the sphere used in the single target case, while the second, labeled as 'Target 2' in Fig. 16, was a smaller metallic sphere of 0.2032m diameter. An empty scene measurement without the targets present in the scene was also made and was coherently subtracted from the target scene data to reduce the clutter. The beamformed image corresponding to the single target scene is depicted in Fig. 17(a); both the target and the ghost are clearly visible in the image. In addition, other target-room interactions, such as those resulting from multiple bounces within the front wall, can be observed. The result after multipath exploitation is provided in Fig. 17(b). The variance of the weighting functions in the exploitation algorithm was chosen to be equal to the system's range resolution. We observe that as expected, the ghost has been correctly mapped back to the target, while the other target-room interactions are left as is in the exploited image. Figure 18(a) shows the beamformed image corresponding to the two target scene. Both targets as well as the two ghosts with respect to the back wall are clearly seen. The multipath exploited image is provided in Fig. 18(b), in which one can see that the ghosts have been mapped back to the target locations. We note that, similar to the single target case, the other target-room and target-target interactions are retained in Fig. 18(b).

1.4 Change Detection Based MTI Approach

Detection of humans is one of the most important objectives in urban sensing and through-the-wall radar technology [13-15, 28, 46, 50, 58]. Humans belong to the class of animate objects which are characterized by motion of the limbs, breathing, and heartbeat. These features separate animate and inanimate objects and allow the detection of targets of interest to proceed based on changes in the phase of the scattered radar signals over successive probing and data observations.

Change detection techniques have been recently used to detect moving targets in the presence of heavy clutter that is caused by strong reflections from exterior and interior walls. In the case of moving targets, the subtraction of two consecutive or non-consecutive data frames or images enjoys the same benefits as the background subtraction process for the case of stationary targets. That is, it results in effective removal of all wall returns and non-target clutter. The subtraction operation performed for either case of stationary or moving targets is referred to as Change Detection (CD). The length of the time period elapsing between the two datasets to be subtracted may differ for the two cases. While the stationary scene permits long time periods, the moving target case necessitates short periods. When operating on data frames, both operations can be described by what is known as delay line cancellers (DLC) [66].

It is known that moving target indication (MTI) processing applies clutter filters to remove radar returns scattered from stationary objects. Delay line cancellers can be designed such that their frequency responses place a notch at DC and concurrently meet other desirable passband and stopband filter characteristics [66]. Doppler filter banks typically follow the delay line canceller, and provide benefits of signal separations, radial velocity measurements, and noise reduction [66]. It is important to note that for urban sensing environments, changes in the backscattered signal phase due to motion do not necessarily lend themselves to Doppler frequency shifts. The human motion can be abrupt and highly nonstationary, producing a time-dependent phase whose rate of change

may fail to translate into a single shift or multi-component sinusoids that can be captured by different Doppler filters. Instead, the corresponding wide spectrum of human motions becomes non-localizable and can span the entire radar frequency band. In lieu of Doppler filters, time-frequency processing can be applied to reveal the instantaneous frequency signatures, as it is the case with Human gait. Human gait classification and biometric radar have been discussed in [55-57, 72, 75]. However, apart from regularized motions, such as walking and running, time-frequency Doppler signal representations are very complex and difficult to interpret, especially when dealing with non-homogeneous walls. Therefore, the application of Doppler and Microdoppler filters for indoor target surveillance may not significantly add to target motion detection that is already achieved by delay line cancellers.

Change detection in through-the-wall radar imaging was first discussed concurrently in [59] and [52]. In [59], the Synchronous Impulse Reconstruction (SIRE) radar system, operating in the frequency band of 300MHz-3GHz and employing a multi transmit/receive design, was used for MTI. The change detection approach discussed in [59] subtracts the down range profiles over consecutive data frames, emulating a derivative operator. It was shown that the SIRE successfully detects a human target moving within an enclosed structure. On the other hand, change detection was applied in [52] in the context of background subtraction to detect stationary targets using data acquired during interrogations of a scene at two different time instants. Image intensity subtraction was employed and examples based on ray tracing data covering the 0.7 to 3.1 GHz frequency range were provided. More recently, [69] applied change detection for slow-moving target detection in through-the-wall radar imaging (TWRI) by subtracting the image intensity corresponding to different data frames, followed by a zero threshold operation to suppress the reference image. Examples of target detection in [69] included both EM modeling data and real experiments. Change detection using first- and second- order motion detection images for TWRI application were discussed in [41, 90]. The former has better sensitivity to motion, whereas the latter provides better signal-to-noise ratio (SNR). Experimental data, reported in [41, 90] using four antennas and a signal bandwidth of 500 MHz to 1 GHz, demonstrated that change detection techniques are capable of detecting walking human and simulated human breathing using machine motion. Moving target indicator filtering was also used in [41] for detection of humans in motion inside buildings. An ultrawideband frequency-modulated continuous-wave radar with an extended frequency sweep from 0.5 to 8 GHz was used in the differential mode to track human motion behind a brick wall.

In this section, we examine change detection formulation and performance when clutter removal is performed either coherently or noncoherently. Rather than operating on successive pulses, delay line canceller equivalences are applied to different data frames for each range bin (or equivalently different complex amplitude images for each pixel) (coherent CD) or different intensity images for each pixel (noncoherent CD). The frames can be consecutive, dealing with targets exhibiting sudden short motions, or nonconsecutive with relatively long time difference, for the case in which the target changes its range gate position.

1.4.1 Signal Model

We develop the signal model for wideband operation with multiple transmitters and receivers under coherent integration. Sequential use of the transmitters with simultaneous reception at all receivers is assumed. It is noted that time-multiplexing of the transmitters is a viable option for coherent radar operation in through-the-wall radar sensing applications. This is due to the following two main reasons: a) Ground-based urban imaging radar systems are typically vehicle portable, which restricts the available real estate for deploying multiple antennas on the same platform; this, combined with the important constraint of low cost, results in deployment of far more receivers than wideband transmitters, and b) Indoor targets of interest, such as humans, move at low velocities. As a result,

the time required to collect one data frame with sequential use of the transmitters is small enough so that the target remains stationary during the measurement. The sequential transmit operation is a salient feature of two known through-the-wall radar imaging systems; one is built by the Army Research Lab [50, 59], and the other by the Defense Research and Development Canada [65].

Consider an imaging radar with an M-element linear transmit array and an N-element linear receive array. Let $s(t)$ be the wideband signal used for interrogating the scene. The signal duration T_s is assumed to be less than the pulse repetition interval T_r. Assuming coherent integration of K pulses, the coherent integration interval becomes KT_r. For the case of a single point target of reflectivity σ_p, located at $\mathbf{x}_p = (x_p, y_p)$, the kth emitted pulse with the mth transmitter active is received at the nth receiver in the form

$$z_{mn}(t,k) = \sigma_p s(t - mKT_r - kT_r - \tau_{p,mn}) \tag{1.62}$$

where $\tau_{p,mn}$ is the propagation delay for the signal to travel between the mth transmitter, the target at $\mathbf{x}_p$, and the nth receiver. For through-the-wall propagation, $\tau_{p,mn}$ will comprise the components corresponding to traveling distances before, through, and after the wall [11]. The term mKT_r in (1.62) indicates the additional time required for data collection when the mth transmitter becomes active in a sequential order. We assume that the transmitters transmit their pulses in contiguous time intervals, each of length KT_r. It is further assumed that we deal with targets of constant radar cross section (RCS) over the range of the used frequencies and target aspect angles. The received signal is passed through a filter matched to the transmit waveform and the output can be expressed as

$$z_{mn}^{MF}(t,k) = z_{mn}(t,k) * h(t) = \int_0^{T_r} h(u) z_{mn}(t-u,k) du \tag{1.63}$$

where $h(t) = s^*(-t)$. With K pulses coherently integrated, we obtain

$$z_{mn}^{CI}(t) = \sum_{k=0}^{K-1} z_{mn}^{MF}(t,k) \tag{1.64}$$

In order to generate an image of the scene being interrogated, the MN outputs corresponding to the operation of M transmitters and N receivers are processed as follows. The region of interest is divided into a finite number of pixels in x and y, where x and y represent the crossrange and downrange, respectively. The composite signal corresponding to the pixel, located at $\mathbf{x}_q = (x_q, y_q)$, is obtained by summing time delayed versions of the MN filtered signals,

$$z_q(t) = \sum_{m=0}^{M-1} \sum_{n=0}^{N-1} z_{mn}^{CI}(t + \tau_{q,mn}) \tag{1.65}$$

where $\tau_{q,mn}$ is the focusing delay applied to the matched filtered output of the nth receiver with the mth transmitter active. It is noted that additional weighting can be applied during the summation operations of (1.65) to control the sidelobe level of the transmit-receive array pattern of the imaging radar system. Substituting (1.62), (1.63), and (1.64) in (1.65) yields

$$z_q(t) = \sum_{m=0}^{M-1} \sum_{n=0}^{N-1} \sum_{k=0}^{K-1} \int_0^{T_r} h(u) z_{mn}(t + \tau_{q,mn} - u, k) du \qquad (1.66)$$

The complex amplitude image value $I(\mathbf{x}_q)$ for the pixel at $\mathbf{x}_q$ is obtained by sampling the signal $z_q(t)$ at time $t = 0$. That is,

$$I(\mathbf{x}_q) = z_q(t) \big|_{t=0} \qquad (1.67)$$

The process described by (1.65)-(1.67) is repeated for all pixels in the image to generate the composite image of the scene. The general case of multiple targets can be obtained by superposition of target reflections [5, 11].

1.4.2   Change Detection

In its simplest form, the MTI processing is achieved by using the radar images corresponding to two data frames, which may be consecutive or separated by one or more data frames. Due to time multiplexing of transmitters, a data frame length T_f is equal to M coherent integration intervals, i.e. $T_f = MKT_r$. Let $\left\{ I^{(t)}(\mathbf{x}_q) \right\}_{q=0}^{Q-1}$ and $\left\{ I^{(t+LT_f)}(\mathbf{x}_q) \right\}_{q=0}^{Q-1}$ be the radar images corresponding to the data collected over the two frames, where Q is the number of pixels in each image and L denotes the number of frames between the two acquisitions. It is noted that $L = 1$ represents the case when the two acquisitions are performed over consecutive frames. The timing interval for each data frame is assumed to be a fraction of a second so that the moving target appears stationary during data collection.

Change detection can be performed in two ways, namely, coherent CD and noncoherent CD [41, 52, 59, 69, 90]. In the former approach, complex amplitude image values corresponding to the two data frames are subtracted on a pixel by pixel basis. The latter approach involves subtraction of image pixel intensity values corresponding to different data frames, followed by a zero threshold operation to suppress the reference image. For the coherent approach, the motion detection image can be expressed as follows,

$$\Delta(\mathbf{x}_q) = I^{(t+LT_f)}(\mathbf{x}_q) - I^{(t)}(\mathbf{x}_q), \quad q = 0,1,\ldots,Q-1 \qquad (1.68)$$

Using (66) and (67), we can rewrite (68) as

$$\Delta(\mathbf{x}_q) = \sum_{m=0}^{M-1} \sum_{n=0}^{N-1} \sum_{k=0}^{K-1} \int_0^{T_r} h(u) \delta z_{mn}(t + \tau_{q,mn} - u, k) du \Bigg|_{t=0} \qquad (1.69)$$

where

$$\delta z_{mn}(t,k) = z_{mn}(t - LMKT_r, k) - z_{mn}(t,k) = z_{mn}(t,k) * [\delta(t - LMKT_r - kT_r) - \delta(t - kT_r)] \quad (1.70)$$

and $z_{mn}(t,k)$ is defined in (1.62). From (1.68)-(1.70), we observe that the subtraction of complex amplitude image values for each pixel amounts to subtraction of the received data corresponding to

the two frames for each range bin, followed by image formation. Equation (1.70) provides the equivalent delay line canceller representation for change detection directly in the data domain. A block diagram of the data domain CD algorithm implementation is provided Fig. 19. Note that the windowing operation in the figure ensures application of the algorithm over data frames of length T_f. The block diagram of Fig. 19 is a two-frame delay line canceller, reminiscent of the commonly used two-pulse DLC for clutter filter in range-Doppler radars [66]. More frames can be used in CD leading to multiple frames delay line canceller, which is similar to three- or higher- pulse DLC. However, unlike range-Doppler radar systems, in which higher order clutter filters provide flexibility in trading off clutter suppression with Doppler frequency magnitude, there are no clear advantages of using multiple frames in CD for the underlying problem. Hunt suggested averaging multiple frames, only to emphasize the stationary targets [90].

The noncoherent CD approach involving intensity images is depicted in Fig. 20. In this case, the intensity images corresponding to the two data frames are first computed. Then, a difference image is generated by a pixel by pixel subtraction of the intensity images as

$$\Delta(\mathbf{x}_q) = |I^{(t+LT_f)}(\mathbf{x}_q)|^2 - |I^{(t)}(\mathbf{x}_q)|^2, \quad q = 0,1,\ldots,Q-1 \tag{1.71}$$

The final motion detection image is obtained by a zero threshold operation

$$\Delta_{TH}(\mathbf{x}_q) = \begin{cases} \Delta(\mathbf{x}_q) & \text{if } \Delta(\mathbf{x}_q) \geq 0 \\ 0 & \text{otherwise} \end{cases} \tag{1.72}$$

This threshold results in the target appearing in the final motion detection image only at the position it was occupying during acquisition of the second (test) data frame, since the target image at position corresponding to the first (reference) data frame appears as a negative value after intensity subtraction and is thus removed. It is noted that, unlike the complex amplitude image subtraction, there is no equivalent data domain representation for the intensity image subtraction or noncoherent CD approach due to the nonlinearity of the modulus function in (1.71). However, the delay line canceller framework can still be applied. The image intensity at each pixel can be viewed as a nonlinear function of the data in the respective frame, and the subtraction, implied by the DLC, is performed between two corresponding pixels separated by one or multiple frames.

The aforementioned change detection schemes, though presented for motion detection, can also be applied for detection of stationary targets in the presence of clutter and noise [52]. If a target-free background image of the scene being interrogated is available (feasible when the radar system is being used for long term surveillance), it can be subtracted (complex amplitude or intensity pixel subtraction) from an image of the same scene acquired at a later time that may contain a target of interest, thus rendering background subtraction as a special case of change detection.

1.4.3 Experimental Results

A wideband through-the-wall imaging radar system was set up in the Radar Imaging Lab at Villanova University. A stepped-frequency CW signal, consisting of 101 frequency steps of size 10 MHz, covering the 1.5-2.5 GHz band was chosen for imaging. The bandwidth of 1 GHz provides a range resolution of 15cm and the 10 MHz frequency step allows 15m unambiguous range, which is roughly three times the length of the room being imaged. An Agilent network analyzer, model ENA 5071B, was used for signal synthesis and data collection. A horn antenna, model ETS-Lindgren 3164-04, with an operational bandwidth from 0.7 to 6 GHz, was mounted on a Field Probe Scanner to synthesize an 11-element uniform receive line array with an inter-element spacing of 7.5cm. Two horn antennas

(model ETS-Lindgren 3164-04), mounted on tripods and placed slightly above and on either side of the receive array, were used as transmitters. Each transmitter was spaced 3.75cm away from the nearest receiver. Thus, for the system used, $M = 2$ and $N = 11$. A 10ft x 8ft wall segment was constructed utilizing 0.14m thick solid concrete blocks with a dielectric constant of 7.66. The receive array was at a standoff distance of 1.05m from the wall, whereas the transmitters were positioned 1.33m in downrange from the wall.

In order to illustrate the performance of change detection under complex and intensity image delay line cancellers, we consider the following experiment. A human walks away from the front wall in an empty room, following a straight line path. Since simultaneous data cannot be collected at all receive locations due to the synthetic nature of the receive aperture, eight different target positions were considered, separated by 15cm, along the trajectory, as illustrated in Fig. 21. Data was collected for all eight positions, with the target stationary at each position, using time multiplexing of the transmitters. At each position, coherent integration was performed over 16 measurements. That is, $K = 16$ for the experiment.

We first consider the case where the person moves from position 3 to position 4. That is, the two acquisitions are performed over consecutive frames and $L = 1$. Figures 22(a) and (b) show the beamformed images using the data corresponding to positions 3 and 4, respectively. Both images show strong reflections from the front wall, rendering target returns hard to detect in either image. Figure 23(a) shows the result of coherent change detection wherein the complex radar image of Fig. 22(a) is subtracted from the complex image of Fig. 22(b). We observe that all stationary background including the front wall has been eliminated from the image, and the target undergoing motion has been detected. Since the target appears in two consecutive range cells, no clear target displacement is observed and the target image appears blurred. The corresponding noncoherent CD results under intensity image DLC are presented in Fig. 23(b). We observe that the intensity image DLC removes most of the imaged target in the case of consecutive range cell acquisitions. Moreover, due to the nonlinearity of the modulus function, the stationary background in the image is in general different for each data acquisition, thereby causing the background to be only partially cancelled out under intensity image DLC [69]. As a result, stronger artifacts than those of the complex image DLC can be clearly observed. The ability to detect the target in the change detected image is, therefore, reduced under intensity image DLC as compared to complex image DLC.

Next, we investigate the performance of the various schemes under large target displacement between consecutive acquisitions. Consider the case where the person moves from position 1 to position 4. In this case, $L = 3$. Figure 24(a) shows the result of coherent change detection. Since the target undergoes large range migration, the moving target presents itself as two targets in the image. The noncoherent change detection results for the large target displacement case are presented in Fig. 24(b). We observe that the intensity image DLC retains the target at position 4 and removes the target at position 1. However, similar to the small target displacement case, the artifacts resulting from the background not being totally cancelled out render target detection difficult.

1.5   Conclusions

In this section, we presented recent algorithmic advances in through-the-wall radar imaging. First, considering ground-based EM sensing, we discussed two methods, namely, spatial filtering and EM modeling based solution, for mitigating the front wall return prior to application of the image formation methods. The spatial filtering technique builds on the strong correlation of wall EM responses across antenna array elements to reduce constant-type return that is typical of walls in monostatic illuminations. The spatial filter, thus, allows the follow-on beamforming to unmask and

image behind-the-wall targets that have limited spatial extent, such as humans, compared to walls without the need for *o priori* knowledge of the wall characteristics. A simple IIR notch filter with flexible design was compared with the fixed design MA subtraction filtering, commonly used in GPR. On the other hand, the EM modeling approach is wall-dependent and relies on accurate estimation of the wall parameters for suppression of the wall return. Extraction of the wall parameters and coherent subtraction of the modeled wall reflection was shown to significantly improve the signal-to- wall-clutter ratio.

Second, an approach to exploit the rich indoor multipath environment for improved target detection was described. A ray tracing approach was used to derive a multipath model, considering reflections inside an enclosed room comprising four homogeneous walls. Using the model, it was demonstrated analytically that the multipath corresponding to each sensor appeared on the wall but changes position from one sensor to another. Hence, a least squares technique was used to estimate its actual focusing location in both downrange and crossrange. The model was utilized to develop a multipath exploitation technique which associates multipath ghosts with their respective targets and maps them to their true target locations. This technique reduced the false positives in the original beamformed image as well as increased the signal-to-noise ratio at the true target locations.

Third, we discussed a change detection approach to moving target indication for through-the-wall applications. Change detection was used to mitigate the heavy clutter that is caused by strong reflections from exterior and interior walls. Both coherent and noncoherent change detection techniques were examined and their performance was compared under both consecutive and non-consecutive acquisitions. For non-consecutive acquisitions, the coherent CD scheme showed two sets of imaged targets corresponding to the positions of a single target at the two data acquisitions, whereas the noncoherent CD retained only one set of imaged targets, though with significantly more artifacts. For consecutive acquisitions, the coherent change detection provided better performance than the noncoherent CD, which removed most of the imaged target during the zero-thresholding step.

1.6 References

[1] Ahmad, F.; Amin, M. G. (2006). Noncoherent Approach to Through-the-Wall Radar Localization. *IEEE Transactions on Aerospace and Electronic Systems* 42(4), 1405-1419.

[2] Ahmad, F., Amin, M.G. (2005). A Noncoherent Radar System Approach for Through-The-Wall Imaging. In *Proc. SPIE - Sensors, ond Commond, Control, Communications, and Intelligence Technologies IV Conference*, Orlando, FL, 2005; vol. 5778, 196-207.

[3] Ahmad, F. and Amin, M. G. (2007). Performance of autofocusing schemes for single target and populated scenes behind unknown walls. In *Proceedings of SPIE - Radar Sensor Technology XI*, Orlando, FL, April, 2007; vol. 6547.

[4] Ahmad, F. and Amin, M.G. (2008). Multi-location wideband synthetic aperture imaging for urban sensing applications. *Journal of the Fronklin Institute* 345(6), 618-639.

[5] Ahmad, F., Amin, M.G. and Kassam, S.A. (2005). Synthetic aperture beamformer for imaging through a dielectric wall. *IEEE Tronsoctions on Aerospace and Electronic Systems* 41(1), 271-283.

[6] Ahmad, F., Amin, M.G., and Mandapati, G. (2007). Autofocusing of through-the-wall radar imagery under unknown wall characteristics. *IEEE Trons. Image Process.* 16 (7), 1785–1795.

[7] Ahmad, F., Frazer, G., Kassam, S. A., Amin, M. G. (2004). Design and implementation of near-field, wideband synthetic aperture beamformers. *IEEE Trons. Aerosp. Electron. Syst.* 40(1), 206-220.

[8]   Ahmad, F., Amin, M.G., and Zemany, P.D. (2007). Performance analysis of dual-frequency CW radars for motion detection and ranging in urban sensing applications. In *Praceedings of SPIE - Radar Sensor Technology XI*, Orlando, FL, April 2007; vol. 6547.

[9]   Ahmad, F., Amin, M.G., and Zemany, P.D. (2009). Dual-Frequency Radars for Target Localization in Urban Sensing. *IEEE Transoctions on Aerospoce ond Electronic Systems* 45 (4).

[10]   Ahmad, F., Amin, M.G., Setlur, P. (2006). Through-the-wall target localization using dual-frequency CW radars. In *Prac. SPIE - Sensars, and Command, Contral, Cammunicatians, and Intelligence (C3I) Technalogies Conference*, Orlando, FL, April 2006; vol. 6201.

[11]   Ahmad, F., Zhang, Y. and Amin, M. (2008). Three-dimensional wideband beamforming for imaging through a single wall. *IEEE Geascience and Remote Sensing Letters* 5(2), 176-179.

[12]   Alli, G. and DiFilippo, D. (2010). Beamforming for through-the-wall radar imaging. In Amin, M.G (ed.) Through-the-wall radar imaging. pp.81-120. Boca Raton, FL: CRC Press.

[13]   Amin, M.G. (Ed.) (2008). Special Issue on "Advances in indoor radar imaging". *Journol of the Franklin Institute* 345(6), 556-722.

[14]   Amin, M.G. (Ed.) (2010). Through-the-Wall Radar Imaging; CRC Press:Boca Raton, FL, 2010.

[15]   Amin, M. and Sarabandi, K. (Eds.) (2009). Special Issue on Remote Sensing of Building Interior. *IEEE Trons. on Geoscience ond Remote Sensing* 47(5), 1270-1420.

[16]   Barrie, G., Tunaley, J. (2003). An Analysis of Through- and In-the-Wall UWB Impulse Radar: System design considerations. Technical Memorandum TM 2003-134, Defence Research and Development Canada (DRDC).

[17]   Borek, S.E., An overview of through the wall surveillance for homeland security. In *Proceedings of the 34th, Applied Imogery ond Pottern Recognitian Warkshap*, October 2005; vol. 6, pp. 19–21.

[18]   Brunzell, H. (1999). Detection of shallowly buried objects using impulse radar. *IEEE Tronsoctions on Geoscience ond Remote Sensing* 37(2), 875–886.

[19]   Burkholder, R. J. (2008). Electromagnetic models for exploiting multi-path propagation in through-wall radar imaging. In: *Proceedings of the Internotionol Conference an Electramagnetics in Advanced Applicotions*, pp. 572-575. Torino, Italy: IEEE.

[20]   Chandra, R., Gaikwad, A.N., Singh, D., and Nigam, M.J. (2008). An approach to remove the clutter and detect the target for ultra-wideband through wall imaging. *Journol of Geaphysics ond Engineering* 5(4), 412–419.

[21]   Chang, P.C., Burkholder, R.J., Volakis, J.L., Marhefka, R.J., Bayram, Y. (2009). High-Frequency EM Characterization of Through-Wall Building Imaging. *IEEE Transoctions on Geascience and Remate Sensing* 47(5), 1375-1387.

[22]   Çetin, M., Karl, W., and Castañon, D. Evaluation of a regularized SAR imaging technique based on recognition-oriented features, Proceedings of the SPIE – Algorithms for SAR Imagery VII, Orlando, FL, Apr. 2000; vol. 4053, pp. 40–51.

[23]   Curlander, J.C. and McDonough, R.N. Synthetic Aperture Radar-Systems and Signal Processing; Wiley: New York, 1991.

[24]   Dehmollaian, M. and Sarabandi, K. (2008a). Refocusing through building walls using synthetic aperture radar. *IEEE Tronsoctians an Geoscience ond Remote Sensing* 46(6), 1589–1599.

[25]   Dehmollaian, M. and Sarabandi, K. (2008b). Analytical, numerical, and experimental methods for through-the-wall radar imaging, *Proceedings af the IEEE Internotional Canference on Acoustics, Speech, and Signal Processing*, Las Vegas, NV, Apr. 2008; pp. 5181–5184.

[26]   Dehmollaian, M., Sarabandi, K. (2008c). An Approximate Solution of Scattering from Reinforced Concrete Walls Using An Analytic 1-D Periodic Green's Function. *IEEE Transactians on Antennas and Prapogotion* 56(8), 2681-2690.

[27]   Dehmollaian, M., Thiel, M., and Sarabandi, K. (2009). Through-the-wall imaging using differential SAR. *IEEE Tronsoctions an Geascience ond Remote Sensing* 47(5), 1289 – 1296.

[28]   Dogaru, T. and Le, C. (2008). Validation of Xpatch computer models for human body radar signature. U.S. ARL technical report ARL-TR-4403, Adelphi, MD, 2008.

[29] Dogaru, T. and Le, C. (2009). SAR images of rooms and buildings based on FDTD computer models. *IEEE Tronsoctions on Geoscience ond Remote Sensing* 47(5), 1388-1401.

[30] Dogaru, T. and Le, C. (2009a). Through-the-wall small weapon detection based on polarimteric radar techniques. U.S. ARL technical report ARL-TR-5041, Adelphi, MD, 2009.

[31] Falconer, D.G., Ficklin, R.W., and Konolige, K.G., Robot-mounted through-wall radar for detecting, locating, and identifying building occupants. In Proceedings of the IEEE International Conf. on Robotics and Automation, 2000; pp. 1868–1875.

[32] Ferris Jr., D.D. and Currie, N.C., A survey of current technologies for through-the-wall surveillance (TWS). In *Proceedings of the SPIE - Sensors, C31 Information, ond Troining Technologies for Low Enforcement*, Boston, MA, Nov. 1998; vol. 3577, pp 62–72.

[33] Fontana, R.J. (2004). Recent system applications of short-pulse ultra-wideband (UWB) technology. *IEEE Trons. Microwove Theory Tech.* 52 (9).

[34] Frazier, L.M. (1996). Surveillance through walls and other opaque materials. In Proceedings of the IEEE National Radar Conference, 1996; pp. 27-31.

[35] Frazier, L.M. (2004). Motion detection radar (MDR) for law enforcement. *IEEE Potentials* 16(5), 3079–3082.

[36] Greneker, E.F. (1998). RADAR flashlight for through-the-wall detection of humans. In Proceedings of the SPIE – Targets Backgrounds: Charact. Representation IV, 1998; vol. 3375, 280–285.

[37] Greneker, E. F., Rausch, E. O. (2008). Wall characterization for through-the-wall radar applications. In Proc. SPIE - Radar Sensor Technology XII conference, Orlando, FL, April 2008; vol. 6947.

[38] Goodman, J. W. (1996). Introduction to Fourier Optics; McGraw-Hill: New York, 1996.

[39] Gustaffson, F. (1996). Determining the initial states in forward-backward filtering. *IEEE Tronsoctions on Signal Processing* 44(4), 988–992.

[40] Hunt, A.R. (2005). Image formation through walls using a distributed radar sensor network. In *Proceedings of the SPIE - Loser Phys. Photonics, Spectrosc., Mol. Modeling V*, 2005; vol. 5778, pp. 169–174.

[41] Hunt, A. R. (2009). Use of a frequency-hopping radar for imaging and motion detection through walls. *IEEE Tronsoctions on Geoscience and Remote Sensing* 47(5), 1402-1408.

[42] Kak, A.C. and Slaney (1988). M. Principles of Computerized Tomographic Imaging; IEEE Press: New York, 1988.

[43] Kidera, S., Sakamoto, T. and Sato, T (2009). Experimental study of shadow region imaging algorithm with multiple scattered waves for UWB radars. *Progress in Electromognetics Research* 5(4), 393-296.

[44] Komanduri, V. R., Hoorfar, A., Engheta, N. (2005). Low-Profile Array Design Considerations for Through-the-Wall Microwave Imaging Applications. In Proceedings of the IEEE Int. AP-S Symposium. Washington DC, July 2005.

[45] Kong, J. A. (2000). Electromagnetic Wave Theory; EMW Publishing: Cambridge, MA, 2000.

[46] Lai, C. P. and Narayanan, R. M. (2005). Through-wall imaging and characterization of human activity using ultrawideband (UWB) random noise radar, Proceedings of the SPIE—Sensors and C3I Technologies for Homeland Security and Homeland Defense, Orlando, FL, May 2005; vol. 5778, pp. 186-195.

[47] Lai, C. P., Narayanan, R. M. (2010). Ultrawideband random noise radar design for through-wall surveillance. *IEEE Transactions on Aerospoce ond Electronic Systems* 46(4), pp. 1716-1730.

[48] Lukin, K., Konovalov, V. Through wall detection and recognition of human beings using noise radar sensors. In *Proc. NATO RTO SET Symposium on Torget Identification ond Recognition Using RF Systems*, Oslo, Norway, Oct. 2004; P15.1–P15.12.

[49] Maaref, N. , Millot, P., Pichot, C., and Picon, O. (2009). A study of UWB FM-CW Radar for the detection of human beings in motion inside a building. *IEEE Tronsoctions on Geoscience ond Remote Sensing* 47(5), 1297 – 1300.

[50] Martone, A., Ranney, K. and Innocenti, R. (2009). Through-the-wall detection of slow-moving personnel. In Proceedings of the SPIE—Radar Sensor Technology XIII, Orlando, FL, April 13-17, 2009; 7308, 73080Q1-73080Q12.

[51] McEwan, T.E. (1994). Ultra-wideband radar motion sensor, U.S. Patent 5,361,070, 1994.

[52] Moulton, J. , Kassam, S.A., Ahmad, F., Amin, M.G., and Yemelyanov, K. (2008). Target and change detection in synthetic aperture radar sensing of urban structures. In Proceedings of IEEE Radar Conference, Rome, Italy, May26-30, 2008.

[53] Muqaibel, A., Ahmad Safaai-Jazi (2008). Characterization of wall dispersive and attenuative effects on UWB radar signals. *Journol of the Fronklin Institute* 345, 640–658.

[54] Nag, S., Barnes, M.A., Payment., T., and Holladay, G. (2002). An ultra-wideband through-the-wall radar for detecting the motion of people in real time. In Proceedings of the SPIE - Radar Sensor Technology and Data Visualization, Orlando, FL, April 2002; vol. 4744, pp.48–57.

[55] Narayanan, R. M., Shastry, M. C., Chen, P. H., Levi, M. (2010). Through-the-wall detection of stationary human targets using Doppler radar. *Progress in Electromagnetics Research B* 20, 147-166.

[56] Orovic, I., Stankovic, S., and Amin, M. (2011). A new approach for classification of human gait based on time-frequency feature representations. *Signol Processing* 91(6), 1448-1456.

[57] Ram, S. S., Li, Y., Lin, A., and Ling, H. (2008). Doppler-based detection and tracking of humans in indoor environments. *Journal of the Fronklin Institute* 345(6), 679–699.

[58] Ram, S. S. and Ling, H. (2008). Through-wall tracking of human movers using joint Doppler and array processing. *IEEE Geoscience ond Remote Sensing Letters* 5(3), 537-541.

[59] Ranney, K. et al. (2008). Recent MTI experiments using ARL's Synchronous Impulse Reconstruction (SIRE) Radar, Proceedings of the SPIE—Radar Sensor Technology XII, Orlando, FL, April 2008; vol. 6947, pp. 694708-1–694708-9.

[60] Robinson, E.A. and Treitel, S. (1980). Geophysical Signal Analysis; Prentice-Hall: Englewood Cliffs, NJ, 1980.

[61] Setlur, P. (2010). *Stotisticol algorithms and bounds far moving targets in urbon sensing ond thraugh-the-woll rodor opplicotions*. PhD Thesis: Villanova University.

[62] Setlur, P., Ahmad, F., Amin, M.G., and Zemany, P.D. (2007), Experiments on through-the-wall motion detection and ranging. In *Praceedings af the SPIE - Cammand, Control, Communications, ond Intelligence (C3I) Technologies for Homelond Security ond Homelond Defense VI*, Orlando, FL, April 2007; vol. 6538.

[63] Setlur, P., Amin, M.G., and Ahmad, F. (2011). Multipath model and exploitation in through-the-wall and urban radar sensing. *IEEE Tronsoctions on Geoscience ond Remote Sensing* 49(10), 4021-4034.

[64] Setlur, P., Amin, M.G., and Thayaparan, T. (2005). Micro-doppler signal estimation for vibrating and rotating targets. In *Proc. Eighth Int. Sympasium on Signol Processing ond its Applicatians*, Sydney, Australaia, August 2005.

[65] Sévigny, P. et al. (2010). Concept of operation and preliminary experimental results of the DRDC through-wall SAR system. In Proceedings of the SPIE—Radar Sensor Technology XIV, Orlando, FL, April 2010; vol. 7669, pp. 766907-1– 766907-11.

[66] Skolnik, M. (2001). Introduction to Radar Systems, 3rd Ed.; McGraw Hill: New York, 2001.

[67] Song, L. P., Yu, C., Liu, Q. H. (2005). Through-wall imaging (TWI) by radar: 2-D tomographic results and analyses. *IEEE Trons. Geosci. Remote Sensing* 43 (12), 2793–2798.

[68] Soldovieri, F., Solimene, R. (2007). Through-wall imaging via a linear inverse scattering algorithm. *IEEE Geoscience and Remote Sensing Letters* 4(4), 513-517.

[69] Soldovieri, F., Solimene, R., and Pierri, R. (2009). A simple strategy to detect changes in through the wall imaging. *Progress In Electramagnetics Reseorch M* 7, 1–13.

[70] Soldovieri, F., Ahmad, F., Solimene, R. (2011). Validation of microwave tomographic inverse scattering approach via through-the-wall experiments in semi-controlled conditions. *IEEE Geoscience and Remote Sensing Letters* 8(1), 123-127.

[71] Solimene, R., Ahmad, F., Soldovieri, and F. (2012). A novel CS-SVD strategy to perform data reduction in linear inverse scattering problems. *IEEE Geoscience and Remote Sensing Letters* 9(5), 881-885.

[72] Tahmoush, D., Silvious, J. (2009). Stride rate in radar micro-doppler images, in *Proceedings of the IEEE International Conference on Systems, Man, and Cybernetics*, San Antonio, TX, October 11-14, 2009, pp. 4218-4223.

[73] Thajudeen, C. and Hoorfar, A. (2010). A Comparative study of wall parameter estimation and mitigation techniques. In Proceedings of the 2010 USNC/URSI Meeting, Toronto, Canada, July 2010.

[74] Thajudeen, C., Hoorfar, A., Ahmad, F., Dogaru, T. (2011). Measured complex permittivity of walls with different hydration levels and the effect on power estimation of TWRI target returns. *Progress in Electromagnetic Research B* 30, 177-199.

[75] Thayaparan, T., Stankovic, L. and Djurovic, I. (2008). Micro-Doppler human signature detection and its application to gait recognition and indoor imaging. *Journal of the Franklin Institute* 345(6), 700–722.

[76] Thiel, M., Sarabandi, K. (2011). Ultrawideband Multi-Static Scattering Analysis of Human Movement Within Buildings for the Purpose of Stand-Off Detection and Localization. *IEEE Transactions on Antennas and Propagation* 59(4), 1261-1268.

[77] Tivive, F.H.C., Bouzerdoum, A., and Amin, M.G. (2011). An SVD-based Approach for Mitigating Wall Reflections in Through-the-Wall Radar Imaging, in *Proceedings of the IEEE Radar Conference*, Kansas City, MO, May 23-27, 2011, pp. 519-524.

[78] Tyson, R.K. (1998). Principles of Adaptive Optics, 2nd Ed.; Academic Press:Boston, MA, 1998.

[79] Vaccaro, R.J. (1998). The past, present, and the future of underwater acoustic signal processing. *IEEE Signal Processing Magazine* 15 (4), 21–51.

[80] Venkatasubramanian, V., Leung, H. (2009). Chaos UWB radar for through-the-wall imaging. *IEEE Transactions on Image Processing* 18(6), 1255-1265.

[81] Verma, P.K., Gaikwad, A.N., Singh, D., and Nigam, M.J. (2009). Analysis of clutter reduction techniques for through wall imaging in UWB range. *Progress in Electromagnetics Research B* 17, 29–48.

[82] Wang, G., Amin, M.G., and Zhang, Y. (2006). A new approach for target locations in the presence of wall ambiguity. *IEEE Transactions on Aerospace and Electronic Systems* 42(1), 301-315.

[83] Yang, Y., Fathy, A.E. (2009). Development and Implementation of a Real-Time See-Through-Wall Radar System Based on FPGA. *IEEE Transactions on Geoscience and Remote Sensing* 47(5), 1270-1280.

[84] Yemelyanov, K.M., Engheta, N., Hoorfar, A., McVay, J.A. (2009). Adaptive Polarization Contrast Techniques for Through-Wall Microwave Imaging Applications. *IEEE Transactions on Geoscience and Remote Sensing* 47(5),1362-1374.

[85] Yoon, Y.-S. and Amin, M.G. (2008a). High-Resolution Through-the-Wall Radar Imaging using Beamspace MUSIC. *IEEE Transactions on Antennas and Propagation* 56(6), 1763-1774.

[86] Yoon, Y., Amin, M.G., Ahmad, F. (2011). MVDR Beamforming for Through-the-Wall Radar Imaging. *IEEE Transactions on Aerospace and Electronic Systems* 47(1), 347-366.

[87] Yoon, Y.-S. and Amin, M. G. (2009). Spatial Filtering for Wall-Clutter Mitigation in Through-the-Wall Radar Imaging. *IEEE Transactions on Geoscience and Remote Sensing* 47(9), 3192 - 3208.

[88] Zhang, J. and Huang, Y. (1999). Extraction of dielectric properties of building materials from free-space time-domain measurement, *Proceedings of High Frequency Postgraduate Student Colloq.*, Sep. 1999, pp. 127–132.

[89] Zhang, W., Hoorfar, A., Thajudeen, C. , Ahmad, F. (2010). Full polarimetric beamforming algorithm for through-the-wall radar imaging. *Radio Science* 46(RS0E16), doi:10.1029/2010RS004631.

[90]   Zhang, Y. D. and Hunt, A. (2010). Image and localization of behind-the-wall targets using collocated and distributed apertures. In Through-the-Wall Radar Imaging; Amin, M.G. Ed.; CRC Press:Boca Raton, FL, 2010, Chapter 4; pp. 121-156.

[91]   Zhang, Y., Amin, M.G., Ahmad, F. (2008). Time-frequency analysis for the localization of multiple moving targets using dual-frequency radars. *IEEE Signal Processing Letters* 15, 777-780.
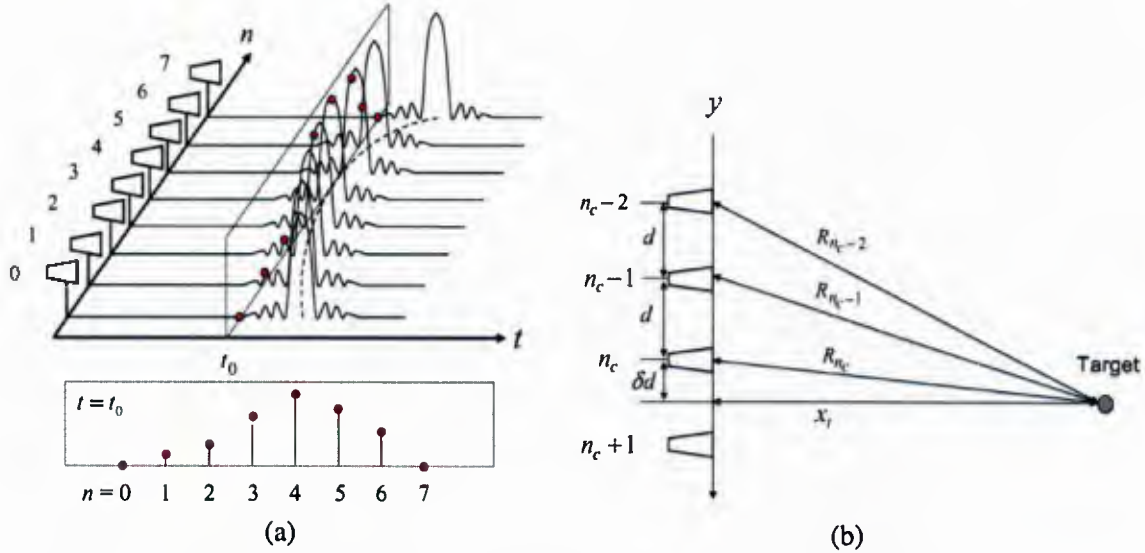
Figure 1. Received signals using SAR data collection scheme. (a) Array signal at $t = t_0$. (b) Range between antenna locations and the target.
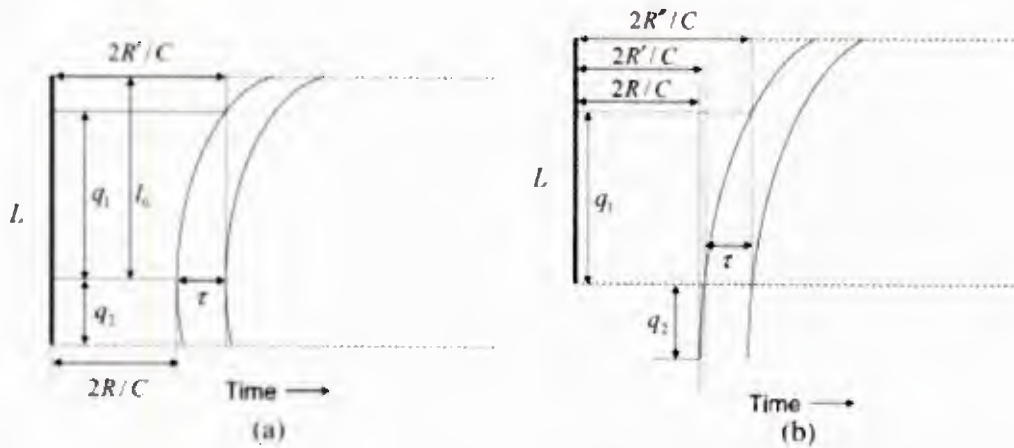
Figure 2. Target return signal in the time-space domain. (a) Target is within the array aperture. (b) Target is outside the array aperture
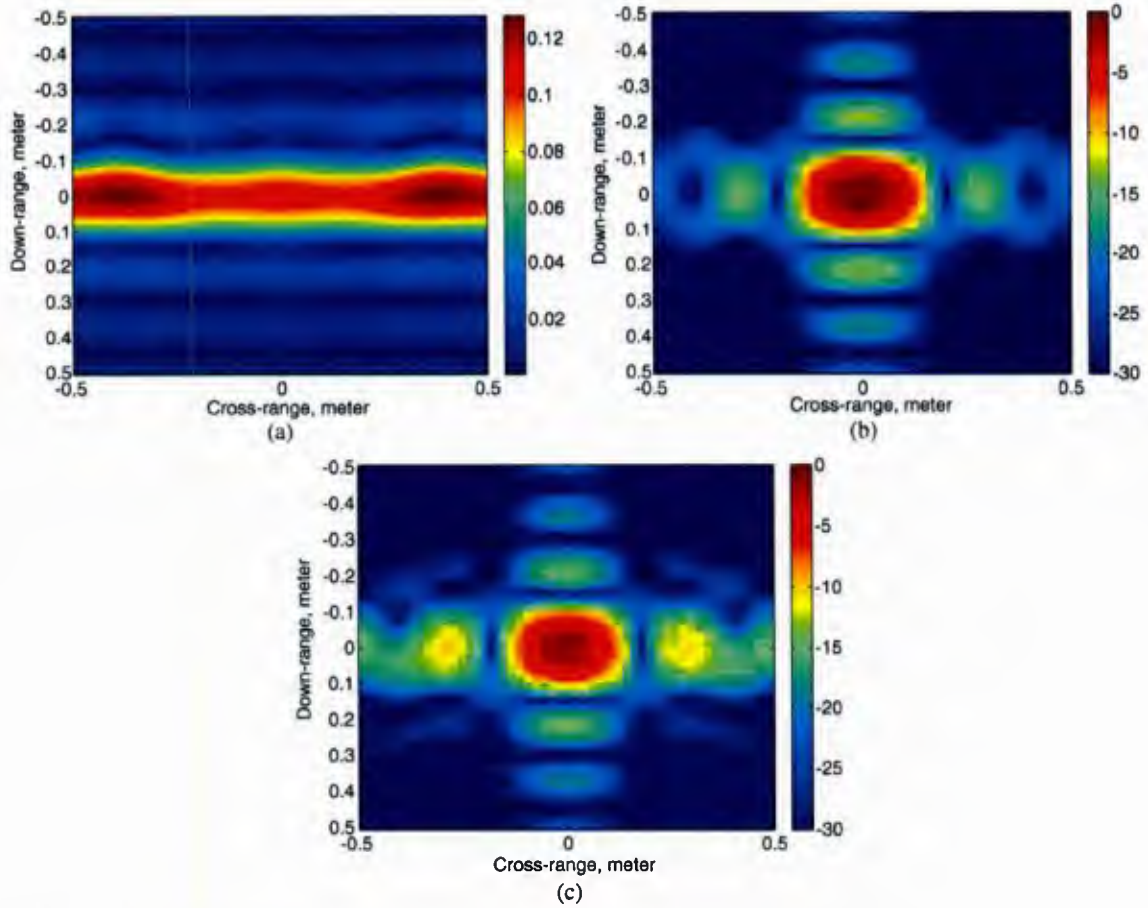
Figure 3. Modification in the PSF due to MA subtraction. (a) Second term in (19). (b) PSF without filtering. (c) PSF after MA subtraction.
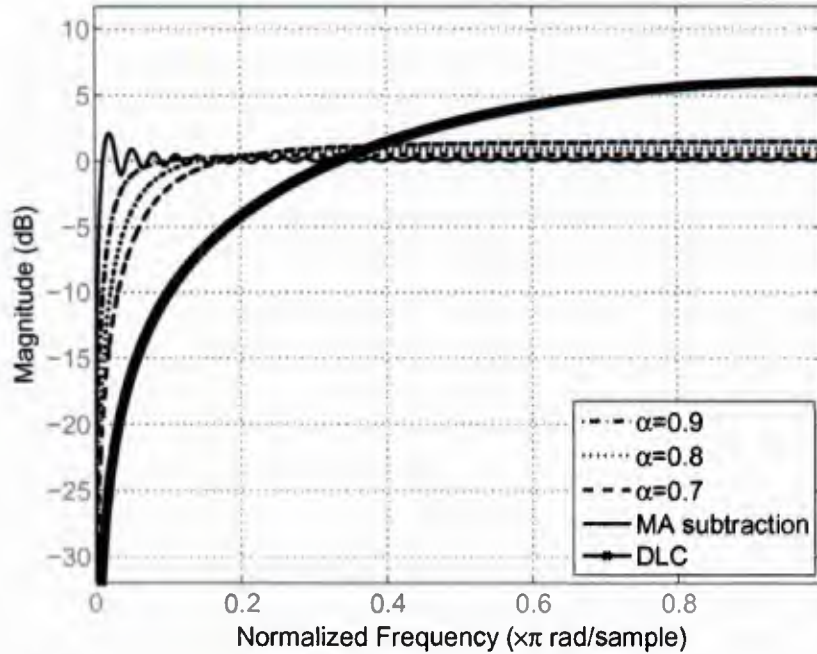
Figure 4. Frequency response of the notch filter for various α, DLC with two pulses, and MA subtraction with 67 antennas.
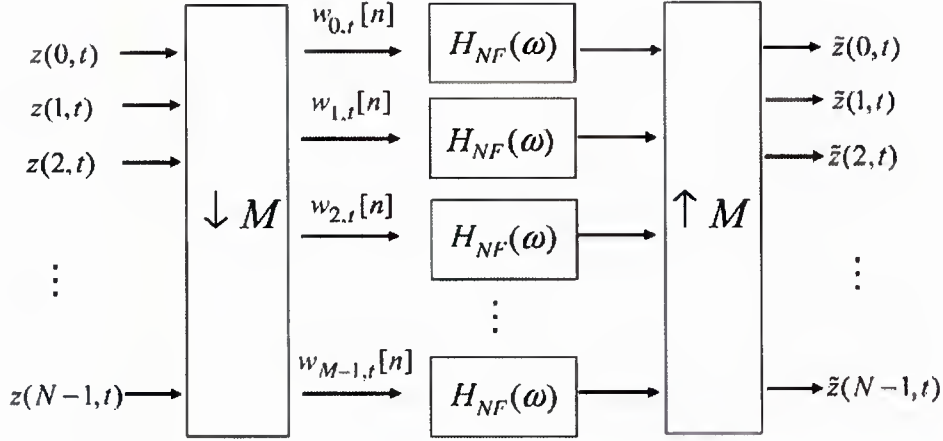
Figure 5. Block diagram of notch filtering

(a)

(b)

(c)
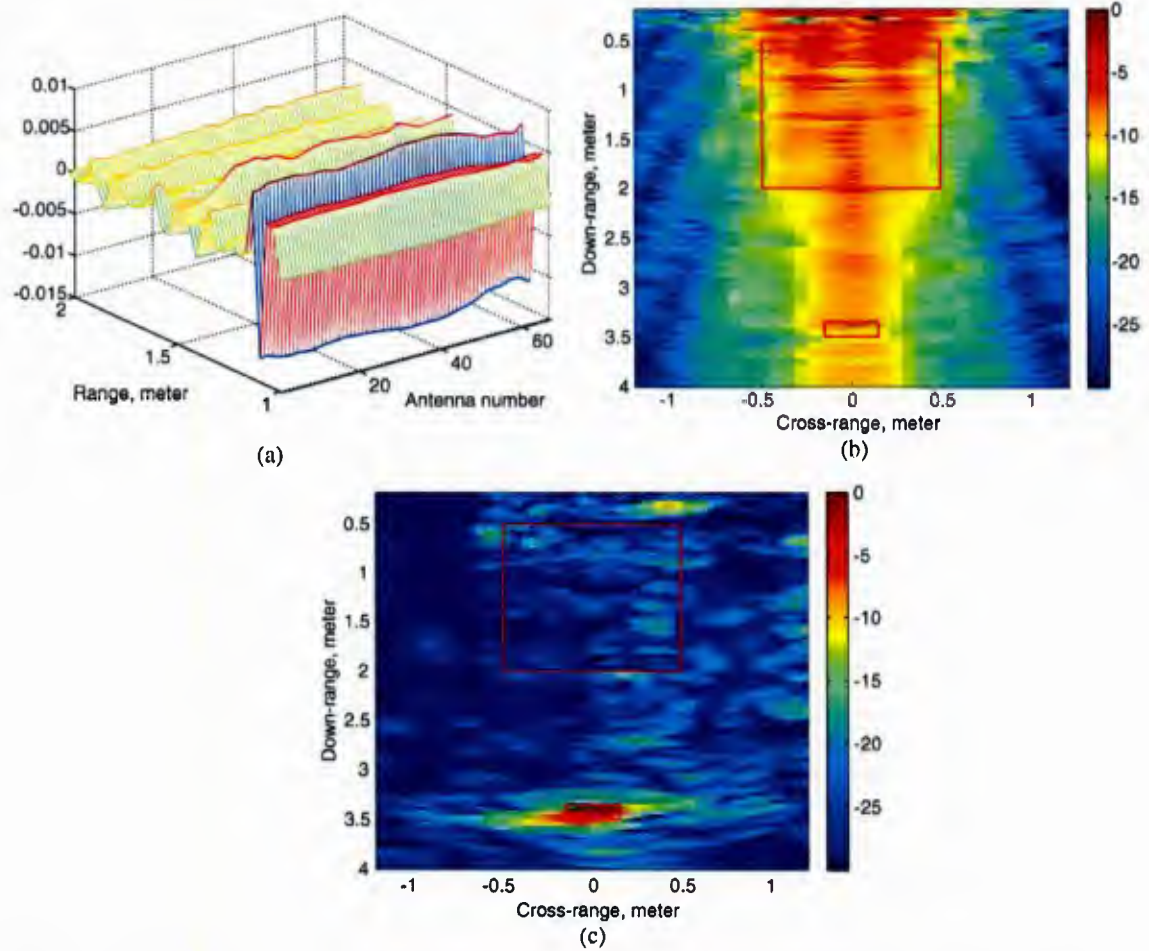
Figure 6. (a) Wall reflections of the solid concrete wall in time domain across the antenna positions. (b) DS image with wall reflections. (c) DS image with background subtraction.
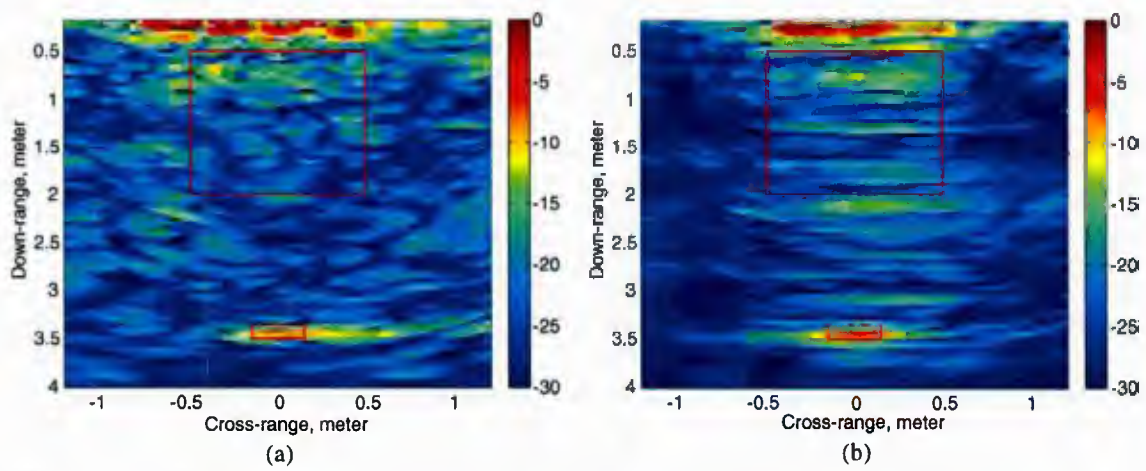
Figure 7. DS images for solid concrete wall. (a) MA subtraction. (b) Spatial notch filtering.

(a)   (b)

Figure 8. (a) Side view of the measurement setup. (b) Trihedral target.
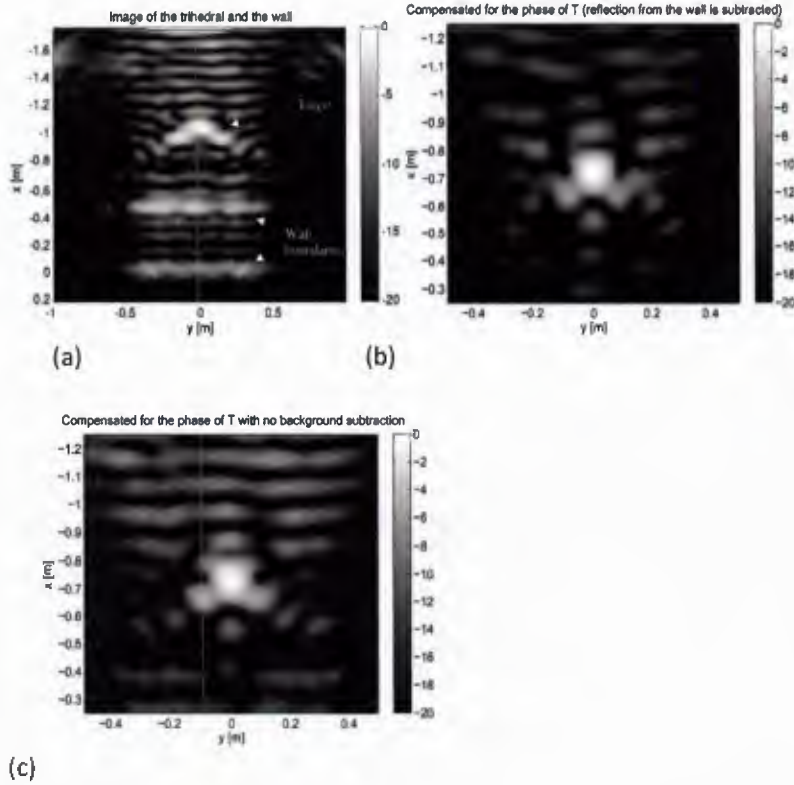
Figure 9. (a) Image of the trihedral behind wall using full received data and free-space image formation. (b) Image of trihedral after estimated wall return subtraction and wall compensation. (c) Image of trihedral after wall compensation.
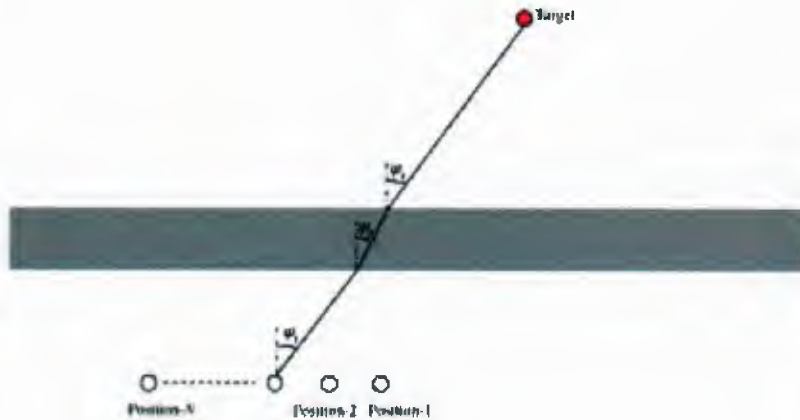
Fig. 10. Through-the-wall synthetic aperture radar model.
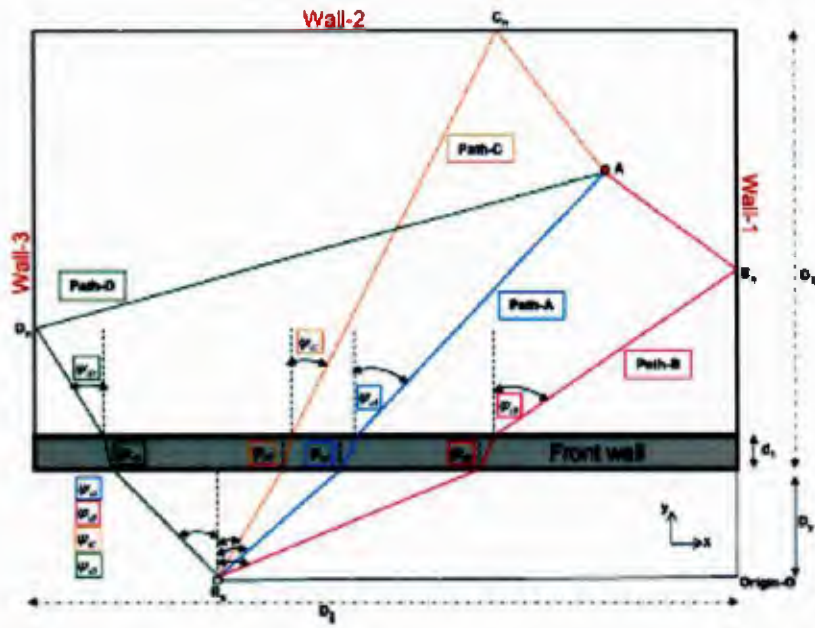
Fig. 11. Multipath model.
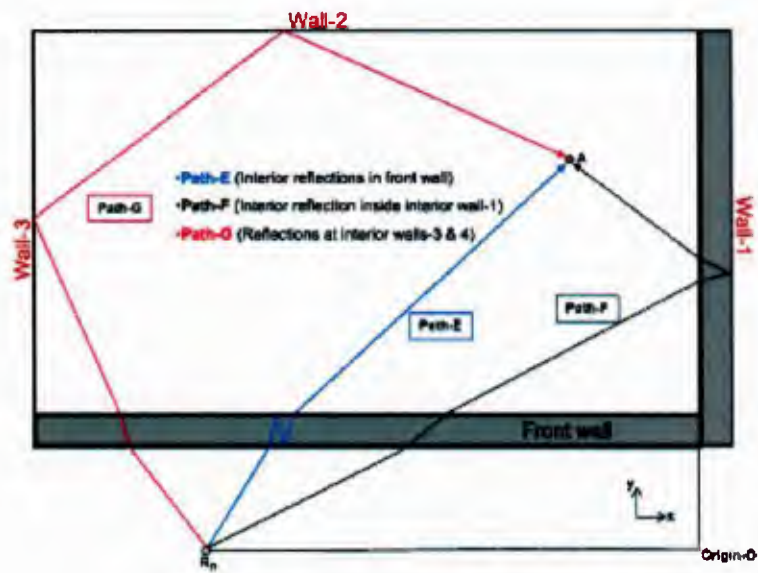
Fig. 12. Other higher order paths.
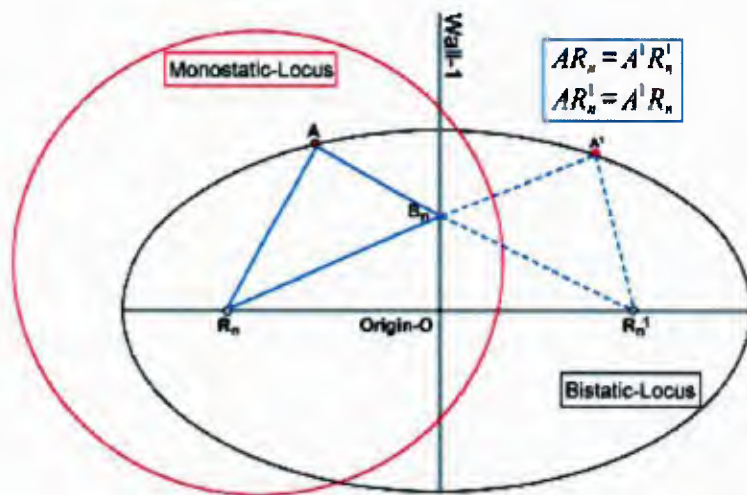
Fig. 13. The equivalence between the bistatic and monostatic geometries.
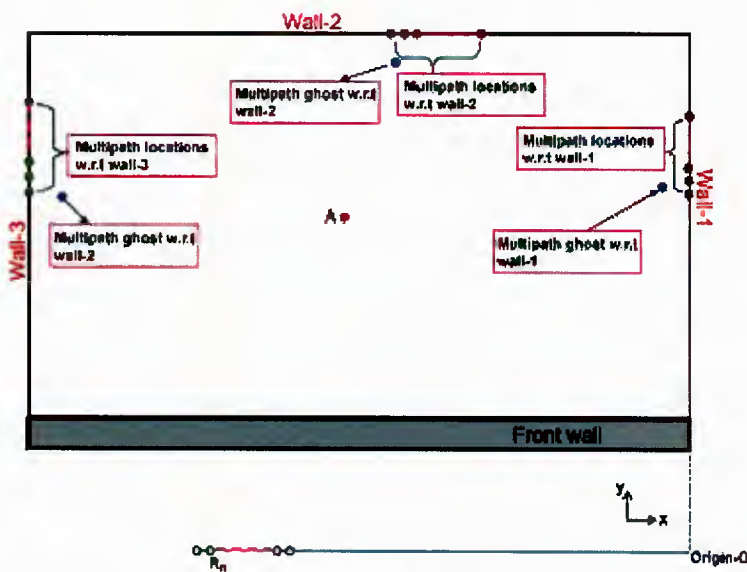
Fig. 14. Multipath locations and imaged location of multipath ghosts.
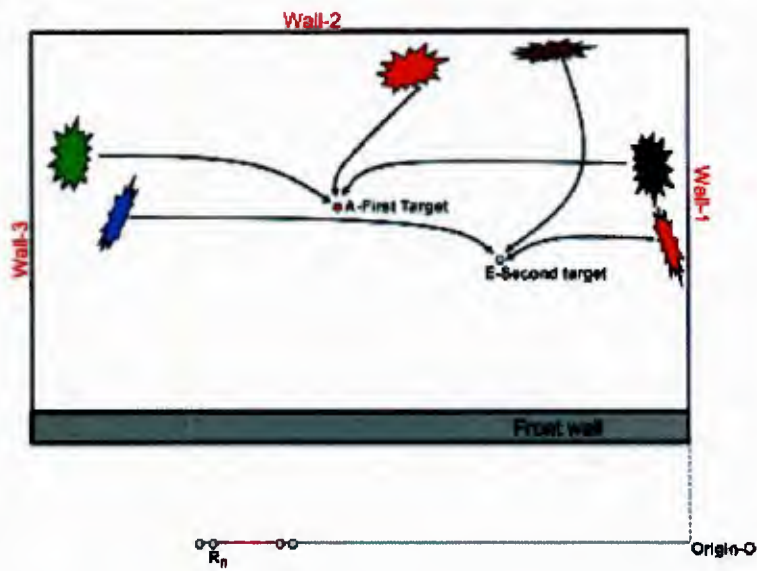
Fig. 15. Multipath exploitation principle.
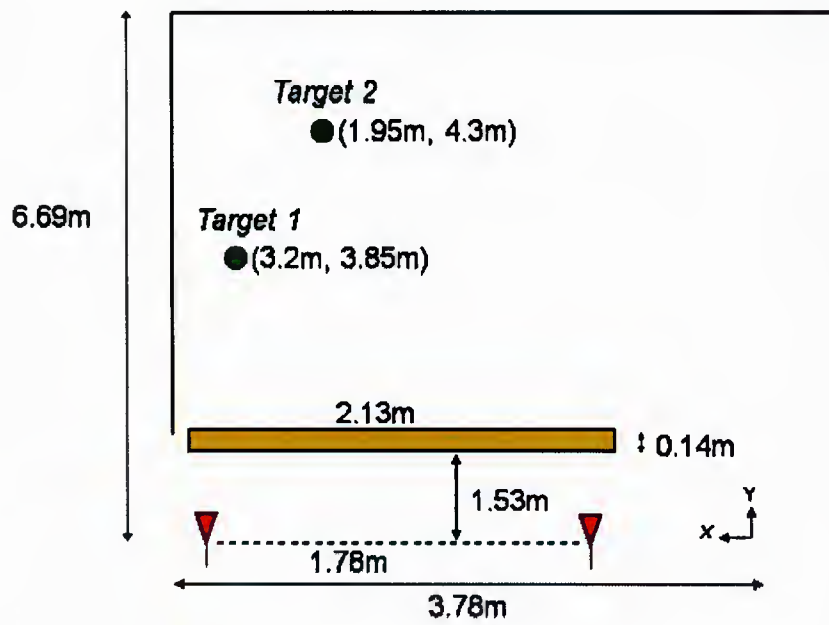
Fig. 16. Scene Layout

<center>(a)   (b)</center>
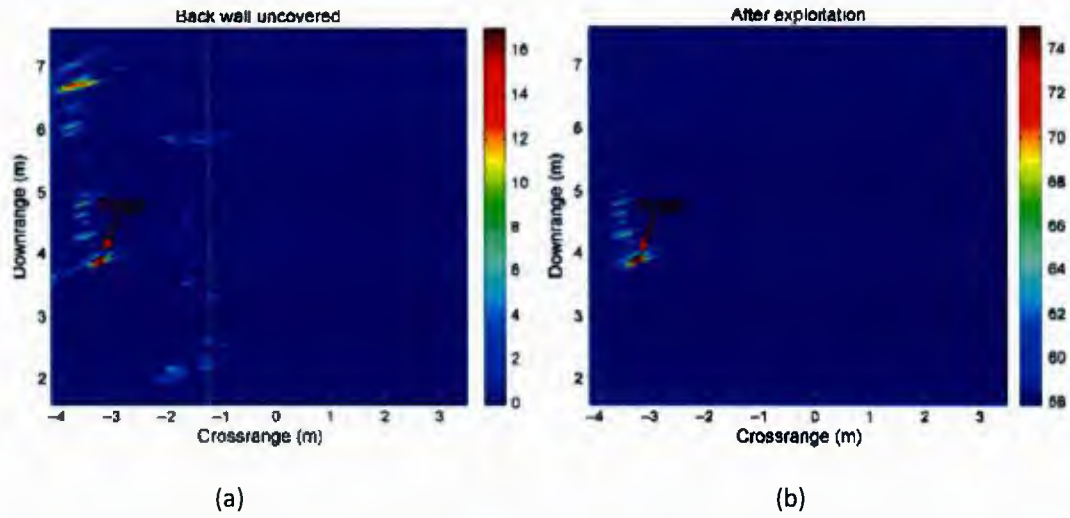
Fig. 17. Single target experiment: (a) Original, (b) after multipath exploitation.
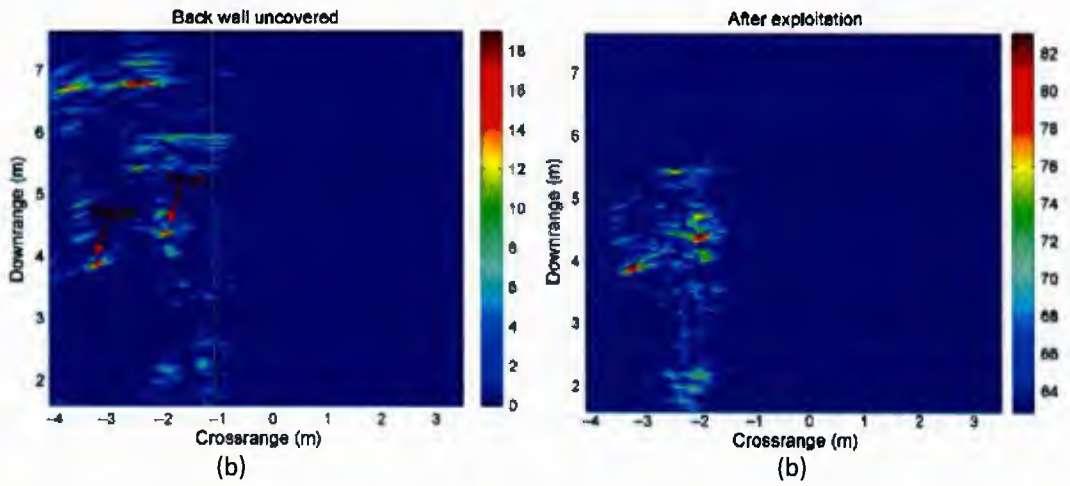

<center>(b)   (b)</center>

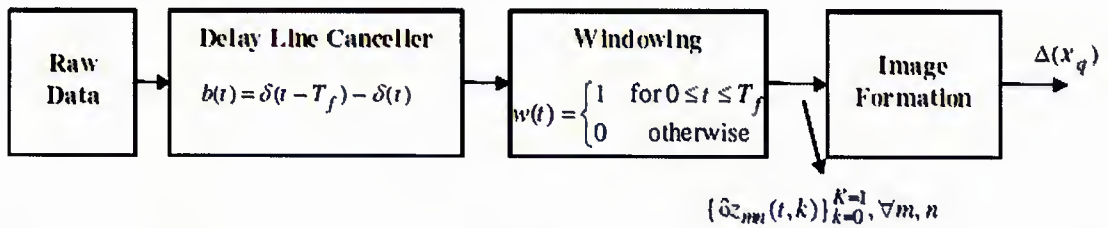Fig. 18. Two target experiment: (a) Original , (b) after multipath exploitation.

Figure 19. Block diagram of the data domain CD approach, equivalent to complex amplitude image subtraction (coherent CD).
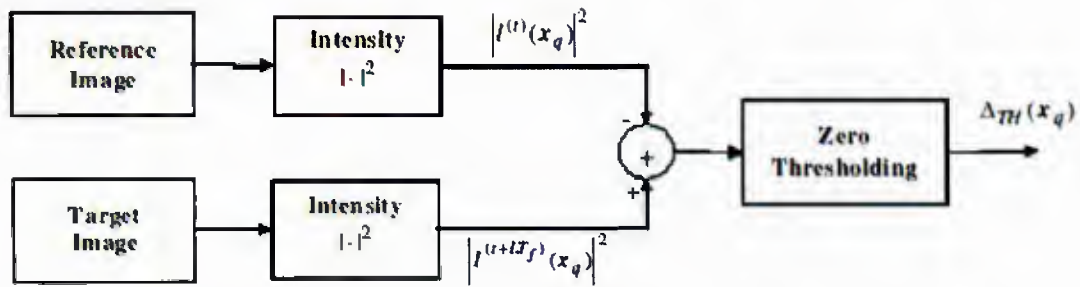
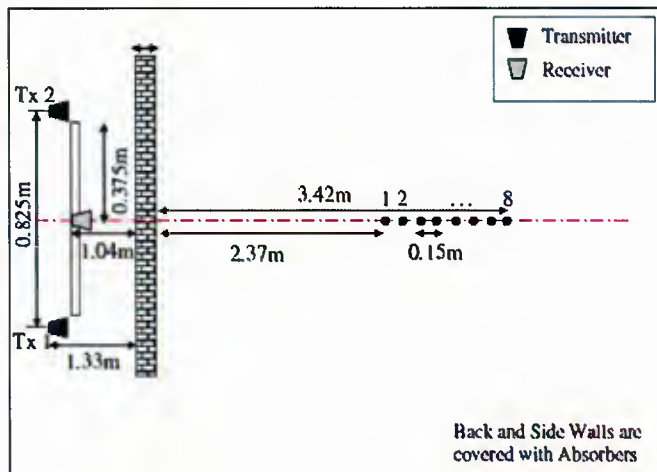Figure 20. Block diagram of the noncoherent change detection approach.

Figure 21. Layout of the scene and target trajectory.

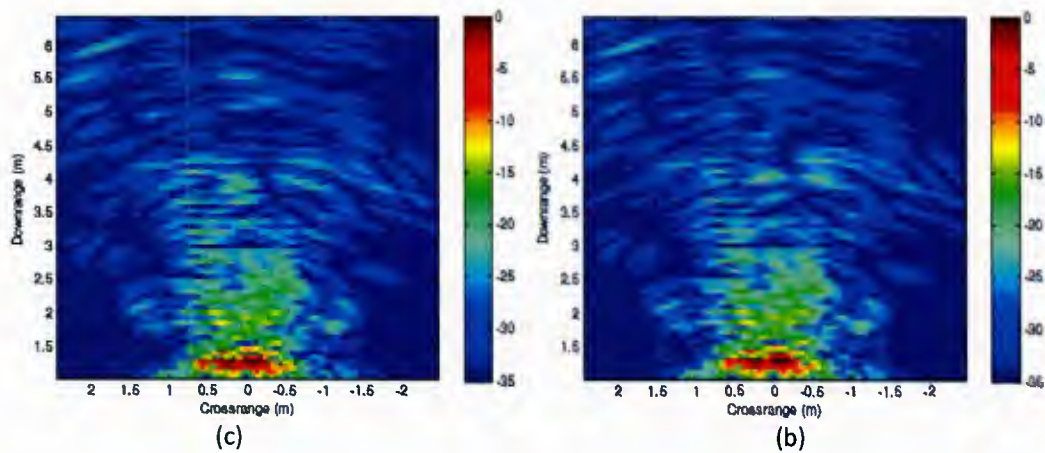(c)   (b)

Figure 22. Beamformed images for the target at position (a) 3 and (b) 4 (consecutive range cells).
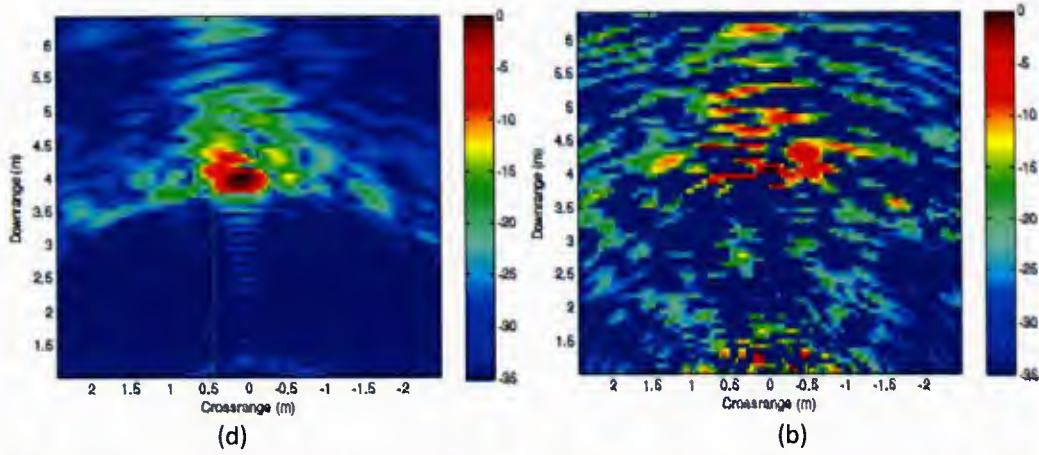
Figure 23. Images after change detection under (a) coherent CD and (b) noncoherent CD for the human walking from position 3 to position 4.
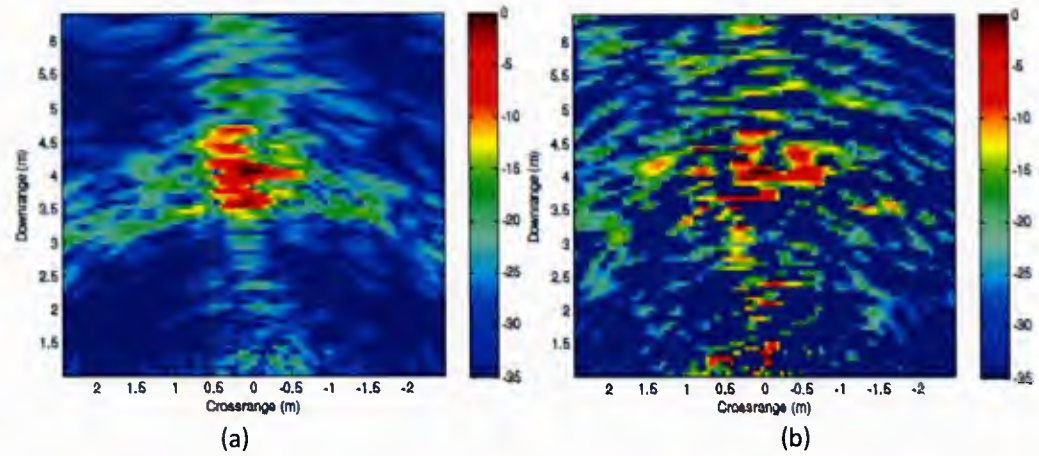

Figure 24. Images after change detection under (a) coherent CD and (b) noncoherent CD for the human walking from position 1 to position 4.

Section 2 - Compressive Sensing for Through-the-Wall Radar Imaging

2.1   Introduction

Through-the-wall radar imaging (TWRI) is an emerging technology that addresses the desire to see inside buildings using electromagnetic (EM) waves for various purposes, including determining the building layout, discerning the building intent and nature of activities, locating and tracking the occupants, and even identifying and classifying inanimate objects of interest within the building. TWRI is highly desirable for law enforcement, fire and rescue, and emergency relief, and military operations [1–6].

Applications primarily driving TWRI development can be divided based on whether information on motions within a structure or on imaging the structure and its stationary contents is sought out. The need to detect motion is highly desirable to discern about the building intent and in many fire and

44

hostage situations. Discrimination of movements from background clutter can be achieved through change detection (CD) or exploitation of Doppler [7–24]. One-dimensional motion detection and localization systems employ a single transmitter and receiver and can only provide range-to-motion, whereas two- and three-dimensional multi-antenna systems can provide more accurate localization of moving targets. The 3-D systems have higher processing requirements compared to 2-D systems. However, the third dimension provides height information, which permits distinguishing people from animals, such as household pets. This is important since radar cross section alone for behind-the-wall targets can unreliable.

Imaging of structural features and stationary targets inside buildings requires at least 2-D and preferably 3-D systems [25–43]. Because of the lack of any type of motion, these systems cannot rely on Doppler processing or CD for target detection and separation. Synthetic aperture radar (SAR) based approaches have been the most commonly used algorithms for this purpose. Most of the conventional SAR techniques usually neglect propagation distortions such as those encountered by signals passing through walls [44]. Distortions degrade the performance and can lead to ambiguities in target and wall localizations. Free-space assumptions no longer apply after the EM waves propagate through the first wall. Without factoring in propagation effects, such as attenuation, reflection, refraction, diffraction, and dispersion, imaging of contents within buildings will be severely distorted. As such, image formation methods, array processing techniques, target detection, and image sharpening paradigms must work in concert and be reexamined in view of the nature and specificities of the underlying sensing problem.

In addition to exterior walls, the presence of multipath and clutter can significantly contaminate the radar data leading to reduced system capabilities for imaging of building interiors and localization and tracking of targets behind walls. The multiple reflections within the wall result in wall residuals along the range dimension. These wall reverberations can be stronger than target reflections, leading to its masking and undetectability, especially for weak targets close to the wall [45]. Multipath stemming from multiple reflections of EM waves off the targets in conjunction with the walls may result in the power being focused at pixels different than those corresponding to the target. This gives rise to ghosts, which can be confused with the real targets inside buildings [46–49]. Further, uncompensated refraction through walls can lead to localization or focusing errors, causing offsets and blurring of imaged targets [26, 39]. SAR techniques and tomographic algorithms, specifically tailored for TWRI, are capable of making some of the adjustments for wave propagation through solid materials [26–30, 36–41, 50–57]. While such approaches are well suited for shadowing, attenuation, and refraction effects, they do not account for multipath as well as strong reflections from the front wall.

The problems caused by the front wall reflections can be successfully tackled through wall clutter mitigation techniques. Several approaches have been devised, which can be categorized into those based on estimating the wall parameters and others incorporating either wall backscattering strength or invariance with antenna location [39, 45, 58–61]. In [39, 58], a method to extract the dielectric constant and thickness of the non-frequency dependent wall from the time-domain scattered field was presented. The time-domain response of the wall was then analytically modeled and removed from the data. In [45], a spatial filtering method was applied to remove the dc component corresponding to the constant-type radar return, typically associated with the front wall. The third method, presented in [59–61], was based not only on the wall scattering invariance along the array but also on the fact that wall reflections are relatively stronger than target reflections. As a result, the wall subspace is usually captured in the most dominant singular values when applying singular value decomposition (SVD) to the measured data matrix. The wall contribution can then be removed by orthogonal subspace projection.

Several methods have also been devised for dealing with multipath ghosts in order to provide proper representation of the ground truth. Earlier work attempted to mitigate the adverse effects stemming

from multipath propagation [27]. Subsequently, research has been conducted to utilize the additional information carried by the multipath returns. The work in [49] considered multipath exploitation in TWRI, assuming prior knowledge of the building layout. A scheme taking advantage of the additional energy residing in the target ghosts was devised. An image was first formed, the ghost locations for each target were calculated, and then the ghosts were mapped back onto the corresponding target. In this way, the image became ghost-free with increased signal-to-clutter ratio (SCR).

More recently, the focus of the TWRI research has shifted towards addressing constraints on cost and acquisition time in order to achieve the ultimate objective of providing reliable situational awareness through high-resolution imaging in a fast and efficient manner. This goal is primarily challenged due to use of wideband signals and large array apertures. Most radar imaging systems acquire samples in frequency (or time) and space, and then apply compression to reduce the amount of stored information. This approach has three inherent inefficiencies. First, as the demands for high resolution and more accurate information increase, so does the number of data samples to be recorded, stored, and subsequently processed. Second, there are significant data redundancies not exploited by the traditional sampling process. Third, it is wasteful to acquire and process data samples that will be discarded later. Further, producing an image of the indoor scene using few observations can be logistically important, as some of the measurements in space and frequency or time can be difficult, unavailable, or impossible to attain.

Towards the objective of providing timely actionable intelligence in urban environments, the emerging compressive sensing (CS) techniques have been shown to yield reduced cost and efficient sensing operations that allow super-resolution imaging of sparse behind-the-wall scenes [10, 62–76]. CS is a very effective technique for scene reconstruction from a relatively small number of data samples without compromising the imaging quality [77–89]. In general, the minimum number of data samples or sampling rate that is required for scene image formation is governed by the Nyquist theorem. However, when the scene is sparse, CS provides very efficient sampling, thereby significantly decreasing the required volume of data collected.

In this section, we focus on CS for TWRI and present l_1 norm reconstruction techniques that address the unique challenges associated with fast and efficient imaging in urban operations. Sections 2.2 to 2.5 deal with imaging of stationary scenes, whereas moving target localization is discussed in Sections 2.6 and 2.7. More specifically, Section 2.2 deals with CS based strategies for stepped-frequency based radar imaging of sparse stationary scenes with reduced data volume in spatial and frequency domains. Prior and complete removal of clutter is assumed, which renders the scene sparse. Section 2.3 presents CS solutions in the presence of front wall clutter. Wall mitigation in conjunction with application of CS is presented for the case when the same reduced frequency set is used from all of the employed antennas. Section 2.4 considers imaging of the building interior structures using a CS-based approach, which exploits prior information of building construction practices to form an appropriate sparse representation of the building interior layout. Section 2.5 presents CS based multipath exploitation technique to achieve good image reconstruction in rich multipath indoor environments from few spatial and frequency measurements. Section 2.6 deals with joint localization of stationary and moving targets using CS based approaches, provided that the indoor scene is sparse in both stationary and moving targets. Section 2.7 discusses a sparsity-based CD approach to moving target indication for TWRI applications, and deals with cases when the heavy clutter caused by strong reflections from exterior and interior walls reduces the sparsity of the scene. Concluding remarks are provided in Section 2.8. It is noted that for the sake of not overly complicating the notation, some symbols are used to indicate different variables over different sections. However, for those cases, these variables are redefined to reflect the change.

2.2   CS Strategies in Frequency and Spatial Domains For TWRI

In this section, we apply CS to through-the-wall imaging of stationary scenes, assuming prior and complete removal of the front wall clutter [62, 63]. For example, if the reference scene is known, then background subtraction can be performed for removal of wall clutter, thereby improving the sparsity of the behind-the-wall stationary scene. We assume stepped-frequency based SAR operation. We first present the through-the-wall signal model, followed by a description of the sparsity-based scene reconstruction, highlighting the key equations. It is noted that the problem formulation can be modified in a straightforward manner for pulsed operation and multistatic systems.

2.2.1   Through-the-Wall Signal Model

Consider a homogeneous wall of thickness d and dielectric constant ε located along the x-axis, and the region to be imaged located beyond the wall along the positive z-axis. Assume that an N-element line array of transceivers is located parallel to the wall at a standoff distance z_{off}, as shown in Fig. 1. Let the nth transceiver, located at $\mathbf{x}_n = (x_n, -z_{off})$, illuminate the scene with a stepped-frequency signal of M frequencies, which are equispaced over the desired bandwidth $\omega_{M-1} - \omega_0$,

$$\omega_m = \omega_0 + m\Delta\omega, \quad m = 0,1,\ldots,M-1 \tag{2.1}$$

where ω_0 is the lowest frequency in the desired frequency band and $\Delta\omega$ is the frequency step size. The reflections from any targets in the scene are measured only at the same transceiver location. Assuming the scene contains P point targets and the wall return has been completely removed, the output of the nth transceiver corresponding to the mth frequency is given by,

$$y(m,n) = \sum_{p=0}^{P-1} \sigma_p \exp(-j\omega_m \tau_{p,n}) \tag{2.2}$$

where σ_p is the complex reflectivity of the pth target, and $\tau_{p,n}$ is the two-way traveling time between the nth antenna and the target. It is noted that the complex amplitude due to free-space path loss, wall reflection/transmission coefficients and wall losses, is assumed to be absorbed into the target reflectivity. The propagation delay $\tau_{p,n}$ is given by [27–28, 40]

$$\tau_{p,n} = \frac{2l_{np,air,1}}{c} + \frac{2l_{np,wall}}{v} + \frac{2l_{np,air,2}}{c} \tag{2.3}$$

where c is the speed of light in free-space, $v = c/\sqrt{\varepsilon}$ is the speed through the wall, and the variables $l_{np,air,1}$, $l_{np,wall}$, and $l_{np,air,2}$ represent the traveling distances of the signal before, through, and beyond the wall, respectively, from the nth transceiver to the pth target.

An equivalent matrix-vector representation of the received signals in (2.2) can be obtained as follows. Assume that the region of interest is divided into a finite number of pixels $N_x \times N_z$ in crossrange and downrange, and the point targets occupy no more than P ($<< N_x \times N_z$) pixels. Let $r(k,l), k = 0,1,\ldots,N_x - 1, \ l = 0,1,\ldots,N_z - 1$, be a weighted indicator function, which takes the value σ_p if the pth point target exists at the (k, l)-th pixel; otherwise, it is zero. With the values $r(k,l)$ lexicographically ordered into a column vector $\mathbf{r}$ of length $N_x N_z$, the received signal corresponding to the nth antenna can be expressed in matrix-vector form as,

$$\mathbf{y}_n = \Psi_n \mathbf{r} \tag{2.4}$$

where Ψ_n is a matrix of dimensions $M \times N_x N_z$, and its mth row is given by,

$$[\Psi_n]_m = \begin{bmatrix} e^{-j\omega_m \tau_{00,n}} & \cdots & e^{-j\omega_m \tau_{(N_x N_z - 1),n}} \end{bmatrix} \tag{2.5}$$

Considering the measurement vector corresponding to all N antennas, defined as,

$$y = \begin{bmatrix} \mathbf{y}_0^T & \mathbf{y}_1^T & \cdots & \mathbf{y}_{N-1}^T \end{bmatrix}^T \qquad (2.6)$$

the relationship between $\mathbf{y}$ and $\mathbf{r}$ is given by

$$\mathbf{y} = \Psi \mathbf{r} \qquad (2.7)$$

where

$$\Psi = \begin{bmatrix} \Psi_0^T & \Psi_1^T & \cdots & \Psi_{N-1}^T \end{bmatrix}^T \qquad (2.8)$$

The matrix Ψ is a linear mapping between the full data $\mathbf{y}$ and the sparse vector $\mathbf{r}$.

2.2.2 Sparsity-Based Data Acquisition and Scene Reconstruction

The expression in (2.7) involves the full set of measurements made at the N array locations using the M frequencies. For a sparse scene, it is possible to recover $\mathbf{r}$ from a reduced set of measurements. Consider $\breve{\mathbf{y}}$, which is a vector of length $Q_1 Q_2$ ($<< MN$) consisting of elements chosen from $\mathbf{y}$ as follows,

$$\breve{\mathbf{y}} = \Phi \mathbf{y} = \Phi \Psi \mathbf{r} \qquad (2.9)$$

where Φ is a $Q_1 Q_2 \times MN$ matrix of the form,

$$\Phi = \mathrm{kron}\,(\vartheta, \mathbf{I}_{Q_1}) \cdot \mathrm{diag}\,\{\varphi^{(0)}, \varphi^{(1)}, \ldots, \varphi^{(N-1)}\} \qquad (2.10)$$

In (2.10), 'kron' denotes the Kronecker product, $\mathbf{I}_{Q_1}$ is a $Q_1 \times Q_2$ identity matrix, ϑ is a $Q_2 \times N$ measurement matrix constructed by randomly selecting Q_2 rows of an $N \times N$ identity matrix, and $\varphi^{(n)}$, $n = 0,1,\ldots,N-1$, is a $Q_1 \times M$ measurement matrix constructed by randomly selecting Q_1 rows of an $M \times M$ identity matrix. We note that ϑ determines the reduced antenna locations, whereas $\varphi^{(n)}$ determines the reduced set of frequencies corresponding to the nth antenna location. The number of measurements $Q_1 Q_2$ required to achieve successful CS reconstruction highly depends on the coherence between Φ and Ψ. For the problem at hand, Φ is the canonical basis and Ψ is similar to the Fourier basis, which have been shown to exhibit maximal incoherence [80]. Given $\breve{\mathbf{y}}$, we can recover $\mathbf{r}$ by solving the following equation[1],

$$\hat{\mathbf{r}} = \arg\min \|\mathbf{r}\|_{l_1} \text{ subject to } \breve{\mathbf{y}} \approx \Phi \Psi \mathbf{r} \qquad (2.11)$$

We note that the problem in (2.11) can be solved using convex relaxation, greedy pursuit, or combinatorial algorithms [91–96]. In this section, we consider Orthogonal Matching Pursuit (OMP), which is known to provide a fast and easy to implement solution. Moreover, OMP is better suited when frequency measurements are used [95]. It is noted that the number of iterations of the OMP is usually associated with the level of sparsity of the scene. In practice, this piece of information is often unavailable a priori and the stopping condition is heuristic. Underestimating the sparsity would result in the image not being completely reconstructed (underfitting), while overestimation would cause some of the noise being treated as signal (overfitting). Use of cross validation (CV) has been also proposed to determine the stopping condition for the greedy algorithms [97–99]. CV is a statistical technique that separates a data set into a training set and a cross validation set. The training set is used to detect the optimal stopping iteration. There is, however, a tradeoff between allocating the measurements for reconstruction or CV. More details can be found in [97, 98].

---

[1] Ideally, minimization of the l_0 norm would provide the sparsest solution. Unfortunately, it is NP-hard to solve the resulting minimization problem. The l_1 norm has been shown to serve as a good surrogate for l_0 norm [90]. The l_1-minimization problem is convex, which can be solved in polynomial time.

2.2.3 Illustrative Results

A through-the-wall wideband SAR system was set up in the Radar Imaging Lab at Villanova University. A 67-element line array with an inter-element spacing of 0.0187m, located along the x-axis, was synthesized parallel to a 0.14m thick solid concrete wall of length 3.05m and at a standoff distance equal to 1.24m. A stepped-frequency signal covering the 1-3 GHz frequency band with a step size of 2.75MHz was employed. Thus, at each scan position, the radar collects 728 frequency measurements. A vertical metal dihedral was used as the target and was placed at (0, 4.4)m on the other side of the front wall. The size of each face of the dihedral is 0.39m by 0.28m. The back and the side walls of the room were covered with RF absorbing material to reduce clutter. The empty scene without the dihedral target present was also measured to enable background subtraction for wall clutter removal.

The region to be imaged is chosen to be 4.9m × 5.4m centered at (0, 3.7)m and divided into 33 × 73 pixels, respectively. For CS, 20% of the frequencies and 51% of the array locations were used, which collectively represent 10.2% of the total data volume. Figs. 2(a) and 2(c) depict the images corresponding to the full dataset obtained with backprojection and l_1 norm reconstruction, respectively. Figs. 2(b) and 2(d) show the images corresponding to the measured scene obtained with backprojection and l_1 norm reconstruction, respectively, applied to the reduced background subtracted dataset. In Figure 2 and all subsequent figures in this section, we plot the image intensity with the maximum intensity value in each image normalized to 0dB. The true target position is indicated with a solid red rectangle. We observe that, with the availability of the empty scene measurements, background subtraction renders the scene sparse and thus, CS based approach generates an image using reduced data where the target can be easily identified. On the other hand, backprojection applied to reduced dataset results in performance degradation, indicated by the presence of many artifacts in the corresponding image. OMP was used to generate the CS images. For this particular example, the number of OMP iterations was set to 5.

2.3   Effects of Walls on Compressive Sensing Solutions

The application of CS for TWRI as presented in Section II assumed prior and complete removal of front wall EM returns. Without this assumption, strong wall clutter, which extends along the range dimension, reduces the sparsity of the scene and, as such, impedes the application of CS [71–73]. Having access to the background scene is not always possible in practical applications. In this section, we apply joint CS and wall mitigation techniques using reduced data measurements. In essence, we address wall clutter mitigations in the context of CS.

There are several approaches, which successfully mitigate the front wall contribution to the received signal [39, 45, 58–61]. These approaches were originally introduced to work on the full data volume and did not account for reduced data measurements especially randomly. We examine the performance of the subspace projection wall mitigation technique [60] in conjunction with sparse image reconstruction. Only a small subset of measurements is employed for both wall clutter reduction and image formation. We consider the case where the same subset of frequencies is used for each employed antenna. Wall clutter mitigation under use of different frequencies across the employed antennas is discussed in [68, 73]. It is noted that, although not reported in this section, the spatial filtering based wall mitigation scheme [45] in conjunction with CS provides a similar performance to the subspace projection scheme [73].

2.3.1 Wall Clutter Mitigation

We first extend the through-the-wall signal model of (2.2) to include the front wall return. Without the assumption of prior wall return removal, the output of the nth transceiver corresponding to the mth frequency for a scene of P point targets is given by,

$$y(m,n) = \sigma_w \exp(-j\omega_m \tau_w) + \sum_{p=0}^{P-1} \sigma_p \exp(-j\omega_m \tau_{p,n}) \tag{2.12}$$

where σ_w is the complex reflectivity of the wall, and τ_w is the two-way traveling time of the signal from the nth antenna to the wall, and is given by

$$\tau_w = \frac{2z_{off}}{c} \tag{2.13}$$

It is noted that both the target and wall reflectivities in (2.12) are assumed to be independent of frequency and aspect angle. Many of the walls and indoor targets, including humans, have dependency of their reflection coefficients on frequency, which could also be a function of angle and polarization. This dependency, if neglected, could be a source of error. The latter, however, can be tolerated for relatively limited aperture and bandwidth. Further note that we assume a simple scene of P point targets behind a front wall. The model can be extended to incorporate returns from more complex scenes involving multiple walls and room corners. These extensions are discussed in later sections.

From (2.12), we note that τ_w does not vary with the antenna location since the array is parallel to the wall. Furthermore, as the wall is homogeneous and assumed to be much larger than the beamwidth of the antenna, the first term in (2.12) assumes the same value across the array aperture. Unlike τ_w, the time delay $\tau_{p,n}$, given by (2.3), is different for each antenna location, since the signal path from the antenna to the target is different from one antenna to the other.

The signals received by the N antennas at the M frequencies are arranged into an $M \times N$ matrix, $\mathbf{Y}$,

$$\mathbf{Y} = \begin{bmatrix} \mathbf{y}_0 & \cdots & \mathbf{y}_n & \cdots & \mathbf{y}_{N-1} \end{bmatrix} \tag{2.14}$$

where $\mathbf{y}_n$ is the $M \times 1$ vector containing the stepped-frequency signal received by the nth antenna,

$$\mathbf{y}_n = \begin{bmatrix} y(0,n) & \cdots & y(m,n) & \cdots & y(M-1,n) \end{bmatrix}^T \tag{2.15}$$

with $y(m,n)$ given by (12). The eigen-structure of the imaged scene is obtained by performing the SVD of $\mathbf{Y}$,

$$\mathbf{Y} = \mathbf{U}\Lambda\mathbf{V}^H \tag{2.16}$$

where 'H' denotes the Hermitian transpose, $\mathbf{U}$ and $\mathbf{V}$ are unitary matrices containing the left and right singular vectors, respectively, and Λ is a diagonal matrix

$$\Lambda = \begin{pmatrix} \lambda_1 & \cdots & 0 \\ \vdots & \ddots & \vdots \\ 0 & \cdots & \lambda_N \\ \vdots & \ddots & \vdots \\ 0 & \cdots & 0 \end{pmatrix} \tag{2.17}$$

and $\lambda_1 \geq \lambda_2 \geq \ldots \geq \lambda_N$ are the singular values. Without loss of generality, the number of frequencies are assumed to exceed the number of antenna locations, i.e., $M > N$. The subspace projection method assumes that the wall returns and the target reflections lie in different subspaces. Therefore, the first K dominant singular vectors of the $\mathbf{Y}$ matrix are used to construct the wall subspace,

$$\mathbf{S}_{wall} = \sum_{i=1}^{K} \mathbf{u}_i \mathbf{v}_i^H \tag{2.18}$$

Methods for determining the dimensionality K of the wall subspace have been reported in [59, 60]. The subspace orthogonal to the wall subspace is,

$$\mathbf{S}_{wall}^{\perp} = \mathbf{I} - \mathbf{S}_{wall}\mathbf{S}_{wall}^H \tag{2.19}$$

where $\mathbf{I}$ is the identity matrix. To mitigate the wall returns, the data matrix $\mathbf{Y}$ is projected on the orthogonal subspace [60],

$$\tilde{\mathbf{Y}} = \mathbf{S}_{wall}^{\perp}\mathbf{Y} \tag{2.20}$$

The resulting data matrix has little or no contribution from the front wall.

2.3.2 Joint Wall Mitigation and CS

Subspace projection method for wall clutter reduction relies on the fact that the wall reflections are strong and assume very close values at the different antenna locations. When the same set of frequencies is employed for all employed antennas, the condition of spatial invariance of the wall reflections is maintained [72, 73]. This permits direct application of the subspace projection method as a preprocessing step to the l_1 norm based scene reconstruction of (2.11).

2.3.3 Illustrative Results

We consider the same experimental setup as in Section III.C. Fig. 3(a) shows the result obtained with l_1 norm reconstruction using 10.2% of the raw data volume without background subtraction. The number of OMP iterations was set to 100. Comparing Fig. 3(a) and the corresponding background subtracted image of Fig. 2(d), it is evident that in the absence of access to the background scene, the wall mitigation techniques must be applied, as a preprocessing step, prior to CS in order to detect the targets behind the wall.

First, we consider the case when the same set of reduced frequencies is used for a reduced set of antenna locations. We employ only 10.2% of the data volume, i.e., 20% of the available frequencies and 51% of the antenna locations. The subspace projection method is applied to a $\mathbf{Y}$ matrix of reduced dimension 146×34. The corresponding l_1 norm reconstructed image obtained with OMP is depicted in Fig. 3(b). It is clear that, even when both spatial and frequency observations are reduced, the joint application of wall clutter mitigation and CS techniques successfully provides front wall clutter suppression and unmasking of the target.

2.4 Designated Dictionary for Wall Detection

In this section, we address the problem of imaging building interior structures using a reduced set of measurements. We consider interior walls as targets of interest and attempt to reveal the building interior layout based on CS techniques. We note that construction practices suggest the exterior and interior walls to be parallel or perpendicular to each other. This enables sparse scene representations using a dictionary of possible wall orientations and locations [76]. Conventional CS recovery algorithms can then be applied to reduced number of observations to recover the positions of various walls, which is a primary goal in TWRI.

2.4.1 Signal Model under Multiple Parallel Walls

Considering a monostatic stepped-frequency SAR system with N antenna positions located parallel to the front wall, as shown in Fig. 1, we extend the signal model in (2.12) to include reflections from

51

multiple parallel interior walls, in addition to the returns from the front wall and the P point targets. That is, the received signal at the nth antenna location corresponding to the mth frequency can be expressed as,

$$y(m,n) = \sigma_w \exp(-j\omega_m \tau_w) + \sum_{p=0}^{P-1} \sigma_p \exp(-j\omega_m \tau_{p,n}) + \sum_{i=0}^{I_w-1} \sigma_{w_i} \exp(-j\omega_m \tau_{w_i}) \qquad (2.21)$$

where I_w is the number of interior walls parallel to the array axis, τ_{w_i} represents the two-way traveling time of the signal from the nth antenna to the ith interior wall and σ_{w_i} is the complex reflectivity of the ith interior wall. Similar to the front wall, the delays τ_{w_i} are independent of the variable n, as evident in the subscripts.

Note that the above model contains contributions only from interior walls parallel to the front wall and the antenna array. This is because, due to the specular nature of the wall reflections, a SAR system located parallel to the front wall will only be able to receive direct returns from walls which are parallel to the front wall. The detection of perpendicular walls is possible by concurrently detecting and locating the canonical scattering mechanism of corner features created by the junction of walls of a room or by having access to another side of the building. Extension of the signal model to incorporate corner returns is reported in [76].

Instead of the point-target based sensing matrix described in (2.7), where each antenna accumulates the contributions of all the pixels, we use an alternate sensing matrix, proposed in [68], to relate the scene vector, $\mathbf{r}$, and the observation vector, $\mathbf{y}$. This matrix underlines the specular reflections produced by the walls. Due to wall specular reflections, and since the array is assumed parallel to the front wall and, thus, parallel to interior walls, the rays collected at the nth antenna will be produced by portions of the walls that are only in front of this antenna (see Fig. 4(a)). The alternate matrix, therefore, only considers the contributions of the pixels that are located in front of each antenna. In so doing, the returns of the walls located parallel to the array axis are emphasized. As such, it is most suited to the specific building structure imaging problem, wherein the signal returns are mainly caused by EM reflections of exterior and interior walls. The alternate linear model can be expressed as

$$\mathbf{y} = \overline{\Psi}\mathbf{r} \qquad (2.22)$$

where

$$\overline{\Psi} = \begin{bmatrix} \overline{\Psi}_0^T & \overline{\Psi}_1^T & \dots & \overline{\Psi}_{N-1}^T \end{bmatrix} \qquad (2.23)$$

with $\overline{\Psi}_n$ defined as,

$$\left[\overline{\Psi}_n\right]_m = \begin{bmatrix} \Im_{[(0,0),n]}e^{-j\omega_m\tau_{(0,0)}} & \dots & \Im_{[(N_x-1,N_z-1),n]}e^{-j\omega_m\tau_{(N_x-1,N_z-1)}} \end{bmatrix} \qquad (2.24)$$

In (2.24), $\tau_{k,l}$ is the two-way signal propagation time associated with the downrange of the (k,l)th pixel, and the function $\Im_{[(k,l),n]}$ works as an indicator function in the following way,

$$\Im_{[(k,l),n]} = \begin{cases} 1 & \text{if the } (k,l)\text{th pixel is in front of the } n\text{th antenna} \\ 0 & \text{otherwise} \end{cases} \qquad (2.25)$$

That is, if x_k and x_n represent the crossrange coordinates of the (k, l)th pixel and the nth antenna location, respectively, and ∂x is the crossrange sampling step, then $\Im_{[(k,l),n]} = 1$ provided that $x_k - \partial x/2 \leq x_n \leq x_k + \partial x/2$ (see Fig. 4(b)).

2.4.2 Sparsifying Dictionary for Wall Detection

Since the number of parallel walls is typically much smaller compared to the downrange extent of the building, the decomposition of the image into parallel walls can be considered as sparse. Note that although other indoor targets, such as furniture and humans, may be present, their projections onto the horizontal lines are expected to be negligible compared to those of the walls.

In order to obtain a linear matrix-vector relation between the scene and the horizontal projections, we define a sparsifying matrix **R** composed of possible wall locations. Specifically, each column of the dictionary **R** represents an image containing a single wall of length l_x pixels, located at a specific crossrange and at a specific downrange in the image. Consider the crossrange to be divided into N_c non-overlapping blocks of l_x pixels each (see Fig. 5(a)), and the downrange division defined by the pixel grid. The number of blocks N_c is determined by the value of l_x, which is the minimum expected wall length in the scene. Therefore, the dimension of **R** is $N_x N_z \times N_c N_z$, where the product $N_c N_z$ denotes the number of possible wall locations. Figure 5(b) shows a simplified scheme of the sparsifying dictionary generation. The projection associated with each wall location is given by,

$$g^{(b)}(l) = \frac{1}{l_x} \sum_{k \in B[b]} r(k,l) \tag{2.26}$$

where $B[b]$ indicates the bth crossrange block and $b = 1, 2, \ldots, N_c$. Defining

$$\mathbf{g} = \left[g^{(1)}(0) \quad \cdots \quad g^{(N_c)}(0) \quad g^{(1)}(1) \quad \cdots \quad g^{(N_c)}(1) \quad \cdots \quad g^{(1)}(N_z - 1) \quad \cdots \quad g^{(N_c)}(N_z - 1) \right]$$

the linear system of equations relating the observed data **y** and the sparse vector **g** is given by,

$$\mathbf{y} = \overline{\Psi} \mathbf{R} \mathbf{g} \tag{2.28}$$

In practice and by the virtue of collecting signal reflections corresponding to the zero aspect angle, any interior wall outside the synthetic array extent will not be visible to the system. Finally, the CS image in this case is obtained by first recovering the projection vector **g** using l_1 norm minimization with a reduced set of measurements and then forming the product **Rg**.

It is noted that we are implicitly assuming that the extents of the walls in the scene are integer multiples of the block of l_x pixels. In case this condition is not satisfied, the maximum error in determining the wall extent will be at most equal to the chosen block size. Note that incorporation of the corner effects will help resolve this issue, since the localization of corners will identify the wall extent [76].

2.4.3 Illustrative Results

A through-the-wall SAR system was set up in the Radar Imaging Lab, Villanova University. A stepped-frequency signal consisting of 335 frequencies covering the 1 to 2 GHz frequency band was used for interrogating the scene. A monostatic synthetic aperture array, consisting of 71-element locations with an inter-element spacing of 2.2cm, was employed. The scene consisted of two parallel plywood walls, each 2.25cm thick, 1.83m wide, and 2.43m high. Both walls were centered at 0m in crossrange. The first and the second walls were located at respective distances of 3.25m and 5.1m from the antenna baseline. Figure 6(a) depicts the geometry of the experimental scene.

The region to be imaged is chosen to be 5.65m (crossrange) × 4.45m (downrange), centered at (0, 4.23)m, and is divided into 128 × 128 pixels. For the CS approach, we use a uniform subset of only 84 frequencies at each of the 18 uniformly spaced antenna locations, which represent 6.4% of the full

data volume. The CS reconstructed image is shown in Fig. 6(b). We note that the proposed algorithm was able to reconstruct both walls. However, it can be observed in Fig. 6(b) that ghost walls appear immediately behind each true wall position. These ghosts are attributed to the dihedral-type reflections from the wall-floor junctions.

2.5 CS and Multipath Exploitation

In this section, we consider the problem of multipath in view of the requirements of fast data acquisition and reduced measurements. Multipath ghosts may cast a sparse scene as a populated scene, and at minimum will render the scene less sparse, degrading the performance of CS based reconstruction. A CS method that directly incorporates multipath exploitation into sparse signal reconstruction for imaging of stationary scenes with a stepped-frequency monostatic SAR is presented. Assuming prior knowledge of the building layout, the propagation delays corresponding to different multipath returns for each assumed target position are calculated, and the multipath returns associated with reflections from the same wall are grouped together and represented by one measurement matrix. This allows CS solutions to focus the returns on the true target positions without ghosting. Although not considered in this section, it is noted that the clutter due to front wall reverberations can be mitigated by adapting a similar multipath formulation, which maps back multiple reflections within the wall after separating wall and target returns [100].

2.5.1 Multipath Propagation Model

We refer to the signal that propagates from the antenna through the front wall to the target and back to the antenna as the direct target return. Multipath propagation corresponds to indirect paths, which involve reflections at one or more interior walls by which the signal may reach the target. Multipath can also occur due to reflections from the floor and ceiling and interactions among different targets. In considering wall reflections and assuming diffuse target scattering, there are two typical cases for multipath. In the first case, the wave traverses a path that consists of two parts; one part is the propagation path to the target and back to the receiver, and the other part is a round trip path from the target to an interior wall. As the signal weakens at each secondary wall reflection, this case can usually be neglected. Furthermore, except when the target is close to an interior wall, the corresponding propagation delay is high, and, most likely, would be equivalent to the direct-path delay of a target that lies outside the perimeter of the room being imaged. Thus, if necessary, this type of multipath can be gated out. The second case is a bistatic scattering scenario, where the signal propagation on transmit and receive takes place along different paths. This is the dominant case of multipath with one of the paths being the direct propagation, to or from the target, and the other involving a secondary reflection at an interior wall.

Other higher-order multipath returns are possible as well. Signals reaching the target can undergo multiple reflections within the front wall. We refer to such signals as wall ringing multipath. Also, the reflection at the interior wall can occur at the outer wall-air interface. This will result, however, in additional attenuation and, therefore, can be neglected. In order to derive the multipath signal model, we assume perfect knowledge of the front wall, i.e. location, thickness, and dielectric constant, as well as the location of the interior walls.

2.5.1.1 Interior Wall Multipath

Consider the antenna-target geometry illustrated in Fig. 7(a), where the front wall has been ignored for simplicity. The pth target is located at $\mathbf{x}_p = (x_p, z_p)$, and the interior wall is parallel to the z-axis and located at $x = x_w$. Multipath propagation consists of the forward propagation from the nth antenna to the target along the path $\mathcal{P}''$ and the return from the target via a reflection at the

interior wall along the path $\mathcal{P}'$. Assuming specular reflection at the wall interface, we observe from Fig. 7(a) that reflecting the return path about the interior wall yields an alternative antenna-target geometry. We obtain a virtual target located at $\mathbf{x}'_p = (2x_w - x_p, z_p)$, and the delay associated with path $\mathcal{P}'$ is the same as that of the path $\widetilde{\mathcal{P}}'$ from the virtual target to the antenna. This correspondence simplifies the calculation of the one-way propagation delay $\tau_{p,n}^{(\mathcal{P}')}$ associated with path $\mathcal{P}'$. It is noted that this principle can be used for multipath via any interior wall.

From the position of the virtual target of an assumed target location, we can calculate the propagation delay along path $\mathcal{P}'$ as follows. Under the assumption of free space propagation, the delay can be simply calculated as the Euclidean distance from the virtual target to the receiver divided by the propagation speed of the wave. In the TWRI scenario, however, the wave has to pass through the front wall on its way from the virtual target to the receiver. As the front wall parameters are assumed to be known, the delay can be readily calculated from geometric considerations using Snell's law [28].

2.5.1.2 Wall Ringing Multipath

The effect of wall ringing on the target image can be delineated through Fig. 7(b), which depicts the wall and the incident, reflected, and refracted waves. The distance between the target and the array element in crossrange direction, Δx, can be expressed as

$$\Delta x = (\Delta z - d)\tan\theta_{air} + d(1 + 2i_w)\tan\theta_{wall} \tag{2.29}$$

where Δz is the distance between target and array element in downrange direction, and θ_{air} and θ_{wall} are the angles in the air and in the wall medium, respectively. The integer i_w denotes the number of internal reflections within the wall. The case $i_w = 0$ describes the direct path as derived in [28]. From Snell's law,

$$\frac{\sin\theta_{air}}{\sin\theta_{wall}} = \sqrt{\varepsilon} \tag{2.30}$$

Equations (2.29) and (2.30) form a nonlinear system of equations that can be solved numerically for the unknown angles, e.g., using the Newton method. Having the solution for the incidence and refraction angles, we can express the one-way propagation delay associated with the wall ringing multipath as [101]

$$\tau = \frac{(\Delta z - d)}{c\cos\theta_{air}} + \frac{\sqrt{\varepsilon}d(1 + 2i_w)}{c\cos\theta_{wall}}. \tag{2.31}$$

2.5.2 Received Signal Model

Having described the two principal multipath mechanisms in TWRI, namely the interior wall and wall ringing types of multipath, we are now in a position to develop a multipath model for the received signal. We assume that the front wall returns have been suppressed and the measured data contains only the target returns. The case with the wall returns present in the measurements is discussed in [100].

Each path $\mathcal{P}$ from the transmitter to a target and back to receiver can be divided into two parts, $\mathcal{P}'$ and $\mathcal{P}''$, where $\mathcal{P}''$ denotes the partial path from the transmitter to the scattering target and $\mathcal{P}'$ is the return path back to the receiver. For each target-transceiver combination, there exist a number of partial paths due to the interior wall and wall ringing multipath phenomena. Let $\mathcal{P}'_{i_1}, i_1 = 0,1,\ldots,R_1 - 1,$ and $\mathcal{P}''_{i_2}, i_2 = 0,1,\ldots,R_2 - 1,$ denote the feasible partial paths. Any

55

combination of $\mathcal{P}'_{i_1}$ and $\mathcal{P}''_{i_2}$ results in a round-trip path $\mathcal{P}_i, i = 0,1,\ldots,R-1$. We can establish a function that maps the index i of the round-trip path to a pair of indices of the partial paths, $i \mapsto (i_1, i_2)$. Hence, we can determine the maximum number $R \leq R_1 R_2$ of possible paths for each target-transceiver pair. Note that, in practice, $R \ll R_1 R_2$, as some round-trip paths may be equal due to symmetry while some others could be strongly attenuated, and, thereby can be neglected. We follow the convention that $\mathcal{P}_0$ refers to the direct round-trip path.

The round-trip delay of the signal along path $\mathcal{P}_i$, consisting of the partial parts $\mathcal{P}'_{i_1}$ and $\mathcal{P}''_{i_2}$, can be calculated as

$$\tau^{(i)}_{p,n} = \tau^{(i_1)}_{p,n} + \tau^{(i_2)}_{p,n} \tag{2.32}$$

We also associate a complex amplitude $w^{(i)}_p$ for each possible path corresponding to the pth target, with the direct path, which is typically the strongest in TWRI, having $w^{(0)}_p = 1$.

Without loss of generality, we assume the same number of propagation paths for each target. The unavailability of a path for a particular target is reflected by a corresponding path amplitude of zero. The received signal at the nth antenna due to the mth frequency can, therefore, be expressed as

$$y(m,n) = \sum_{i=0}^{R-1} \sum_{p=0}^{P-1} w^{(i)}_p \sigma^{(i)}_p \exp(-j\omega_m \tau^{(i)}_{p,n}) \tag{2.33}$$

As the bistatic radar cross section (RCS) of a target could be different from its monostatic RCS, the target reflectivity is considered to be dependent on the propagation path. For convenience, the path amplitude $w^{(i)}_p$ (33) can be absorbed into the target reflectivity $\sigma^{(i)}_p$, leading to

$$y(m,n) = \sum_{i=0}^{R-1} \sum_{p=0}^{P-1} \sigma^{(i)}_p \exp(-j\omega_m \tau^{(i)}_{p,n}) \tag{2.34}$$

Note that (2.34) is a generalization of the non-multipath propagation model (2.2). If the number of propagation paths is set to 1, then the two models are equivalent.

The matrix-vector form for the received signal under multipath propagation is given by

$$\mathbf{y} = \Psi^{(0)}\mathbf{r}^{(0)} + \Psi^{(1)}\mathbf{r}^{(1)} + \ldots + \Psi^{(R-1)}\mathbf{r}^{(R-1)} \tag{2.35}$$

where

$$\mathbf{r}^{(i)} = \left[r^{(i)}_{00} \quad \cdots \quad r^{(i)}_{N_x N_z - 1} \right]^T$$
$$[\Psi^{(i)}]_{sq} = \exp(-j\omega_m \tau^{(i)}_{q,n}), \quad m = s \bmod M, n = \lfloor s/M \rfloor \tag{2.36}$$
$$s = 0,1,\ldots,MN-1, q = 0,1,\ldots,N_x N_z - 1$$

The term $r^{(i)}_q, q = 0,1,\ldots,N_x N_z - 1$, takes the value $\sigma^{(i)}_p$ if the pth point target exists at the qth pixel; otherwise, it is zero. Finally, the reduced measurement vector $\breve{\mathbf{y}}$ can be obtained from (2.35) as $\breve{\mathbf{y}} = \Phi\mathbf{y}$, where the $Q_1 Q_2 \times MN$ matrix Φ is defined in (2.10).

2.5.3 Sparse Scene Reconstruction with Multipath Exploitation

Within the CS framework, we aim at undoing the ghosts, i.e., inverting the multipath measurement model and achieving a reconstruction, wherein only the true targets remain.

In practice, any prior knowledge about the exact relationship between the various sub-images $\mathbf{r}^{(i)}$ of the sparse scene is either limited or nonexistent. However, we know with certainty that the sub-images $\mathbf{r}^{(0)}, \mathbf{r}^{(1)},\ldots,\mathbf{r}^{(R-1)}$ describe the same underlying scene. That is, the support of the R images

is the same, or at least approximately the same. The common structure property of the sparse scene suggests the application of a group sparse reconstruction.

All unknown vectors in (2.35) can be stacked to form a tall vector of length $N_x N_z R$

$$\vec{\mathbf{r}} = \begin{bmatrix} \mathbf{r}^{(0)^T} & \mathbf{r}^{(1)^T} & \cdots & \mathbf{r}^{(R-1)^T} \end{bmatrix}^T \tag{2.37}$$

The reduced measurement vector $\breve{\mathbf{y}}$ can then be expressed as

$$\breve{\mathbf{y}} = \mathbf{B}\vec{\mathbf{r}} \tag{2.38}$$

where $\mathbf{B} = \begin{bmatrix} \Phi\Psi^{(0)} & \Phi\Psi^{(1)} & \cdots & \Phi\Psi^{(R-1)} \end{bmatrix}$ has dimensions $Q_1 Q_2 \times N_x N_z R$.

We proceed to reconstruct the images $\vec{\mathbf{r}}$ from $\breve{\mathbf{y}}$ under measurement model (2.38). It has been shown that a group sparse reconstruction can be obtained by a mixed $l_1 - l_2$ norm regularization [102–105]. Thus, we solve

$$\hat{\vec{\mathbf{r}}} = \arg\min_{\vec{\mathbf{r}}} \frac{1}{2} \|\breve{\mathbf{y}} - \mathbf{B}\vec{\mathbf{r}}\|_2^2 + \alpha \|\vec{\mathbf{r}}\|_{2,1} \tag{2.39}$$

where α is the so-called regularization parameter and

$$\|\vec{\mathbf{r}}\|_{2,1} := \sum_{q=0}^{N_x N_z - 1} \left\| \left[r_q^{(0)}, r_q^{(1)}, \ldots, r_q^{(R-1)} \right]^T \right\|_2 = \sum_{q=0}^{N_x N_z - 1} \sqrt{\sum_{i=0}^{R-1} r_q^{(i)} r_q^{(i)*}} \tag{2.40}$$

is the mixed $l_1 - l_2$ norm. As defined in Eq. (40), the mixed $l_1 - l_2$ norm behaves like an l_1 norm on the vector $\left\| [r_q^{(0)}, r_q^{(1)}, \cdots, r_q^{(R-1)}]^T \right\|_2$, $q = 0,1,\cdots, N_x N_z - 1$, and therefore, induces group sparsity. In other words, each $\left\| [r_q^{(0)}, r_q^{(1)}, \cdots, r_q^{(R-1)}]^T \right\|_2$, and equivalently each $[r_q^{(0)}, r_q^{(1)}, \cdots, r_q^{(R-1)}]^T$, is encouraged to be set to zero. On the other hand, within the groups, the l_2 norm does not promote sparsity [106]. The convex optimization problem (2.39) can be solved using SparSA [102], YALL group [103], or other available schemes [105, 107].

Once a solution $\hat{\vec{\mathbf{r}}}$ is obtained, the sub-images can be noncoherently combined to form an overall image with improved signal-to-noise-and-clutter ratio (SCNR), with the elements of the composite image $\hat{\mathbf{r}}_{GS}$ defined as

$$[\hat{\mathbf{r}}_{GS}]_q = \left\| \left[r_q^{(0)}, r_q^{(1)}, \ldots, r_q^{(R-1)} \right]^T \right\|_2, \quad q = 0, \ldots, N_x N_z - 1. \tag{2.41}$$

2.5.4 Illustrative Results

An experiment was conducted in a semi-controlled environment at the Radar Imaging Lab, Villanova University. A single aluminum pipe (61 cm long, 7.6 cm diameter) was placed upright on a 1.2 m high foam pedestal at 3.67 m downrange and 0.31 m crossrange, as shown in Fig. 8. A 77-element uniform linear monostatic array with an inter-element spacing of 1.9 cm was used for imaging. The origin of the coordinate system is chosen to be at the center of the array. The 0.2 m thick concrete front wall was located parallel to the array at 2.44 m downrange. The left sidewall was at a crossrange of -1.83 m, whereas the back wall was at 6.37 m downrange (See Fig. 8). Also, there was a protruding corner on the right at 3.4 m crossrange and 4.57 m downrange. A stepped-frequency signal, consisting of 801 equally spaced frequency steps covering the 1 to 3 GHz band was employed. The left and right side walls were covered with RF absorbing material, but the protruding right corner and the back wall were left uncovered.

We consider background subtracted data to focus only on target multipath. Figure 9(a) depicts the backprojection image using all available data. Apparently, only the multipath ghosts due to the back wall, and the protruding corner in the back right are visible. Hence, we only consider these two multipath propagation cases for the group sparse CS scheme. We use 25% of the array elements and 50% of the frequencies. The corresponding CS reconstruction is shown in Fig. 9(b). The multipath ghosts have been clearly suppressed.

2.6 CS-Based Change Detection for Moving Target Localization

In this section, we consider sparsity-driven CD for human motion indication in TWRI applications. CD can be used in lieu of Doppler processing, wherein motion detection is accomplished by subtraction of data frames acquired over successive probing of the scene. In so doing, CD mitigates the heavy clutter that is caused by strong reflections from exterior and interior walls and also removes stationary objects present in the enclosed structure, thereby rendering a densely populated scene sparse [7, 9–10]. As a result, it becomes possible to exploit CS techniques for achieving reduction in the data volume. We assume a multistatic imaging system with physical transmit and receive apertures and a wideband transmit pulse. We establish an appropriate CD model for translational motion that permits formulation of linear modeling with sensing matrices, so as to apply CS for scene reconstruction. Other types of human motions involving sudden short movements of the limbs, head, and/or torso are discussed in [70].

2.6.1 Signal Model

Consider wideband radar operation with M transmitters and N receivers. A sequential multiplexing of the transmitters with simultaneous reception at multiple receivers is assumed. As such, a signal model can be developed based on single active transmitters. We note that the timing interval for each data frame is assumed to be a fraction of a second so that the moving target appears stationary during each data collection interval.

Let $s_T(t)$ be the wideband baseband signal used for interrogating the scene. For the case of a single point target with reflectivity σ_p, located at $\mathbf{x}_p = (x_p, z_p)$ behind a wall, the pulse emitted by the mth transmitter with phase center at $\mathbf{x}_{tm} = (x_{tm}, -z_{off})$ is received at the nth receiver with phase center at $\mathbf{x}_{rn} = (x_{rn}, -z_{off})$ in the form

$$y_{mn}(t) = a_{mn}(t) + b_{mn}(t), \quad a_{mn}(t) = \sigma_p s_T(t - \tau_{p,mn})\exp(-j\omega_c \tau_{p,mn}) \qquad (2.42)$$

where ω_c is the carrier frequency, $\tau_{p,mn}$ is the propagation delay for the signal to travel between the mth transmitter, the target at $\mathbf{x}_p$, and the nth receiver, and $b_{mn}(t)$ represents the contribution of the stationary background at the nth receiver with the mth transmitter active. The delay $\tau_{p,mn}$ consists of the components corresponding to traveling distances before, through, and after the wall, similar to (3).

In its simplest form, CD is achieved by coherent subtraction of the data corresponding to two data frames, which may be consecutive or separated by one or more data frames. This subtraction operation is performed for each range bin. CD results in the set of difference signals,

$$\delta y_{mn}(t) = y_{mn}^{(L+1)}(t) - y_{mn}^{(1)}(t) = a_{mn}^{(L+1)}(t) - a_{mn}^{(1)}(t) \tag{2.43}$$

where L denotes the number of frames between the two time acquisitions. The component of the radar return from the stationary background is the same over the two time intervals, and is thus removed from the difference signal. Using (42) and (43), the (m, n)-th difference signal can be expressed as,

$$\delta y_{mn}(t) = \sigma_p s_T(t - \tau_{p,mn}^{(L+1)})\exp(-j\omega_c\tau_{p,mn}^{(L+1)}) - \sigma_p s_T(t - \tau_{p,mn}^{(1)})\exp(-j\omega_c\tau_{p,mn}^{(1)}) \tag{2.44}$$

where $\tau_{p,mn}^{(1)}$ and $\tau_{p,mn}^{(L+1)}$ are the respective two-way propagation delays for the signal to travel between the mth transmitter, the target, and the nth receiver, during the first and the second data acquisitions, respectively.

2.6.2 Sparsity-Driven Change Detection under Translational Motion

Consider the difference signal in (2.44) for the case where the target is undergoing translational motion. Two nonconsecutive data frames with relatively long time difference are used, i.e. $L \gg 1$ [108]. In this case, the target will change its range gate position during the time elapsed between the two data acquisitions. As seen from (2.44), the moving target will present itself as two targets, one corresponding to the target position during the first time interval and the other corresponding to the target location during the second data frame. It is noted that the imaged target at the reference position corresponding to the first data frame cannot be suppressed for the coherent CD approach. On the other hand, the noncoherent CD approach that deals with differences of image magnitudes corresponding to the two data frames, allows suppression of the reference image through a zero thresholding operation [23]. However, as the noncoherent approach requires the scene reconstruction to be performed prior to CD, it is not a feasible option for sparsity-based imaging, which relies on coherent CD to render the scene sparse. Therefore, we rewrite (2.44) as,

$$\delta y_{mn}(t) = \sum_{i=1}^{2} \tilde{\sigma}_i s_T(t - \tau_{i,mn})\exp(-j\omega_c\tau_{i,mn}) \tag{2.45}$$

with

$$\tilde{\sigma}_i = \begin{cases} \sigma_p & i=1 \\ -\sigma_p & i=2 \end{cases} \quad \text{and} \quad \tau_{i,mn} = \begin{cases} \tau_{p,mn}^{(L+1)} & i=1 \\ \tau_{p,mn}^{(1)} & i=2 \end{cases} \tag{2.46}$$

If we sample the difference signal $\delta y_{mn}(t)$ at times $\{t_k\}_{k=0}^{K-1}$ to obtain the $K \times 1$ vector Δy_{mn} and form the concatenated $N_x N_z \times 1$ scene reflectivity vector $\mathbf{r}$, then using the developed signal model in (2.45), we obtain the linear system of equations,

$$\Delta y_{mn} = \Psi_{mn} \mathbf{r} \tag{2.47}$$

The qth column of Ψ_{mn} consists of the received signal corresponding to a target at pixel $\mathbf{x}_q$ and the kth element of the qth column can be written as [70, 83]

$$[\Psi_{mn}]_{k,q} = \frac{s_T(t_k - \tau_{q,mn})\exp(-j\omega_c\tau_{q,mn})}{\left\| s_{q,mn} \right\|_2}, \quad k = 0,1,\ldots,K\text{-}1, \ q = 0,1,\ldots,N_x N_z - 1 \tag{2.48}$$

where $\tau_{q,mn}$ is the two-way signal traveling time from the mth transmitter to the qth pixel and back to the nth receiver. Note that the kth element of the vector $s_{q,mn}$ is $s_T(t_k - \tau_{q,mn})$, which implies that the denominator in the R.H.S. of (2.48) is the energy in the time signal. Therefore, each column of Ψ_{mn} has unit norm. Further note that if there is a target at the qth pixel, the value of the qth element of $\mathbf{r}$ should be $\tilde{\sigma}_q$; otherwise, it is zero.

The CD model described in (2.47-2.48) permits the scene reconstruction within the CS framework. We measure a J ($<< K$) dimensional vector of elements randomly chosen from $\Delta \mathbf{y}_{mn}$. The new measurements can be expressed as

$$\Delta \breve{\mathbf{y}}_{mn} = \varphi_{mn} \Delta \mathbf{y}_{mn} = \varphi_{mn} \Psi_{mn} \mathbf{r} \tag{2.49}$$

where φ_{mn} is a $J \times K$ measurement matrix. Several types of measurement matrices have been reported in the literature [[83], [86], [109] and the references therein]. To name a few, a measurement matrix whose elements are drawn from a Gaussian distribution, a measurement matrix having random ± 1 entries with probability of 0.5, or a random matrix whose entries can be constructed by randomly selecting rows of a $K \times K$ identity matrix. It was shown in [83] that the measurement matrix with random ± 1 elements requires the least amount of compressive measurements for the same radar imaging performance, and permits a relatively straight forward data acquisition implementation. Therefore, we choose to use such a measurement matrix in image reconstructions.

Given $\Delta \breve{\mathbf{y}}_{mn}$ for $m = 0,1,\ldots,M-1$, $n = 0,1,\ldots,N-1$, we can recover $\mathbf{r}$ by solving the following equation,

$$\hat{\mathbf{r}} = \arg\min_{\mathbf{r}} \|\mathbf{r}\|_{l_1} \text{ subject to } \Phi \Psi \mathbf{r} \approx \Delta \breve{\mathbf{y}} \tag{2.50}$$

where

$$\Psi = [\Psi_{00}^T \ \Psi_{01}^T \ \ldots \ \Psi_{(M-1)(N-1)}^T]^T, \quad \Phi = diag(\varphi_{00}, \varphi_{01}, \ldots, \varphi_{(M-1)(N-1)})$$

$$\Delta \breve{\mathbf{y}} = [\Delta \breve{\mathbf{y}}_{00}^T \ \Delta \breve{\mathbf{y}}_{01}^T \ \ldots \ \Delta \breve{\mathbf{y}}_{(M-1)(N-1)}^T]^T \tag{2.51}$$

Equations (2.50, 2.51) represent one strategy that can be adopted for sparsity-based CD approach, wherein a reduced number of time samples are chosen randomly for all the transmitter-receiver pairs constituting the array apertures. The above two equations can also be extended so that the reduction in data measurements includes both spatial and time samples. The latter strategy is not considered in this section.

2.6.3   Illustrative Results

A through-the-wall wideband pulsed radar system was used for data collection in the Radar Imaging Lab at Villanova University. The system uses a 0.7ns Gaussian pulse for scene interrogation. The pulse is up-converted to 3 GHz for transmission and down-converted to baseband through in-phase and quadrature demodulation on reception. The system operational bandwidth from 1.5 – 4.5 GHz provides a range resolution of 5cm. The peak transmit power is 25dBm. Transmission is through a single horn antenna, which is mounted on a tripod. An 8-element line array with an inter-element spacing of 0.06m, is used as the receiver and is placed to the right of the transmit antenna. The center-to-center separation between the transmitter and the leftmost receive antenna is 0.28m, as shown in Fig. 10. A 3.65m × 2.6m wall segment was constructed utilizing 1cm thick cement board on a 2-by-4 wood stud frame. The transmit antenna and the receive array were at a standoff distance of 1.19m from the wall. The system refresh rate is 100Hz.

In the experiment, a person walked away from the wall in an empty room (the back and the side walls were covered with RF absorbing material) along a straight line path. The path is located 0.5m to the right of the center of the scene, as shown in Fig. 10. The data collection started with the

target at position 1 and ended after the target reached position 3, with the target pausing at each position along the trajectory for a second. Consider the data frames corresponding to the target at position 2 and position 3. Each frame consists of 20 pulses, which are coherently integrated to improve the signal-to-noise ratio. The imaging region (target space) is chosen to be 3m × 3m, centered at (0.5m, 4m), and divided into 61 × 61 grid points in crossrange and downrange, resulting in 3721 unknowns. The space-time response of the target space consists of 8 × 1536 space-time measurements. For sparsity-based CD, only 5% of the 1536 time samples are randomly selected at each of the 8 receive antenna locations, resulting in 8 × 77 space-time measured data. Figure 11 depicts the corresponding result. We observe that, as the human changed its range gate position during the time elapsed between the two acquisitions, it presents itself as two targets in the image, and is correctly localized at both of its positions.

2.7   CS General Formulation for Stationary and Moving Targets

As seen in the previous sections, the presence of the front wall renders the target detection problem very difficult and challenging, and has an adverse effect on the scene reconstruction performance when employing CS. Different strategies have been devised for suppression of the wall clutter to enable target detection behind walls.   Change detection enables detection and localization of moving targets. Clutter cancellation filtering provides another option [87, 110]. However, along with the wall clutter, both of these methods also suppress the returns from the stationary targets of interest in the scene, and as such, allow subsequent application of CS to recover only the moving targets.   Wall clutter mitigation methods can be applied to remove the wall and enable joint detection of stationary and moving targets. However, these methods assume monostatic operation with the array located parallel to the front wall, and exploit the strength and invariance of the wall return across the array under such a deployment for mitigating the wall return. As such, they may not perform as well under other situations.

For multistatic imaging radar systems using ultra-wideband (UWB) pulses, an alternate option is to employ time gating, in lieu of the aforementioned clutter cancellation methods. The compact temporal support of the signal renders time gating a viable option for suppressing the wall returns. This enhances the SCR and maintains the sparsity of the scene, thereby permitting the application of CS techniques for simultaneous localization of stationary and moving targets with few observations [74].

2.7.1   Signal Model

Consider the scene layout depicted in Fig. 12. Note that although the M-element transmit and N-element receive arrays are assumed to be parallel to the front wall for notational simplicity, this is not a requirement. Let T_r be the pulse repetition interval. Consider a coherent processing interval of I pulses per transmitter and a single point target moving slowly away from the origin with constant horizontal and vertical velocity components (v_{xp}, v_{zp}), as depicted in Fig. 12.   Let the target position be $\mathbf{x}_p = (x_p, z_p)$ at time $t = 0$. Assume that the timing interval for sequencing through the transmitters is short enough so that the target appears stationary during each data collection interval of length IT_r. This implies that the target position corresponding to the ith pulse is given by

$$\mathbf{x}_p(i) = (x_p + v_{xp}iIT_r, z_p + v_{zp}iIT_r) \tag{2.52}$$

The baseband target return measured by the nth receiver corresponding to the ith pulse emitted by the mth transmitter is given by [74]

$$y_{mni}^p(t) = \sigma_p s_T(t - iIT_r - mT_r - \tau_{p,mn}(i)) \exp(-j\omega_c \tau_{p,mn}(i)) \tag{2.53}$$

where $\tau_{p,mn}(i)$ is the propagation delay for the ith pulse to travel from the mth transmitter to the target at $\mathbf{x}_p(i)$, and back to the nth receiver. In the presence of P point targets, the received signal component corresponding to the targets will be a superposition of the individual target returns in (2.53) with $p = 0,1,\ldots,P-1$. Interactions between the targets and multipath returns are ignored in this model. Note that any stationary targets behind the wall are included in this model and would correspond to the motion parameter pair $(v_{xp}, v_{zp}) = (0,0)$. Further note that the slowly moving targets are assumed to remain within the same range cell over the coherent processing interval.

On the other hand, as the wall is a specular reflector, the baseband wall return received at the nth receiver corresponding to the ith pulse emitted by the mth transmitter can be expressed as

$$y_{mni}^{wall}(t) = \sigma_w s_T(t - iIT_r - mT_r - \tau_{w,mn}))\exp(-j\omega_c \tau_{w,mn}) + B_{mni}^{wall}(t) \tag{2.54}$$

where $\tau_{w,mn}$ is the propagation delay from the mth transmitter to the wall and back to the nth receiver, and $B_{mni}^{wall}(t)$ represents the wall reverberations of decaying amplitudes resulting from multiple reflections within the wall (see Fig. 13). The propagation delay $\tau_{w,mn}$ is given by [111]

$$\tau_{w,mn} = \frac{\sqrt{(x_{tm} - x_{w,mn})^2 + z_{off}^2} + \sqrt{(x_{rn} - x_{w,mn})^2 + z_{off}^2}}{c} \tag{2.55}$$

where

$$x_{w,mn} = \frac{x_{tm} + x_{rn}}{2}. \tag{2.56}$$

is the point of reflection on the wall corresponding to the mth transmitter and the nth receiver, as shown in Fig. 13. Note that, as the wall is stationary, the delay $\tau_{w,mn}$ does not vary from one pulse to the next. Therefore, the expression in (2.54) assumes the same value for $i = 0,1,\ldots,I-1$.

Combining (2.53) and (2.54), the total baseband signal received by the nth receiver, corresponding to the ith pulse with the mth transmitter active, is given by

$$y_{mni}'(t) = y_{mni}^{wall}(t) + \sum_{p=0}^{P-1} y_{mni}^p(t) \tag{2.57}$$

By gating out the wall return in the time domain, we gain access to the sparse behind-the-wall scene of a few stationary and moving targets of interest. Therefore, the time-gated received signal contains only contributions from the P targets behind the wall as well as any residuals of the wall not removed or fully mitigated by gating. In this section, we assume that wall clutter is effectively suppressed by gating. Therefore, using (2.57), we obtain

$$y_{mni}(t) = \sum_{p=0}^{P-1} y_{mni}^p(t) \tag{2.58}$$

2.7.2   Linear Model Formulation and CS reconstruction

With the observed scene divided into $N_x \times N_z$ pixels in crossrange and downrange, consider N_{v_x} and N_{v_z} discrete values of the expected horizontal and vertical velocities, respectively. Therefore, an image with $N_x \times N_z$ pixels in crossrange and downrange is associated with each considered horizontal and vertical velocity pair, resulting in a four-dimensional target space. Note that the considered velocities contain the (0, 0) velocity pair to include stationary targets.

Sampling the received signal $y_{mni}(t)$ at times $\{t_k\}_{k=0}^{K-1}$, we obtain a $K \times 1$ vector $\mathbf{y}_{mni}$. For the lth velocity pair (v_{xl}, v_{zl}), we vectorize the corresponding crossrange vs. downrange image into an $N_x N_z \times 1$ scene reflectivity vector $\mathbf{r}(v_{xl}, v_{zl})$. The vector $\mathbf{r}(v_{xl}, v_{zl})$ is a weighted indicator vector defining the scene reflectivity corresponding to the lth considered velocity pair, i.e., if there is a target at the spatial grid point (x, z) with motion parameters (v_{xl}, v_{zl}), then the value of the corresponding element of $\mathbf{r}(v_{xl}, v_{zl})$ should be nonzero; otherwise, it is zero.

Using the developed signal model in (2.53) and (2.58), we obtain the linear system of equations,

$$\mathbf{y}_{mni} = \Psi_{mni}(v_{xl}, v_{zl})\mathbf{r}(v_{xl}, v_{zl}), \quad l = 0,1,\dots,N_{v_x}N_{v_z}-1 \tag{2.59}$$

where the matrix $\Psi_{mni}(v_{xl}, v_{zl})$ is of dimension $K \times N_x N_z$. The qth column of $\Psi_{mni}(v_{xl}, v_{zl})$ consists of the received signal corresponding to a target at pixel $\mathbf{x}_q$ with motion parameters (v_{xl}, v_{zl}), and the ith element of the qth column can be written as

$$[\Psi_{mni}(v_{xl}, v_{zl})]_{k,q} = s_T(t_k - ilT_r - mT_r - \tau_{q,mn}(i))\exp(-j\omega_c\tau_{q,mn}(i)), \quad q = 0,1,\dots,N_x N_z - 1$$
(2.60)

where $\tau_{q,mn}(i)$ is the two-way signal traveling time, corresponding to (v_{xl}, v_{zl}), from the mth transmitter to the qth spatial grid point and back to the nth receiver for the ith pulse.

Stacking the received signal samples corresponding to I pulses from all MN transmitting and receiving element pairs, we obtain the $MNIK \times 1$ measurement vector $\mathbf{y}$ as

$$\mathbf{y} = \Psi(v_{xl}, v_{zl})\mathbf{r}(v_{xl}, v_{zl}), \quad l = 0,1,\dots,(N_{v_x}N_{v_z}-1) \tag{2.61}$$

where

$$\Psi(v_{xl}, v_{zl}) = [\Psi_{000}^T(v_{xl}, v_{zl}), \dots, \Psi_{(M-1)(N-1)(I-1)}^T(v_{xl}, v_{zl})]^T. \tag{2.62}$$

Finally, forming the $MNIK \times N_x N_z N_{v_x} N_{v_z}$ matrix Ψ as

$$\Psi = [\Psi(v_{x0}, v_{z0}), \dots, \Psi(v_{x(N_{v_x}N_{v_z}-1)}, v_{z(N_{v_x}N_{v_z}-1)})]., \tag{2.63}$$

we obtain the linear matrix equation

$$\mathbf{y} = \Psi\hat{\mathbf{r}} \tag{2.64}$$

with $\hat{\mathbf{r}}$ being the concatenation of target reflectivity vectors corresponding to every possible considered velocity combination.

The model described in (64) permits the scene reconstruction within the CS framework. We measure a $J < MNIK$ dimensional vector of elements randomly chosen from $\mathbf{y}$. The reduced set of measurements can be expressed as

$$\breve{\mathbf{y}} = \Phi\Psi\hat{\mathbf{r}} \tag{2.65}$$

where Φ is a $J \times MNIK$ measurement matrix. For measurement reduction simultaneously along the spatial, slow time, and fast time dimensions, the specific structure of the matrix Φ is given by

$$\Phi = \text{kron}(\Phi_1, \mathbf{I}_{J_1 J_2 N_1}) \cdot \text{kron}(\Phi_2, \mathbf{I}_{J_1 J_2 M}) \cdot \text{kron}(\Phi_3, \mathbf{I}_{J_1 MN}) \cdot \text{diag}\{\Phi_4^{(0)}, \Phi_4^{(1)}, \dots, \Phi_4^{(MNI-1)}\}$$
(2.66)

where $\mathbf{I}_{(\cdot)}$ is an identity matrix with the subscript indicating its dimensions, and M_1, N_1, J_1, and J_2 denote the reduced number of transmit elements, receive elements, pulses, and fast time samples, respectively, with the total number of reduced measurements $J = M_1 N_1 J_1 J_2$. The matrix Φ_1 is an $M_1 \times M$ matrix, Φ_2 is an $N_1 \times N$ matrix, Φ_3 is a $J_2 \times I$ matrix, and each of the Φ_4 matrices is a $J_1 \times K$ matrix for determining the reduced number of transmitting elements, receiving

elements, pulses and fast time samples, respectively. Each of the three matrices $\Phi_1, \Phi_2,$ and Φ_3 consists of randomly selected rows of an identity matrix. These choices of reduced matrix dimensions amount to selection of subsets of existing available degrees of freedom offered by the fully deployed imaging system. Any other matrix structure does not yield to any hardware simplicity or saving in acquisition time. On the other hand, three different choices, discussed in Section VI.B, are available for compressive acquisition of each pulse in fast time.

Given the reduced measurement vector $\breve{y}$ in (2.65), we can recover $\hat{r}$ by solving the following equation,

$$\hat{\hat{r}} = \arg \min_{\hat{r}} \|\hat{r}\|_{l_1} \text{ subject to } \Phi \Psi \hat{r} \approx \breve{y} \tag{2.67}$$

We note that the reconstructed vector can be rearranged into $N_{v_x} N_{v_z}$ matrices of dimensions $N_x \times N_z$ in order to depict the estimated target reflectivity for different vertical and horizontal velocity combinations. Note that i) Stationary targets will be localized for the (0,0) velocity pair, and ii) Two targets located at the same spatial location but moving with different velocities will be distinguished and their corresponding reflectivity and motion parameters will be estimated.

2.7.3   Illustrative Results

A real data collection experiment was conducted in the Radar Imaging Laboratory, Villanova University. The system and signal parameters are the same as described in Section VI.C. The origin of the coordinate system was chosen to be at the center of the receive array. The scene behind the wall consisted of one stationary target and one moving target, as shown in Fig. 14. A metal sphere of 0.3 m diameter, placed on a 1 m high Styrofoam pedestal, was used as the stationary target. The pedestal was located 1.25 m behind the wall, centered at (0.49 m, 2.45 m). A person walked towards the front wall at a speed of 0.7 m/s approximately along a straight line path, which is located 0.2 m to the right of the transmitter. The back and the right side wall in the region behind the front wall were covered with RF absorbing material, whereas the 8 in thick concrete side wall on the left and the floor were uncovered. A coherent processing interval of 15 pulses was selected.

The image region is chosen to be 4 m × 6 m, centered at (-0.31 m, 3 m), and divided into 41 × 36 pixels in crossrange and downrange. As the human moves directly towards the radar, we only consider varying vertical velocity from -1.4 m/s to 0 m/s, with a step size of 0.7 m/s, resulting in three velocity pixels. The space-slow time-fast time response of the scene consists of 8 × 15 × 2872 measurements. First, we reconstruct the scene without time gating the wall response. Only 33.3% of the 15 pulses and 13.9% of the fast-time samples are randomly selected for each of the 8 receive elements, resulting in 8 × 5 × 400 space-slow time-fast time measured data. This is equivalent to 4.6% of the total data volume. Figure 15 depicts the CS based result, corresponding to the three velocity bins, obtained with the number of OMP iterations set to 50. We observe from Figs. 15(a) and 15(b) that both the stationary sphere and the moving person cannot be localized. The reason behind this failure is two-fold: 1) The front wall is a strong extended target and as such, most of the degrees of freedom of the reconstruction process are used up for the wall, and 2) The low SCR, due to the much weaker returns from the moving and stationary targets compared to the front wall reflections, causes the targets to be not reconstructed with the residual degrees of freedom of the OMP. These results confirm that the performance of the sparse reconstruction scheme is hindered by the presence of the front wall.

After removal of the front wall return from the received signals through time gating, the space-slow time-fast time data includes 8 × 15 × 2048 measurements. For CS, we used all eight receivers, randomly selected 5 pulses (33.3% of 15) and chose 400 Gaussian random measurements (19.5% of

2048) in fast time, which amounts to using 6.5% of the total data volume. The number of OMP iterations was set to 4. Figures 16(a), 16(b), and 16(c) are the respective images corresponding to the 0 m/s, -0.7 m/s, and -1.4 m/s velocities. It is apparent that with the wall gated out, both the stationary and moving targets have been correctly localized even with the reduced set of measurements.

2.8   Conclusion

In this section, we presented a review of important approaches for sparse behind-the-wall scene reconstruction using CS. These approaches address the unique challenges associated with fast and efficient imaging in urban operations. First, considering stepped-frequency SAR operation, we presented a linear matrix modeling formulation, which enabled application of sparsity based reconstruction of a scene of stationary targets using a significantly reduced data volume. Access to background scene without the targets of interest was assumed to render the scene sparse upon coherent subtraction. Subsequent sparse reconstruction using a much reduced data volume was shown to successfully detect and accurately localize the targets.

Second, assuming no prior access to a background scene, we examined the performance of joint mitigation of the wall backscattering and sparse scene reconstruction in TWRI applications. We focused on subspace projections approach, which is a leading method for combating wall clutter. Using real data collected with a stepped-frequency radar, we demonstrated that the subspace projection method maintains proper performance when acting on reduced data measurements.

Third, a sparsity-based approach for imaging of interior building structure was presented. The technique made use of the prior information about building construction practices of interior walls to both devise an appropriate linear model and design a sparsifying dictionary based on the expected wall alignment relative to the radar's scan direction. The scheme was shown to provide reliable determination of building layouts, while achieving substantial reduction in data volume.

Fourth, we described a group sparse reconstruction method to exploit the rich indoor multipath environment for improved target detection under efficient data collection. A ray tracing approach was used to derive a multipath model, considering reflections not only due to targets interactions with interior walls, but also the multipath propagation resulting from ringing within the front wall. Using stepped-frequency radar data, it was shown that this technique successfully reconstructed the ground truth without multipath ghosts, and also increased the SCR at the true target locations.

Fifth, we detected and localized moving humans behind walls and inside enclosed structures using an approach that combines sparsity-driven radar imaging and change detection. Removal of stationary background via CD resulted in a sparse scene of moving targets, whereby CS schemes could exploit full benefits of sparsity-driven imaging. An appropriate CD linear model was developed that allowed scene reconstruction within the CS framework. Using pulsed radar operation, it was demonstrated that a sizable reduction in the data volume is provided by CS without degradation in system performance.

Finally, we presented a CS based technique for joint localization of stationary and moving targets in TWRI applications. The front wall returns were suppressed through time gating, which was made possible by the short temporal support characteristic of the UWB transmit waveform. The SCR enhancement as a result of time gating permitted the application of CS techniques for scene reconstruction with few observations. We established an appropriate signal model that enabled formulation of linear modeling with sensing matrices for reconstruction of the downrange-crossrange-velocity space. Results based on real data experiments demonstrated that joint

localization of stationary and moving targets can be achieved via sparse regularization using a reduced set of measurements without any degradation in system performance.

2.9 References

[1] M. G. Amin (Ed.), *Through-the-Woll Rodor Imoging*, CRC Press, Boca Raton, FL, 2010.

[2] M. G. Amin (Ed.), "Special issue on Advances in Indoor Radar Imaging," *J. Franklin Inst.*, vol. 345, no. 6, pp. 556–722, Sept. 2008.

[3] M. G. Amin and K. Sarabandi (Eds.), "Special issue on Remote Sensing of Building Interior," *IEEE Trons. Geosci. Remote Sens.*, vol. 47, no. 5, pp. 1270–1420, 2009.

[4] E. Baranoski, "Through-wall imaging: Historical perspective and future directions," *J. Fronklin Inst.*, vol. 345, no. 6, pp. 556 – 569, Sept. 2008.

[5] S. E. Borek, "An overview of through the wall surveillance for homeland security," in *Proc. 34th, Applied Imogery ond Pottern Recognition Workshop*, vol. 6, Oct. 2005, pp. 19–21.

[6] H. Burchett, "Advances in Through Wall Radar for Search, Rescue and Security Applications," in *Proc. Inst. of Eng. ond Tech. Conf. Crime ond Security*, London, UK, Jun. 2006, pp. 511–525.

[7] A. Martone, K. Ranney, and R. Innocenti, "Through-the-wall detection of slow-moving personnel," in *Proc. SPIE*, vol. 7308, 2009, pp. 73080Q1-73080Q12.

[8] X. P. Masbernat, M. G. Amin, F. Ahmad, and C. Ioana, "An MIMO-MTI approach for through-the-wall radar imaging applications," in *Proc. 5th Int. Woveform Diversity ond Design Conf.*, 2010.

[9] M. G. Amin and F. Ahmad, "Change detection analysis of humans moving behind walls," *IEEE Trons. Aerosp. Electronic Syst.*, In Press.

[10] M. Amin, F. Ahmad, and W. Zhang, "A compressive sensing approach to moving target indication for urban sensing," in *Proc. IEEE Rodor Conference*, Kansas City, MO, May 2011, pp. 509 – 512.

[11] J. Moulton, S. Kassam, F. Ahmad, M. Amin, and K. Yemelyanov, "Target and change detection in synthetic aperture radar sensing of urban structures," in *Proc. IEEE Rodor Conference*, Rome, Italy, May 2008.

[12] A. Martone, K. Ranney, and R. Innocenti, "Automatic through the wall detection of moving targets using low-frequency ultra-wideband radar," in *Proc. IEEE Rodor Conf.*, Washington D.C., May 2010, pp. 39-43.

[13] S. S. Ram and H. Ling, "Through-wall tracking of human movers using joint Doppler and array processing," *IEEE Geosci. Remote Sens. Lett.*, vol. 5, no.3, pp. 537-541, 2008.

[14] C. P. Lai and R. M. Narayanan, "Through-wall imaging and characterization of human activity using ultrawideband (UWB) random noise radar," in *Proc. SPIE - Sensors ond C3I Technologies for Homelond Security ond Homelond Defense*, May 2005, vol. 5778, pp. 186-195.

[15] C. P. Lai and R. M. Narayanan, "Ultrawideband random noise radar design for through-wall surveillance," *IEEE Trons. Aerosp. Electronic Syst.*, vol. 46, no. 4, pp. 1716-1730, 2010.

[16] S. S. Ram, Y. Li, A. Lin, and H. Ling, "Doppler-based detection and tracking of humans in indoor environments," *J. Fronklin Inst.*, vol. 345, no. 6, pp. 679-699, Sept. 2008.

[17] E. F. Greneker, "RADAR flashlight for through-the-wall detection of humans," in *Proc. SPIE – Torgets Bockgrounds: Choract. Representotion IV*, vol. 3375, 1998, pp. 280–285.

[18] T. Thayaparan, L. Stankovic, and I. Djurovic, "Micro-Doppler human signature detection and its application to gait recognition and indoor imaging," *J. Fronklin Inst.*, vol. 345, no. 6, pp.700-722, Sept. 2008.

[19] I. Orovic, S. Stankovic, and M. Amin, "A new approach for classification of human gait based on time-frequency feature representations," *Signol Process.*, vol. 91, no. 6, pp. 1448-1456, 2011.

[20] A. R. Hunt, "Use of a frequency-hopping radar for imaging and motion detection through walls," *IEEE Trons. Geosci. Remote Sens.*, vol. 47, no. 5, pp. 1402-1408, 2009.

[21] F. Ahmad, M. G. Amin, and P. D. Zemany, "Dual-Frequency Radars for Target Localization in Urban Sensing," *IEEE Trons. Aerasp. Electronic Syst.*, vol. 45, no. 4, pp. 1598–1609, Oct, 2009.

[22] N. Maaref, P. Millot, C. Pichot, and O. Picon, "A study of UWB FM-CW Radar for the detection of human beings in motion inside a building," *IEEE Trons. Geosci. Remote Sens.*, vol. 47, no. 5, pp. 1297-1300, 2009.

[23] F. Soldovieri, R. Solimene, and R. Pierri, "A simple strategy to detect changes in through the wall imaging," *Pragress in Electramagnetics Research M,* vol. 7, pp. 1-13, 2009.

[24] T. S. Ralston, G. L. Charvat, and J. E. Peabody, "Real-time through-wall imaging using an ultrawideband multiple-input multiple-output (MIMO) phased array radar system," in *Proc. IEEE Intl. Symp. Phosed Array Systems and Technalogy,* Boston, MA, Oct. 2010, pp. 551-558.

[25] F. Ahmad, G. J. Frazer, S. A. Kassam, and M. G. Amin, "Design and implementation of near-field, wideband synthetic aperture beamformers," *IEEE Trons. Aerosp. Electronic Syst.*, vol. 40, no. 1, pp. 206-220, Jan. 2004.

[26] F. Ahmad, M. G. Amin and S. A. Kassam, "Synthetic aperture beamformer for imaging through a dielectric wall," *IEEE Trans. Aerasp. Electranic Syst.*, vol. 41, no. 1, pp. 271-283, 2005.

[27] M. G. Amin and F. Ahmad, "Wideband synthetic aperture beamforming for through-the-wall imaging," *IEEE Signol Process. Mog.*, vol. 25, no. 4, pp. 110-113, July 2008.

[28] F. Ahmad and M. Amin, "Multi-location wideband synthetic aperture imaging for urban sensing applications," *J. Fronklin Inst.*, vol. 345, no. 6, pp. 618 – 639, 2008.

[29] F. Soldovieri and R. Solimene, "Through-wall imaging via a linear inverse scattering algorithm," *IEEE Geosci. Remote Sens. Lett.*, vol. 4, no. 4, pp. 513-517, 2007.

[30] F. Soldovieri, G. Prisco, and R. Solimene, "A multi-array tomographic approach for Through-Wall Imaging," *IEEE Trans. Geosci. Remate Sens.*, vol. 46, no. 4, pp. 1192–1199, 2008.

[31] E. M. Lavely, Y. Zhang, E. H. Hill III, Y-S. Lai, P. Weichman, and A. Chapman, "Theoretical and experimental study of through-wall microwave tomography inverse problems," J. *Fronklin Inst.*, vol. 345, no. 6, pp. 592–617, Sept. 2008.

[32] M.M. Nikolic, M. Ortner, A. Nehorai, and A.R. Djordjevic, "An Approach to Estimating Building Layouts Using Radar and Jump-Diffusion Algorithm," *IEEE Trons. Antennos Propog.*, vol. 57, no. 3, pp. 768–776, Mar. 2009.

[33] C. Le, T. Dogaru, L. Nguyen, and M.A. Ressler, "Ultrawideband (UWB) radar imaging of building interior: Measurements and predictions," *IEEE Trans. Geasci. Remote Sens.*, vol. 47, no. 5, pp. 1409–1420, May 2009.

[34] E. Ertin and R.L. Moses, "Through-the-Wall SAR Attributed Scattering Center Feature Estimation," *IEEE Trons. Geosci. Remote Sens.*, vol. 47, no. 5, pp. 1338–1348, May 2009.

[35] M. Aftanas and M. Drutarovsky, "Imaging of the Building Contours with Through the Wall UWB Radar System," *Radiaengineering J.*, vol. 18, no. 3, pp. 258–264, 2009.

[36] F. Ahmad, Y. Zhang, and M. G. Amin, "Three-dimensional wideband beamforming for imaging through a single wall," *IEEE Geasci. Remote Sens. Lett.*, vol. 5, no. 2, April 2008.

[37] L. P. Song, C. Yu, and Q. H. Liu, "Through-wall imaging (TWI) by radar: 2-D tomographic results and analyses," *IEEE Trans. Geosci. Remote Sens.*, vol. 43, no. 12, pp. 2793–2798, 2005.

[38] M. Dehmollaian, M. Thiel, and K. Sarabandi, "Through-the-wall imaging using differential SAR," *IEEE Trons. Geosci. Remote Sens.*, vol. 47, no. 5, pp. 1289 – 1296, 2009.

[39] M. Dehmollaian and K. Sarabandi, "Refocusing through building walls using synthetic aperture radar," *IEEE Trons. Geosci. Remote Sens.*, vol. 46, no. 6, pp. 1589–1599, 2008.

[40] F. Ahmad and M. G. Amin, "Noncoherent Approach to Through-the-Wall Radar Localization," *IEEE Trans. Aerosp. Electronic Syst.*, vol. 42, no. 4, pp. 1405-1419, 2006.

[41] F. Ahmad and M. G. Amin, "A Noncoherent Radar System Approach for Through-The-Wall Imaging," in *Proc. SPIE - Sensars, and Commond, Contral, Cammunicotions, ond Intelligence Technalogies IV Conference,* Orlando, FL, 2005, vol. 5778, pp. 196-207.

[42] Y. Yang and A. Fathy, "Development and implementation of a real-time see-through-wall radar system based on FPGA," *IEEE Trans. Geasci. Remate Sens.*, vol. 47, no. 5, pp. 1270-1280, 2009.

[43] F. Ahmad and M. G. Amin, "High-resolution imaging using capon beamformers for urban sensing applications," in *Prac. IEEE Int. Canf. an Acaustics, Speech, and Signal Pracess.*, Honolulu, HI, 2007, pp. II-985 - II-988.

[44] M. Soumekh, *Synthetic Aperture Radar Signal Pracessing with Matlab Algorithms*, John Wiley and Sons, New York, NY, 1999.

[45] Y-S. Yoon and M. G. Amin, "Spatial filtering for wall-clutter mitigation in through-the-wall radar imaging," *IEEE Trans. Geasci. Remote Sens.*, vol. 47, no. 9, pp. 3192–3208, 2009.

[46] R. Burkholder, "Electromagnetic models for exploiting multi-path propagation in through-wall radar imaging," in *Prac. Intl. Canf. Electramagnetics in Advanced Applicatians*, Sept. 2009, pp. 572 – 575.

[47] T. Dogaru and C. Le, "SAR images of rooms and buildings based on FDTD computer models," *IEEE Trans. Geasci. Remate Sens.*, vol. 47, no. 5, pp. 1388 –1401, May 2009.

[48] S. Kidera, T. Sakamoto, and T. Sato, "Extended imaging algorithm based on aperture synthesis with double-scattered waves for UWB radars," *IEEE Trans. Geasci. Remate Sens.*, vol. 49, no. 12, pp. 5128–5139, 2011.

[49] P. Setlur, M. Amin, and F. Ahmad, "Multipath model and exploitation in through-the-wall and urban radar sensing," *IEEE Trans. Geasci. Remate Sens.*, vol. 49, no. 10, pp. 4021–4034, 2011.

[50] F. Ahmad, M. G. Amin, and S. A. Kassam, "A Beamforming Approach to Stepped-Frequency Synthetic Aperture Through-the-Wall Radar Imaging," in *Prac. IEEE Int. Warkshop an Camputatianal Advances in Multi-Sensar Adaptive Pracessing*, Puerto Vallarta, Mexico, vol. 345, 2005, pp. 24–27.

[51] F. Ahmad and M. G. Amin, "Performance of autofocusing schemes for single target and populated scenes behind unknown walls," in *Prac. SPIE - Radar Sensar Technalagy XI*, Orlando, FL, vol. 6547, April, 2007.

[52] F. Ahmad, M. G. Amin, and G. Mandapati, "Autofocusing of through-the-wall radar imagery under unknown wall characteristics, *IEEE Trans. Image Pracess.* vol. 16, no. 7, pp. 1785–1795, 2007.

[53] G. Wang and M. G. Amin, "Imaging through unknown walls using different standoff distances," *IEEE Trans. Signal Pracessing* vol. 54, no. 10, pp. 4015-4025, 2006.

[54] G. Wang, M. G. Amin, and Y. Zhang, "A new approach for target locations in the presence of wall ambiguity," *IEEE Trans. Aerasp. Electranic Syst.*, vol. 42, no. 1, pp. 301-315, 2006.

[55] Y. Yoon and M. G. Amin, "High-Resolution Through-the-Wall Radar Imaging using Beamspace MUSIC," *IEEE Trans. Antennas Prapag.*, vol. 56, no. 6, pp. 1763-1774, 2008.

[56] Y. Yoon, M. G. Amin, and F. Ahmad, "MVDR Beamforming for Through-the-Wall Radar Imaging," *IEEE Trans. Aerasp. Electranic Syst.*, vol. 47, no. 1, pp. 347-366, 2011.

[57] W. Zhang, A. Hoorfar, C. Thajudeen, and F. Ahmad, "Full polarimetric beamforming algorithm for through-the-wall radar imaging," *Radia Science*, vol. 46, RS0E16, doi:10.1029/2010RS004631.

[58] C. Thajudeen, W. Zhang, and A. Hoorfar, "Time-domain wall parameter estimation and mitigation for through-the-wall radar image enhancement," in *Prac. Pragress in Electramagnetics Research Symp.*, Cambridge, USA, July 2010.

[59] F. Tivive, M. Amin, and A. Bouzerdoum, "Wall clutter mitigation based on eigen-analysis in through-the-wall radar imaging," in *Prac. IEEE Warkshap an DSP*, 2011.

[60] F. H. C. Tivive, A. Bouzerdoum, and M. G. Amin, "An SVD-based approach for mitigating wall reflections in through-the-wall radar imaging," in *Prac. IEEE Radar Canf.*, Kansas City, MO, 2011, pp. 519–524.

[61] R. Chandra, A. N. Gaikwad, D. Singh, and M. J. Nigam, "An approach to remove the clutter and detect the target for ultra-wideband through wall imaging," *J. Geaphysics and Engineering*, vol. 5, no. 4, pp. 412–419, 2008.

[62] Y.S. Yoon and M. G. Amin, "Compressed sensing technique for high-resolution radar imaging," in *Prac. SPIE*, vol. 6968, 2008, pp. 69681A–1–69681A–10.

[63] Q. Huang, L. Qu, B. Wu, and G. Fang, "UWB through-wall imaging based on compressive sensing," *IEEE Trans. Geosci. Remote Sens.*, vol. 48, no. 3, pp. 1408-1415, 2010.

[64] Y.S. Yoon and M. G. Amin, "Through-the-Wall Radar Imaging Using Compressive Sensing Along Temporal Frequency Domain," in *Proc. IEEE Int. Conf. Acoustics, Speech and Signal Processing*, Dallas, TX, Mar. 2010.

[65] M.G. Amin, F. Ahmad, and W. Zhang, "Target RCS exploitations in compressive sensing for through wall imaging," in *Proc. 5th Int. Waveform Diversity and Design Conf.*, Niagara Falls, Canada, Aug. 2010.

[66] M. Leigsnering, C. Debes, and A. M. Zoubir, "Compressive sensing in through-the-wall radar imaging," in *Proc. IEEE Int. Conf. Acoustics, Speech and Signal Process.*, Prague, Czech Republic, 2011, pp. 4008–4011.

[67] J. Yang, A. Bouzerdoum, F. H. C. Tivive and M. G. Amin. "Multiple-measurement vector model and its application to Through-the-Wall Radar imaging," in *Proc. IEEE Int. Conf. Acoustics, Speech and Signal Process.*, Prague, Czech Republic, May 2011.

[68] F. Ahmad and M. G. Amin, "Partially Sparse Reconstruction of Behind-the-Wall Scenes," in *Proc. SPIE - Compressive Sensing Conf.*, Baltimore, MD, vol. 8365, Apr. 2012.

[69] R. Solimene, F. Ahmad, and F. Soldovieri, "A novel CS-TSVD strategy to perform data reduction in linear inverse scattering problems," *IEEE Geosci. Remote Sens. Lett.*, vol. 9, no. 5, pp. 881–885, 2012.

[70] F. Ahmad and M. G. Amin, "Through-the-wall human motion indication using sparsity-driven change detection," *IEEE Trans. Geosci. Remote Sens.*, vol. 51, no. 2, pp. 881-890, 2013.

[71] E. L. Targarona, M. G. Amin, F. Ahmad, and M. Nájar, "Compressive sensing for through wall radar imaging of stationary scenes using arbitrary data measurements," in *Proc. 11th Intl. conf. on information science, signal processing, and their applications*, Montreal, Canada, 2012.

[72] E. L. Targarona, M. G. Amin, F. Ahmad, and M. Nájar, "Wall mitigation techniques for indoor sensing within the CS framework," in *Proc. Seventh IEEE workshop on sensor array and multi-channel signal processing*, Hoboken, NJ, 2012.

[73] E. Lagunas, E., M. Amin, F. Ahmad, F. and M. Najar, "Joint wall mitigation and compressive sensing for indoor image reconstruction," *IEEE Trans. Geosci. Remote Sens.*, vol. 51, no. 2, pp. 891-906, 2013.

[74] J. Qian, F. Ahmad, and M. G. Amin, "Through-the-wall moving target detection and localization using sparse regularization," in *Journal of Electronic Imaging*, vol. 22, no. 2, Apr. 2013. doi: 10.1117/1.JEI.22.2.021002.

[75] W. Zhang, M. G. Amin, F. Ahmad, A. Hoorfar, and G. E. Smith, "Ultrawideband impulse radar through-the-wall imaging with compressive sensing," *Intl. J. Antennas Propag.*, vol. 2012, p. 11, 2012.

[76] E. Lagunas, M. Amin, F. Ahmad, and M. Nájar, "Determining building interior structures using compressive sensing," *Journal of Electronic Imaging*, vol. 22, no. 2, Apr. 2013. doi: 10.1117/1.JEI.22.2.021003.

[77] E. Candes, J. Romberg, and T. Tao, "Stable signal recovery from incomplete and inaccurate measurements," *Communications in Pure and Applied Math.*, vol. 59, pp. 1207-1223, 2006.

[78] D. Donoho, M. Elad, and V. Temlyakov, "Stable recovery of sparse overcomplete representations in the presence of noise," *IEEE Trans. Inf. Theory*, vol. 52, no. 1, pp. 6 – 18, Jan. 2006.

[79] D.L. Donoho, "Compressed sensing," *IEEE Trans. Inf. Theory*, vol. 52, no. 4, pp. 1289–1306, Apr. 2006.

[80] R. Baraniuk and P. Steeghs, "Compressive radar imaging," in *Proc. IEEE Radar Conf.*, Waltham, MA, April 2007, pp. 128-133.

[81] E. J. Candes and M. B. Wakin, "An introduction to compressed sampling," *IEEE Signal Process. Mag.*, vol. 25, no. 2, pp. 21-30, 2008.

[82] M. Herman and T. Strohmer, "High-resolution radar via compressive sensing," *IEEE Trans. Signal Process.*, vol. 57, no. 6, pp. 2275-2284, 2009.

[83] A. Gurbuz, J. McClellan, and W. Scott, "Compressive sensing for subsurface imaging using ground penetrating radar," *Signal Process.*, vol. 89, no. 10, pp. 1959 – 1972, 2009.

[84] A. Gurbuz, J. McClellan, and W. Scott, "A compressive sensing data acquisition and imaging method for stepped frequency GPRs," *IEEE Trans. Signal Process.*, vol. 57, no. 7, pp. 2640 –2650, 2009.

[85] M. C. Shastry, R. M. Narayanan, and M. Rangaswamy, "Compressive radar imaging using white stochastic waveforms," in *Proc. Intl. Waveform Diversity and Design Conf.*, Niagara Falls, Canada, Aug. 2010, pp. 90-94.

[86] L. C. Potter, E. Ertin, J. T. Parker, and M. Cetin, "Sparsity and compressed sensing in radar imaging," *Proc. of the IEEE*, vol. 98, no. 6, pp. 1006-1020, 2010.

[87] Y. Yu and A. P. Petropulu, "A study on power allocation for widely separated CS-based MIMO radar," in *Proc. SPIE - Compressive Sensing Conf.*, Baltimore, MD, vol. 8365, Apr. 2012.

[88] F. Ahmad (Ed.), *Compressive Sensing*, Proc. SPIE, vol. 8365, SPIE, Bellingham, WA, 2012.

[89] K. Krueger, J.H. McClellan, and W.R. Scott, Jr., "3-D imaging for ground penetrating radar using compressive sensing with block-toeplitz structures," in *Proc. IEEE 7th Sensor Array and multichannel Signal Process. Workshop*, Hoboken, NJ, Jun 2012.

[90] D. L. Donoho, "For most large underdetermined systems of linear equations, the minimal l_1-norm solution is also the sparsest solution, *Communications on Pre and Applied Mathematics*, vol. 59, no. 6, pp. 797-829, 2006.

[91] S. Boyd and L. Vandenberghe, *Convex Optimization*, Cambridge University Press, 2004.

[92] S. S. Chen, D. L. Donoho, and M. A. Saunders, "Atomic decomposition by basis pursuit," *SIAM J. Scientific Computing*, vol. 20, no. 1, pp. 33–61, 1999.

[93] S. Mallat and Z. Zhang, "Matching Pursuit with Time-Frequency Dictionaries," *IEEE Trans. Signal Process.*, vol. 41, no. 12, pp. 3397–3415, 1993.

[94] J. A. Tropp, "Greed is good: Algorithmic results for sparse approximation," *IEEE Trans. Inf. Theory*, vol. 50, no. 10, pp. 2231–2242, 2004.

[95] J. A. Tropp and A. C. Gilbert, "Signal recovery from random measurements via orthogonal matching pursuit," *IEEE Trans. Inf. Theory*, vol. 53, no. 12, pp. 4655–4666, 2007.

[96] D. Needell and J. A. Tropp, "CoSaMP: Iterative signal recovery from incomplete and inaccurate samples," *Appl. Comput. Harmon. Anal.*, vol. 26, no. 3, pp. 301-321, May 2009.

[97] P. Boufounos, M. Duarte and R. Baraniuk, "Sparse signal reconstruction from noisy compressive measurements using cross validation," in *Proc. IEEE 14th Statistical Signal Process. Workshop*, Madison, WI, Aug. 2007, pp.299-303.

[98] R. Ward, "Compressed sensing with cross validation," *IEEE Trans. Inf. Theory*, vol. 55, no. 12, pp. 5773-5782, 2009.

[99] T. Do, L. Gan, N. Nguyen, and T. Tran, "Sparsity adaptive matching pursuit algorithm for practical compressed sensing," in *Proc. 42nd Asilomar Conf. on Signals, Systems and Computers*, Pacific Grove, CA, Oct. 2008, pp. 581-587.

[100] M. Leigsnering, F. Ahmad, M. Amin, and A. Zoubir, "Multipath Exploitation in Through-the-Wall Radar Imaging using Sparse Reconstruction," *IEEE Trans. Aerosp. Electronic Syst.*, Under review.

[101] A. Karousos, G. Koutitas, and C. Tzaras, "Transmission and reflection coefficients in time-domain for a dielectric slab for UWB signals," in *Proc. IEEE Vehicular Technology Conf.*, 2008, pp. 455–458.

[102] S. Wright, R. Nowak, and M. Figueiredo, "Sparse reconstruction by separable approximation," *IEEE Trans. Signal Process.*, vol. 57, no. 7, pp. 2479–2493, 2009.

[103] W. Deng, W. Yin, and Y. Zhang, "Group sparse optimization by alternating direction method," Department of Computational and Applied Mathematics, Rice University, Technical Report TR11-06, 2011.

[104]   M. Yuan and Y. Lin, "Model selection and estimation in regression with grouped variables," *J. Rayal Statistical Society*, Series B, vol. 68, pp. 49–67, 2006.

[105] R. G. Baraniuk, V. Cevher, M. F. Duarte, and C. Hegde, "Model-based compressive sensing," *IEEE Trans. Inf. Theory*, vol. 56, pp. 1982–2001, April 2010. [Online]. Available: http://arxiv.org/abs/0808.3572

[106] F. Bach, R. Jenatton, J. Mairal and G. Obozinski, "Convex optimization with sparsity-inducing norms," In S. Sra, S. Nowozin, S. J. Wright., editors, Optimization for Machine Learning, MIT Press, 2011.

[107] Y. Eldar, P. Kuppinger, and H. Bolcskei, "Block-sparse signals: Uncertainty relations and efficient recovery," *IEEE Trans. Signal Process.*, vol. 58, no. 6, pp. 3042–3054, 2010.

[108] F. Ahmad and M. G. Amin, "Sparsity-based change detection of short human motion for urban sensing," in *Proc. Seventh IEEE Workshop on Sensor Array and Multi-Channel Signal Processing*, Hoboken, NJ, June 2012.

[109] X. X. Zhu and R. Bamler, "Tomographic SAR inversion by L_1-norm regularization—The compressive sensing approach," *IEEE Trans. Geasci. Remate Sens.*, vol.48, no.10, pp.3839-3846, Oct. 2010.

[110] A. S. Khawaja and J. Ma, "Applications of compressed sensing for SAR moving-target velocity estimation and image compression," *IEEE Trans. Instrumentatian and Measurement*, vol. 60, no. 8, pp. 2848-2860, 2011.

[111] F. Ahmad and M. G. Amin, "Wall clutter mitigation for MIMO radar configurations in urban sensing," in *Proc. 11th Intl. Conference on Informatian Science, Signal Pracessing, and their Applicatians*, Montreal, Canada, July 2012.

FIGURE CAPTIONS

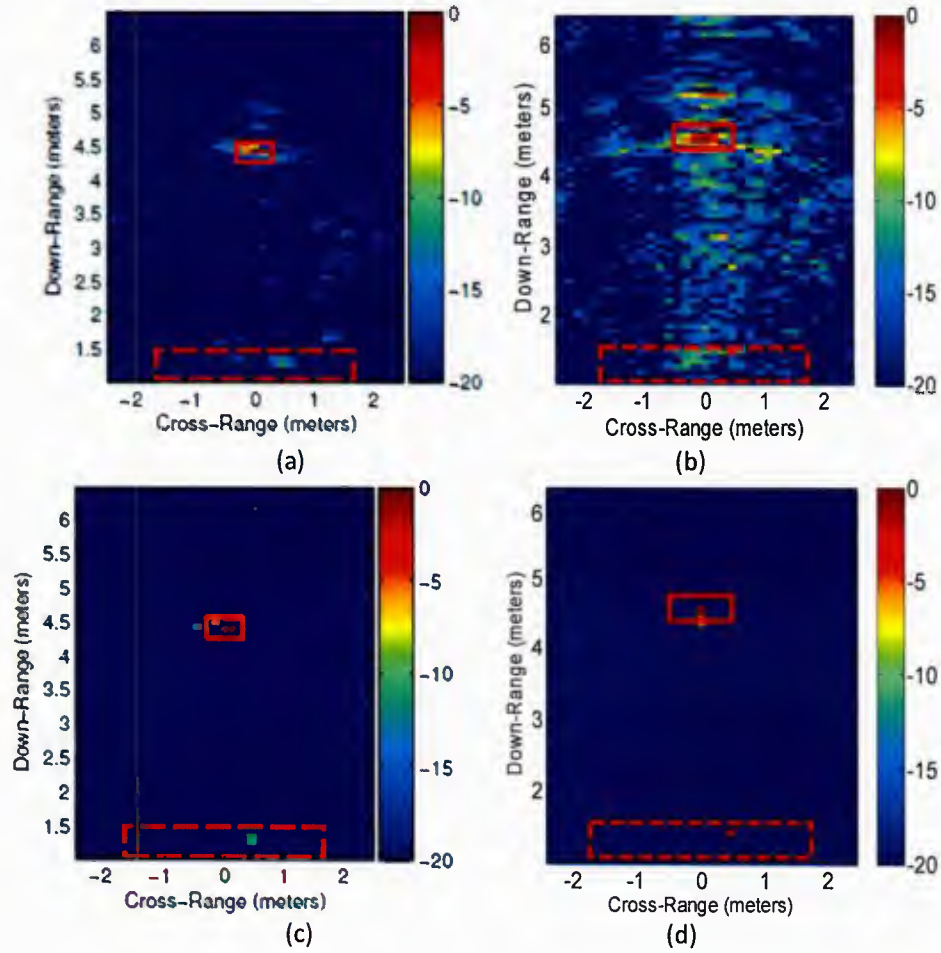Figure 1. Geometry on transmit of the equivalent two-dimensional problem.

Figure 2. Imaging results after background subtraction. (a) Backprojection image using full data (b) Backprojection image using 10% data volume, (c) CS reconstructed image using full data, (d) CS reconstructed image using 10% of the data.
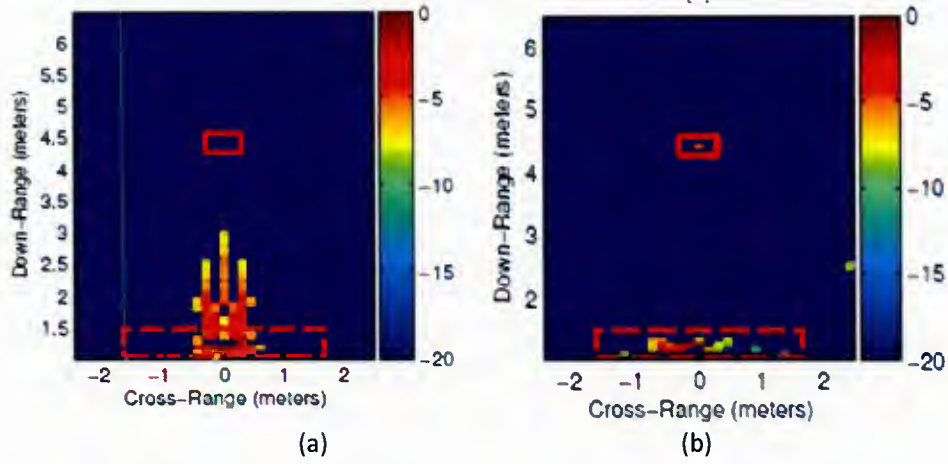
Figure 3.   CS based imaging result (a) using full data volume without background subtraction, (b) using 10% data volume with the same frequency set at each antenna.
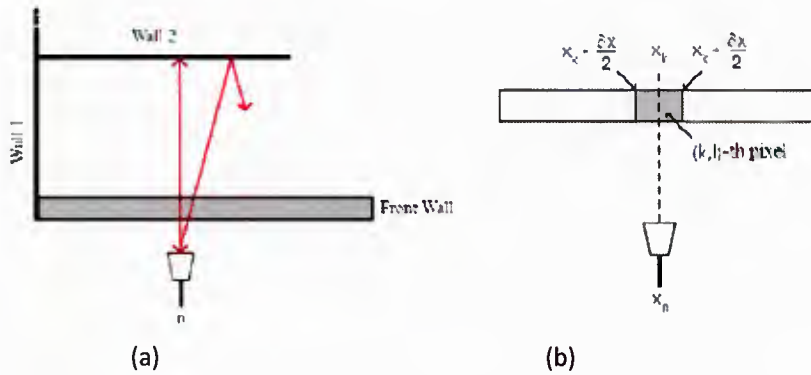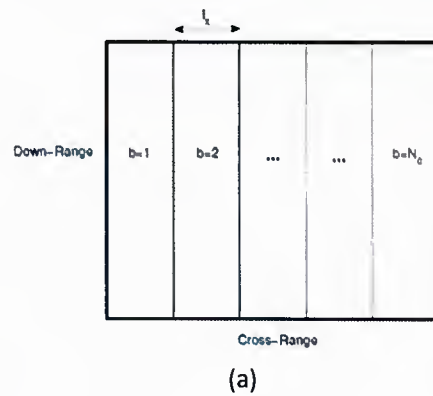
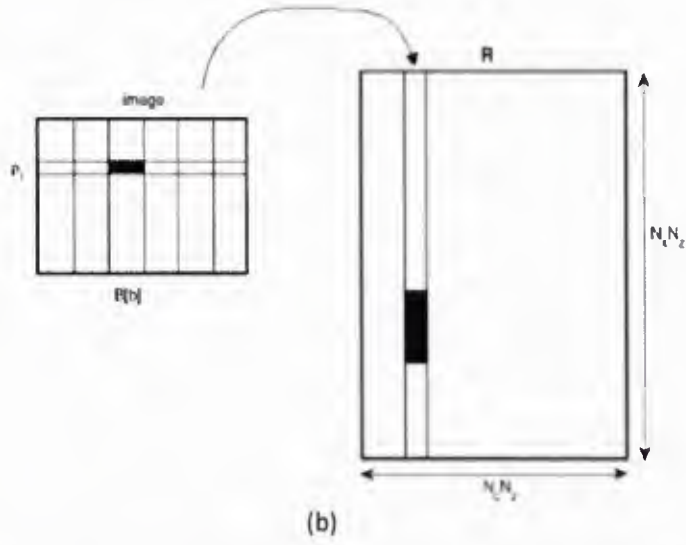Figure 4.   (a) Specular reflections produced by walls, (b) Indicator function.

Figure 5.   (a) Crossrange division into blocks of Ix pixels, (b) Sparsifying dictionary generation.
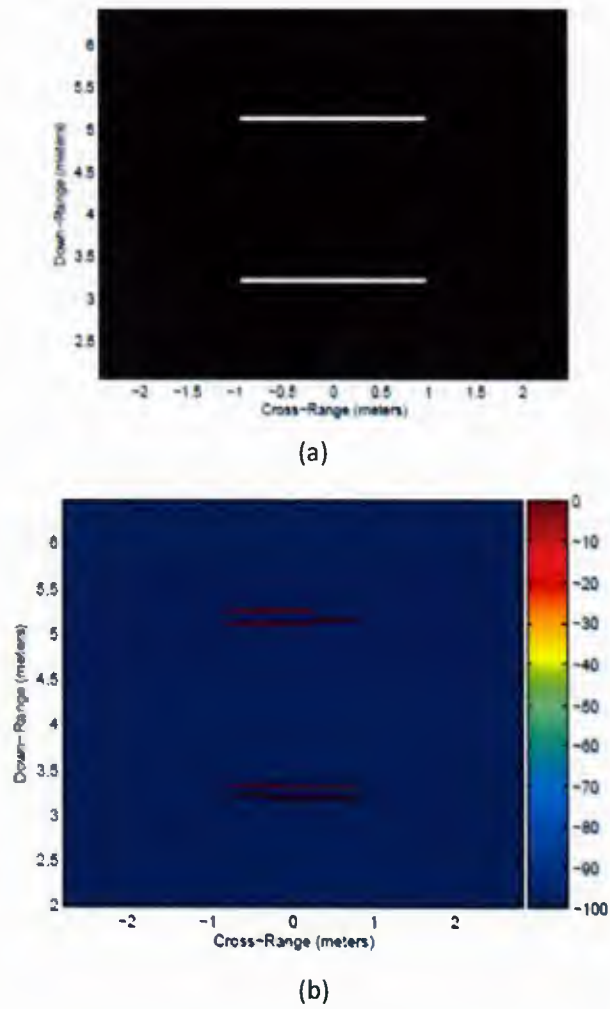
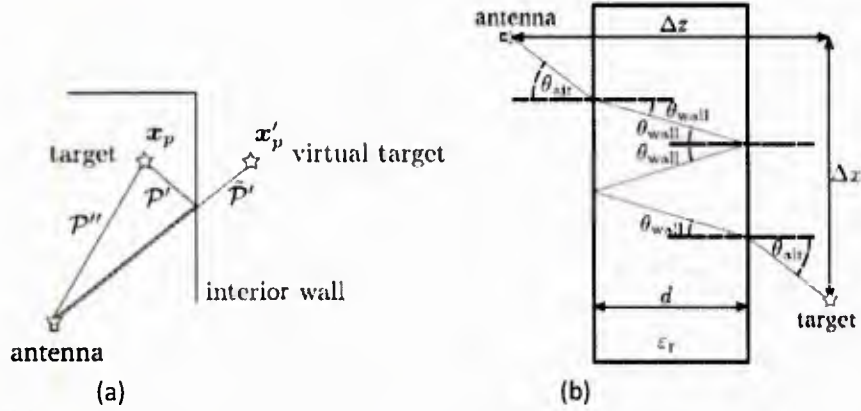Figure 6.   (a) Scene geometry, (b) reconstructed image.

Figure 7. (a) Multipath propagation via reflection at an interior wall, (b) Wall ringing propagation with i_w=1 internal bounces.
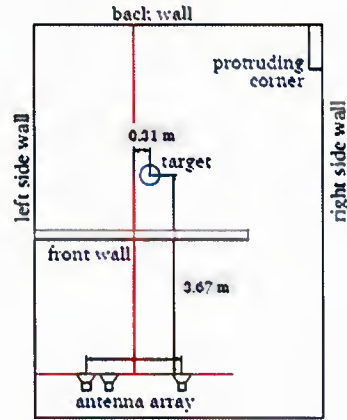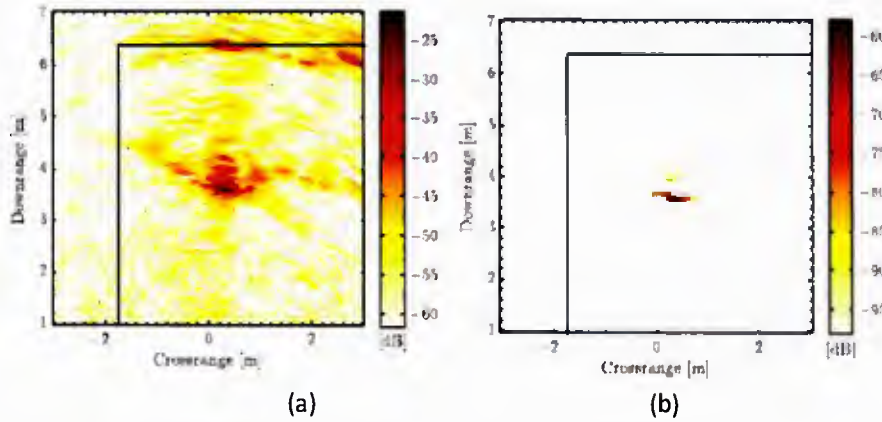
Figure 8.   Scene Layout.

Figure 9. (a) Backprojection image with full data volume; (b) Group sparse reconstruction with 25% of the antenna elements and 50% of the frequencies.
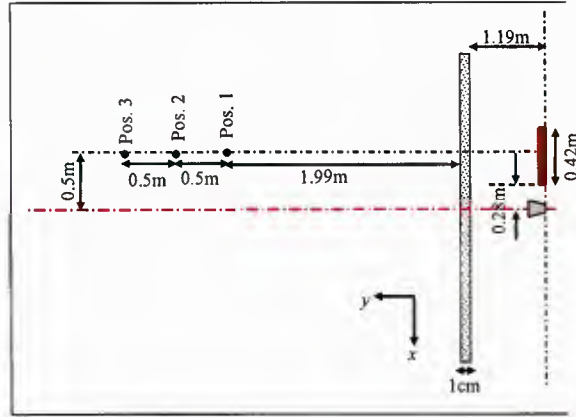
Figure 10. Scene Layout for the target undergoing translational motion.
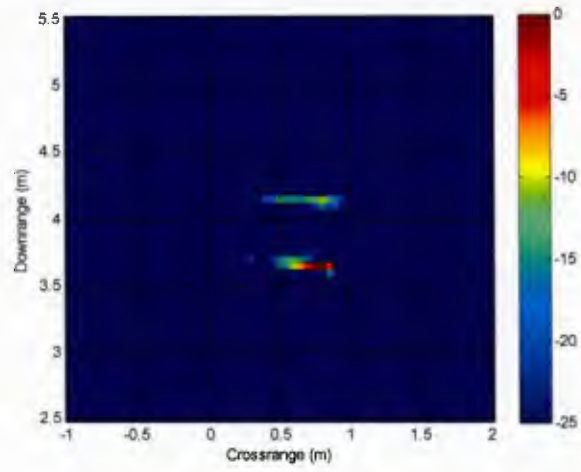
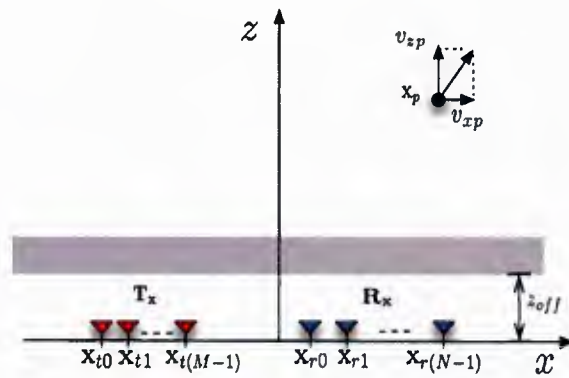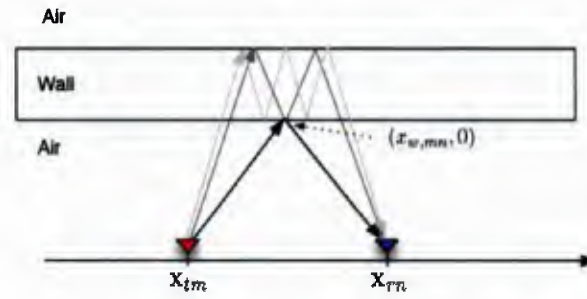Figure 11. Sparsity-based CD image using 5% of the data volume.

Figure 12. Geometry on transmit and receive.

Figure 13. Wall reverberations.

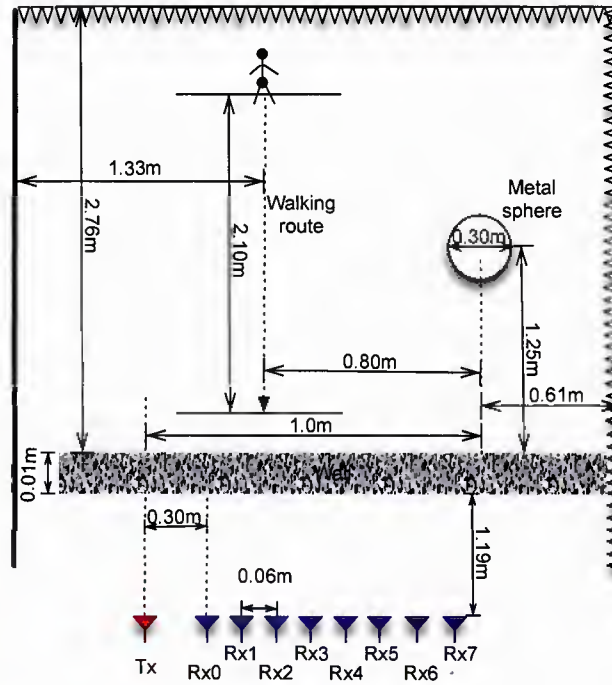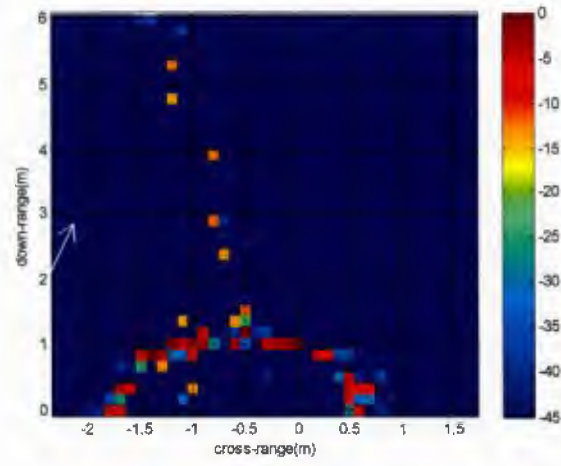Figure 14. The configuration of the experiment.

Figure 15. Imaging result for both stationary and moving targets without time gating, (a) CS reconstructed image $\sigma(0,0)$, (b) CS reconstructed image $\sigma(0,-0.7)$, (c) CS reconstructed image $\sigma(0,-1.4)$.

Figure 16. Imaging result for both stationary and moving targets after time gating: (a) CS reconstructed image $\sigma(0,0)$, (b) CS reconstructed image $\sigma(0,-0.7)$, (c) CS reconstructed image $\sigma(0,-1.4)$.

Figure 1. Geometry on transmit of the equivalent two-dimensional problem.

Figure 2. Imaging results after background subtraction. (a) Backprojection image using full data (b) Backprojection image using 10% data volume, (c) CS reconstructed image using full data, (d) CS reconstructed image using 10% of the data.

(a)   (b)

Figure 3. CS based imaging result (a) using full data volume without background subtraction, (b) using 10% data volume with the same frequency set at each antenna.

(a)   (b)

Figure 4. (a) Specular reflections produced by walls, (b) Indicator function.

(a)

(b)

Figure 5. (a) Crossrange division into blocks of l_x pixels, (b) Sparsifying dictionary generation.

(a)

(b)

Figure 6. (a) Scene geometry, (b) reconstructed image.

(a)   (b)

Figure 7. (a) Multipath propagation via reflection at an interior wall, (b) Wall ringing propagation with i_w =1 internal bounces.

Figure 8. Scene Layout.

(a)   (b)

Figure 9. (a) Backprojection image with full data volume; (b) Group sparse reconstruction with 25% of the antenna elements and 50% of the frequencies.

Figure 10. Scene Layout for the target undergoing translational motion.

Figure 11. Sparsity-based CD image using 5% of the data volume.

Figure 12. Geometry on transmit and receive.

Figure 13. Wall reverberations.

Figure 14. The configuration of the experiment.
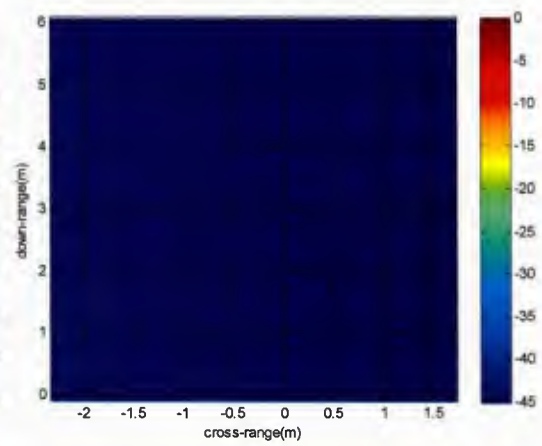
(a)

(b)   (c)

Figure 15. Imaging result for both stationary and moving targets without time gating, (a) CS reconstructed image $\sigma(0,0)$, (b) CS reconstructed image $\sigma(0,-0.7)$,(c) CS reconstructed image $\sigma(0,-1.4)$.
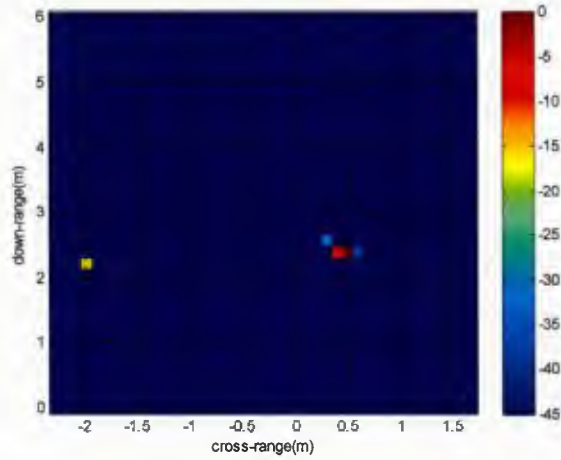
(a)
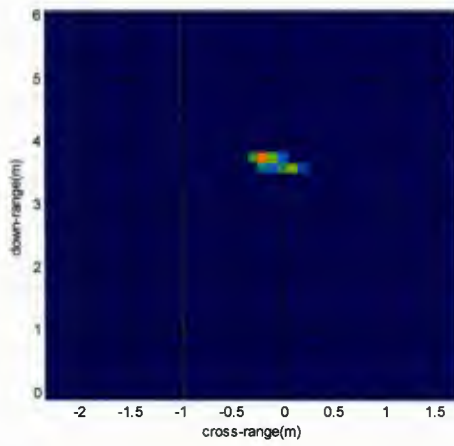
(b)

(c)

Figure 16. Imaging result for both stationary and moving targets after time gating: (a) CS reconstructed image $\sigma(0,0)$, (b) CS reconstructed image $\sigma(0,-0.7)$, (c) CS reconstructed image $\sigma(0,-1.4)$

REPORT DOCUMENTATION PAGE

Form Approved
OMB No. 0704-0188

1. REPORT DATE *(DD-MM-YYYY)* 12/18/2013	2. REPORT TYPE Final Technical Reprot	3. DATES COVERED *(From - To)* 03/01/2010 - 10/31/2013

4. TITLE AND SUBTITLE
Improved Target Detection in Urban Structures using Distributed Sensing and Fast Data Acquisition Techniques

5a. CONTRACT NUMBER

5b. GRANT NUMBER
N00014-10-1-0455

5c. PROGRAM ELEMENT NUMBER

6. AUTHOR(S)
Moeness Amin, Fauzia Ahmad, Yimin Zhang, Batu Chalise, Pawan Setlur, Christian Debes

5d. PROJECT NUMBER

5e. TASK NUMBER

5f. WORK UNIT NUMBER

7. PERFORMING ORGANIZATION NAME(S) AND ADDRESS(ES)
Center for Advanced Communicationsm Villanova Universiity
800 E. Lancaster Avenue, Villanova, PA 19085

8. PERFORMING ORGANIZATION REPORT NUMBER
VU 527874

9. SPONSORING/MONITORING AGENCY NAME(S) AND ADDRESS(ES)
Office of Naval Research
875 North Rudolph Street
Arlington, VA 22203-1995

10. SPONSOR/MONITOR'S ACRONYM(S)
ONR

11. SPONSORING/MONITORING AGENCY REPORT NUMBER

12. DISTRIBUTION AVAILABILITY STATEMENT
Approved for Public Release; Distribution is Unlimited.

13. SUPPLEMENTARY NOTES

14. ABSTRACT
We introduce detection techniques of targets behind walls and inside enclosed structures. These techniques rely on the intensity histogram distinctions between targets and clutter and perform iterative thresholding to achieve desirable probabilities of detection and false alarm. We propose wall clutter mitigation techniques based on wall strong specular reflection as compared to target diffuse multipath characteristics. Multipath exploitation techniques are developed to eliminate ghosts and increase target to clutter ratio. Fast data acquisition is performed by reducing frequencies and thinning the synthesized aperture. Compressive sensing methods are applied to provide situation awareness of sparse scenes using significantly reduced data.

15. SUBJECT TERMS
Compressive Sensing, Through-the-Wall Radar, Urban Sensing, Indoor Imaging

16. SECURITY CLASSIFICATION OF:			17. LIMITATION OF ABSTRACT	18. NUMBER OF PAGES	19a. NAME OF RESPONSIBLE PERSON Moeness Amin
a. REPORT U	b. ABSTRACT U	c. THIS PAGE U			19b. TELEPONE NUMBER *(Include area code)* 610 519 4263

Standard Form 298 (Rev. 8-98)
Prescribed by ANSI-Std Z39-18